https://ntrs.nasa.gov/search.jsp?R=19970010250 2020-06-18T00:13:21+00:00Z

IN-07

NASA Contractor Report 198543

Atomization and Dispersion of a Liquid Jet Injected Into a Crossflow of Air

J.E. Seay and G.S. Samuelsen
University of California
Irvine, California

November 1996

Prepared for
Lewis Research Center
Under Grant NAG3–1124

National Aeronautics and
Space Administration

ATOMIZATION AND DISPERSION OF A LIQUID JET INJECTED INTO A CROSSFLOW OF AIR

CONTRACTOR REPORT
submitted to the National Aeronautics and Space Administration

J.E. Seay
G.S. Samuelsen

UCI-ARTR-95-4

August 1995

UNIVERSITY OF CALIFORNIA

IRVINE CA 92717-3550

Table of Contents

List of Symbols

A	Area
ALR	Air-to-Liquid Ratio
c_{avg}	Fully Mixed Concentration
$\bar{c}_i$	Time-Averaged Concentration at a Point
c_{var}	Spatial Concentration Variance
C_d	Coefficient of Drag
CCD	Charged Coupled Device
CO_2	Carbon Dioxide
CO	Carbon Monoxide
D	Drop Diameter
D_{Jet}	Air Hole Diameter
F	Thrust
g_c	Gravitational Constant
h	Enthalpy
HSCT	High Speed Civil Transport
J	Momentum Flux Ratio $(\rho U^2)_{Jet}/(\rho U^2)_{Mainstream}$
LFE	Laminar Flow Element
LDI	Lean Direct Injected
LIF	Laser Induced Fluorescence
LPP	Lean Prevaporized Premixed

$\dot{m}$	Mass Flow
NO	Nitric Oxide
NO_2	Nitrogen Dioxide
NO_x	Nitrogen Oxides
O_3	Ozone
PDI	Phase Doppler Interferometry
PDPA	Phase Doppler Particle Analyzer
PLLIF	Planar Liquid Laser Induced Fluorescence
Q_A	Air Volume Flow
Q_L	Liquid Volume Flow
RQL	Rich Burn - Quick Mix - Lean Burn
S	Signal
SCFM	Standard Feet Cubed per Minute
SMD	Sauter Mean Diameter, D_{32}
UHC	Unburned Hydrocarbons
U	Velocity
U_R	Relative Velocity between Fuel and Air
U_S	Spatial Unmixedness Parameter
V	Velocity
X	Radial Distance, (i.e., distance from injector panel)
Y	Penetration
Z	Downstream Distance

ΔP_{Air}	Air Circuit Pressure Drop
ΔP_{Fuel}	Fuel Circuit Pressure Drop
ϕ	Equivalence Ratio
ρ_L	Liquid Density
σ	Surface Tension
μ_L	Liquid Viscosity

List of Tables

List of Figures

Abstract

Atomization and Dispersion of a Liquid Jet
Injected into a Crossflow of Air

In recent years, environmental regulations have become more stringent, requiring lower emissions of mainly nitrogen oxides (NO_x), as well as carbon monoxide (CO) and unburned hydrocarbons (UHC). These regulations have forced the gas turbine industry to examine non-conventional combustion strategies, such as the lean burn approach. The reasoning behind operating under lean conditions is to maintain the temperature of combustion near and below temperatures required for the formation of thermal nitric oxide (NO). To be successful, however, the lean processes require careful preparation of the fuel/air mixture to preclude formation of either locally rich reaction zones, which may give rise to NO formation, or locally lean reaction zones, which may give rise to inefficient fuel processing. As a result, fuel preparation is crucial to the development and success of new aeroengine combustor technologies.

A key element of the fuel preparation process is the fuel nozzle. As nozzle technologies have developed, airblast atomization has been adopted for both industrial and aircraft gas turbine applications. However, the majority of the work to date has focused on prefilming nozzles, which despite their complexity and high cost have become an industry standard for conventional combustion strategies. It is likely that the new strategies required to meet future emissions goals will utilize novel fuel injector approaches, such as radial injection. This thesis proposes and demonstrates an experiment to examine, on a mechanistic level (i.e., the physics of the action), the processes associated with the atomization, evaporation, and dispersion of a liquid jet introduced, from a radial, plain-jet airblast injector, into a crossflow of air. This understanding requires the knowledge not only of what factors influence atomization, but also the underlying mechanism associated with liquid breakup and dispersion. The experimental data acquired identify conditions and geometries for improved performance of radial airblast injectors.

Chapter 1 - Introduction

Conventional gas turbine combustors are judged by their performance with respect to energy efficiency, durability, pattern factor, and relight capability. However, as the world has become more environmentally aware, regulations limiting pollutant emissions from gas turbine combustors have been enacted and are becoming more and more stringent.

A pollutant emission is classified as any contaminant present in sufficiently high concentrations to cause adverse effects on humans, animals, plants, or materials. For gas turbine combustion, three main species have been identified as pollutants: carbon monoxide (CO), unburned hydrocarbons (UHC), and nitrogen oxides (NO_x). Nitrogen oxides are comprised of nitric oxide (NO), nitrogen dioxide (NO_2), NO_3, N_20 and other compounds.

Conventional combustors have the tendency to produce copious amounts of NO_x, due to two features of their operation. These combustors operate at fuel/air mass ratios near stoichiometric (ϕ=1) in the dome region to achieve robust stability. Air is then added at downstream locations to complete combustion and to cool the combustion products to an acceptable level for the first stage turbine blades. Although the overall fuel/air ratio is lean, the stoichiometric ratio in the dome yields high reaction temperatures.

Additionally, the recirculation zone present in the dome region provides residence time at these high temperatures, which results in the formation of thermal NO. A second feature of conventional combustors, which leads to thermal NO formation, is incomplete fuel/air mixing. Air and fuel are introduced into the dome region *separately* and mix to various degrees prior to reacting. Incomplete mixing leads to stoichiometric fuel/air pockets, which in turn yield high reaction temperatures, forming thermal NO.

The topic of this thesis is the improvement in fuel/air mixing with the purpose of reducing thermal NO formation. The research is applicable to the Lean-burn Direct Injected (LDI) combustor concept which operates under lean conditions ($\phi \approx 0.4$) in the dome region and, as a result, yields reduced reaction temperatures and limits thermal NO formation (e.g., Shaffar, 1993). All the combustion air is injected through the swirler which eliminates the need for dilution holes that are common in conventional gas turbine combustors. The liquid fuel is injected into the combustion air, mixed, and vaporized before burning. Atomization and dispersion of the fuel is therefore crucial to the success of the LDI concept. Any partially mixed zones of fuel and air will result in high reaction temperatures and thermal NO.

Previous work has demonstrated the effectiveness of lean direct injection, utilizing radial injection of fuel into a swirling airstream, for minimizing the formation of thermal NO (Correa, 1990; Shaffar, 1993). For the LDI concept to reduce the formation of NO, rapid atomization and evaporation of the liquid fuel must be achieved. Therefore the design and operation of the injector can be considered the most crucial element in a successful combustor. The goal of this thesis is to develop and demonstrate an experiment designed to establish a mechanistic understanding of the atomization process and to document the fuel preparation and injection characteristics of a liquid jet injected radially into a high velocity cross-stream. By examining variations in geometry and operating conditions, an optimal configuration for mixing and dispersion of the liquid fuel can be identified.

To develop an experiment, the following objectives must be met:

1) Develop an understanding of the factors influencing the atomization of liquid fuel in a high-velocity crossflow.
2) Design an experiment to reveal the role of geometry and operating conditions on atomization.
3) Examine and evaluate different geometrical variations. Determine the optimal geometric configuration for rapid atomization and dispersion of the fuel.

4) Examine and evaluate various operating conditions. Establish the optimal operating conditions for rapid atomization and dispersion of the fuel.

Chapter 2 presents background information on conventional and advanced combustor concepts, atomizer designs and properties, and environmental effects of combustor emissions. Sections 2.1 through 2.3 describe in detail the various configuration and operating schemes employed in conventional combustor concepts. Sections 2.4 and 2.5 display information on the environmental impacts of combustion and NO_x formation. Finally, in Sections 2.6 and 2.7, advanced combustor and injector concepts are presented.

Chapter 3 outlines the approach taken to achieve the goals of this thesis. Chapter 4 discusses in detail the test facility, experimental hardware, and diagnostic tools employed in the current study. Chapter 5 presents results from experimental testing and a discussion of the results. A summary and conclusion of findings is recorded in Chapter 6.

Chapter 2 - Background

The primary aim of this chapter is to describe in detail the design features and performance criteria for conventional and advanced gas turbines. Over the past 50 years, many improvements have been made to the combustor section. However the size, shape, and general appearance remain fairly similar to original combustor designs. This resemblance in appearance is primarily due to the desired performance requirements and space limitations, both of which have not changed drastically in the past 50 years.

2.1 - The Thermodynamics of Combustion

The thermodynamic cycle employed with gas turbines is the Brayton cycle. Because mass enters and leaves the gas turbine engine, one must consider it an open system. In the Brayton cycle, the compressor raises the pressure of the air, and heat is added at the high pressure by burning a fuel with the air. The high-temperature products of combustion are then expanded in the turbine to produce a work output. Part of this work output is consumed in driving the compressor, and the remainder is available for driving external mechanisms.

The turbojet engine, which is extensively employed with aircraft applications, is a simple modification of the Brayton cycle and is shown

schematically in Figure 1. By examining Figure 1b, several important aspects of gas turbine combustion are seen. The combustor is represented here by the heat addition step from 2 to 3, which occurs at a constant pressure. Any pressure losses realized between the compressor and turbine result in a reduction in the overall output work. Therefore, an ideal gas turbine combustor yields a zero percent pressure loss. Additionally, the hot combustion gases are expanded in the turbine only far enough to generate work to drive the compressor. Because the gas turbine cycle is a steady flow device, the energy required by the compressor can be expressed as follows:

$$h_2 - h_1 = h_3 - h_4 \tag{1}$$

where h is enthalpy corresponding to the position in Figure 1b. The remaining thermal energy is then converted to high-velocity kinetic energy by expanding it in a nozzle, depicted by step 4 to 5. The jet thrust results from the difference in momentum of the air flow entering the compressor and the high-velocity exhaust gases leaving the nozzle. The thrust is given by the following equation:

$$F = \frac{\dot{m}}{g_c}(V_1 - V_5) \tag{2}$$

where g_c is the gravitational constant, $\dot{m}$ is the mass flow, and V_1 and V_5 are the flow velocities corresponding to the points in Figure 1b. For this thesis, the combustor section of the overall system will be analyzed. Specifically, the atomization of the liquid fuel is addressed.

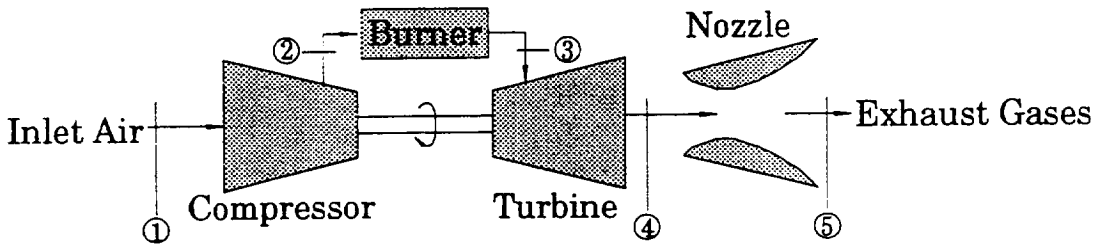

(a)

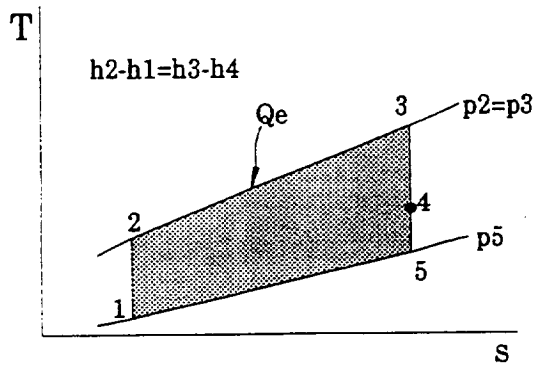

(b)

Figure 1 - Gas turbine cycle for jet propulsion. (adapted from Holman, 1988)

2.2 - Combustor Basic Design Features

In general, all gas turbine combustors employ some form of an air casing, diffuser, liner, and fuel injector. Depending on the performance criteria, many variations on the basic design can exist. It is instructive to examine the basic design of a gas turbine engine because it identifies the essential components required to meet the primary functions of the combustor.

Figure 2a demonstrates the simplest form of a combustor, a straight-walled duct connecting the compressor to the turbine. This configuration is impractical due to high pressure loss and high air speeds, which would blow the flame out. To reduce the pressure loss and the inlet air speed, a diffuser is attached to the front of the combustor section as seen in Figure 2b. The diffuser typically lowers the inlet air velocity by a factor of 5 (Lefebvre, 1983). However, even with a diffuser, the air speed is still too high to sustain a flame. Therefore a region of flow reversal must be created to provide a low velocity area, where the flame is sheltered and maintained. Figure 2c depicts how the flow reversal is achieved with a simple baffle in the flow.

The final problem lies with the flammability limits for a hydrocarbon/air mixture. To produce a reasonable temperature rise, the overall combustor air/fuel ratio (mass) must be approximately 50, which is well below the

flammability limit. Therefore the baffle is replaced with a perforated liner, which shelters the flame in the dome region and then introduces more air further downstream (Figure 2d). The air/fuel ratio obtained in the dome is approximately 14.5 and provides stable burning of the fuel. The air introduced downstream then increases the air/fuel ratio to 50 and cools the burned products down to an acceptable level.

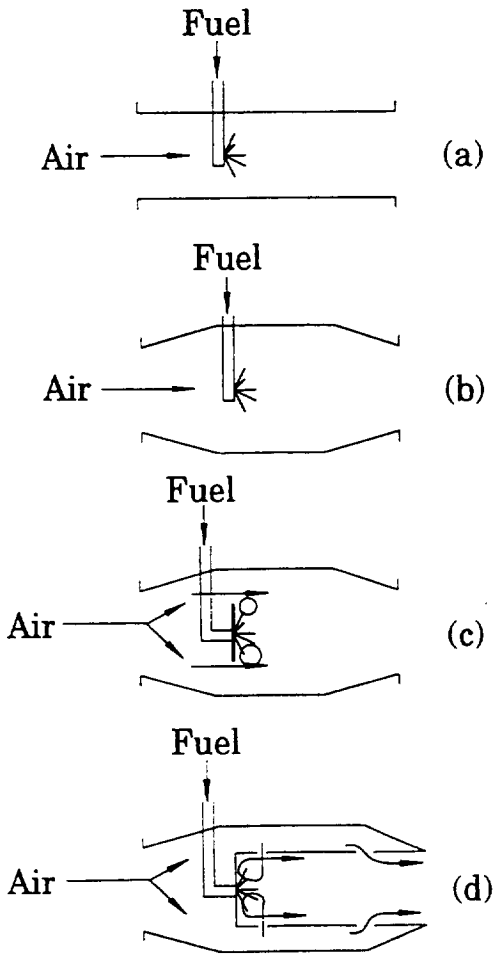

Figure 2 - Stages in the evolution of a conventional gas turbine (adapted from Lefebvre, 1983).

2.3 - Conventional Gas Turbine Combustor

For the reasons explained above, all gas turbine combustors share four basic elements: diffuser, air casing, liner, and fuel injector. The diffuser is required to reduce the air velocity leaving the compressor exit in order to prevent drastic pressure losses across the combustor liner. The air casing provides a plenum for the liner and assists in distributing the air uniformly to various areas within the combustor. The liner provides a low velocity region where the flame can be sustained and allows staging of the amount of air within the combustor.

The fuel injector's primary role is to deliver an atomized spray of fuel to the combustor. Without atomization, it is difficult for most fuels to react due to their slow vaporization rates. The rate of vaporization is enhanced by increasing the total surface area of the fuel. Therefore, better atomization of the fuel leads to smaller fuel droplets and increased surface area, which improves the rate of vaporization. The fuel injector is consequentially critical to the performance of the combustor, and its role of providing a uniform, well-atomized mixture to a combustor is becoming more crucial with advanced combustor designs. Many fuel injector designs have been developed and will be discussed in subsequent sections.

A typical gas turbine combustor can be described in zones. The division of the combustor into zones is helpful in understanding the processes which occur within the combustor. However, because the design criteria for combustors vary, it is sometimes difficult to define each zone in terms of their location. There are three main zones of a combustor: the primary zone, the intermediate or secondary zone, and the dilution zone. The size of each of these zones will vary depending on the performance requirements of the combustor. As seen in Figure 3, the primary zone lies in the dome region of the combustor liner. The primary zone is the location of reaction and recirculation and serves to anchor the flame and to provide sufficient time, temperature, and turbulence to complete combustion. Large-scale recirculation in the primary zone leads to slow mixing of the fuel and surrounding air and thus results in a low volumetric heat release but stable burning over a wide range of fuel flows. Small-scale recirculation in the primary zone promotes intense mixing and yields high volumetric heat releases, but reduces the burning range.

Immediately downstream of the primary zone, lies the intermediate zone. The intermediate zone is responsible for two main functions, which dictate its length. At low altitudes, it serves to prevent dissociation of CO_2 to CO by adding a small amount of air, which slightly lowers the temperature of the reactants. This lower temperature prevents any further dissociation and

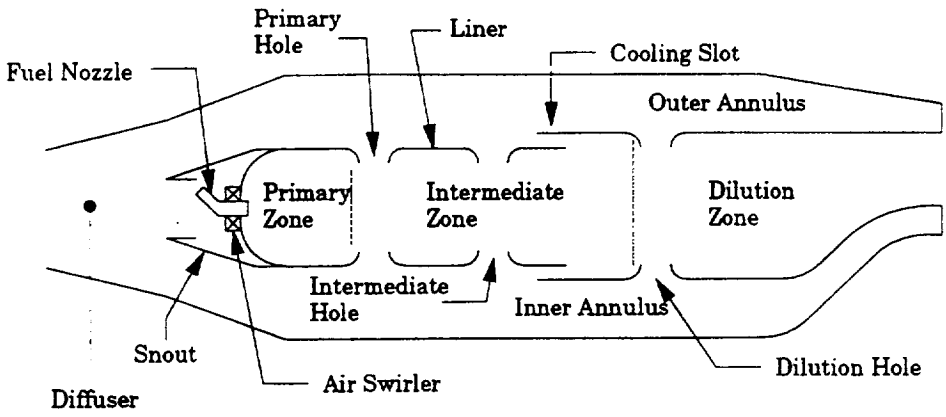

Figure 3 - Main components of a gas turbine combustor.
(adapted from Lefebvre, 1983)

provides sufficient time at temperature for any remaining CO or unburned fuel pockets to be consumed. At high altitudes, the intermediate zone serves as an extension of the primary zone, providing further time at temperature for the completion of the reaction.

The dilution zone is located between the intermediate zone and the first stage turbine blades. The dilution zone is required to develop a mean temperature and a temperature profile, which are acceptable to the turbine. This necessitates optimum penetration and mixing of any remaining air.

2.4 - Gas Turbine Combustors as a Source of Pollution

Conventional gas turbine combustors have the tendency to produce copious amounts of pollutants under various operating conditions. At idle and taxi

conditions, the flame temperature and residence time within the combustor is not sufficient to completely burn all the fuel available. Therefore emissions of unburned hydrocarbons and CO are rather high. Under climb and cruise conditions, the flame temperature in the dome is very high, which leads to the formation of NO_x. These three species (CO, UHC, and NO_x) are the primary pollutants emitted from the gas turbine engine. The following subsections will describe in detail the negative effects pollutant emissions from gas turbines have on the environment.

2.4.1 - Photochemical Oxidant (Smog)

In the early 1950's the importance of oxides of nitrogen and hydrocarbons in the formation of urban "photochemical smog" was discovered (Haagen-Smit, 1952; Haagen-Smit and Fox, 1956; Stanford Research Institute, 1954). Photochemical smog can be considered to be extremely high concentrations of tropospheric ozone (O_3). Because ozone is a very reactive compound, it is not typically present in the troposphere, where there is a plethora of species to react with. However, in urban areas, combustion processes are responsible for emitting large quantities of oxides of nitrogen and hydrocarbons. The production of ozone from the simplest hydrocarbon, methane, in the presence of high concentrations of NO, is summarized by the following reaction (Turco, 1990):

$$CH_4 + OH + 9O_2 \xrightarrow{NO} CO_2 + \frac{1}{2}H_2 + 2H_2O + 5O_3 \qquad (3)$$

As seen in the equation above, large quantities of ozone can be produced in urban areas, such as Los Angeles, and result in the formation of photochemical smog. Tropospheric ozone, if present in large amounts, could have global implications. Because ozone absorbs thermal radiation in the 9.6μm band, it serves as a greenhouse agent in the troposphere. A trend between increased levels of tropospheric ozone and the average increase in global temperature has been demonstrated (Fishman, 1991).

2.4.2 - Acid Rain

Emissions of NO_x into the troposphere can also result in the formation of acid rain. The removal of oxides of nitrogen from the troposphere occurs via the following reactions (Turco, 1990):

$$\begin{aligned} NO + O_3 &\rightarrow NO_2 + O_2 \\ NO_2 + OH + M &\rightarrow HNO_3 + M \\ NO_2 + O_3 &\rightarrow NO_3 + O_2 \\ NO_2 + NO_3 + M &\rightarrow N_2O_5 + M \\ N_2O_5 + H_2O &\xrightarrow{Cloud} 2HNO_3 \end{aligned} \qquad (4)$$

The nitric acid formed via these reactions is readily scavenged by precipitation. Acid rain can lead to a variety of problems, including tree and crop damage as well as damage to manmade structures and machines. Acidification of lakes by acid rain can kill fish and destroy other aquatic life.

2.4.3 - Effects of NO_x on Stratospheric Ozone

Stratospheric ozone is crucial to life on Earth, because of its strong absorption of solar ultraviolet radiation (240-320 nm). The thin band of ozone found in the stratosphere protects both plant and animal life from the damaging effects of overexposure to ultraviolet radiation. The average concentration of ozone in the atmosphere was initially assumed to be dependent on the photodissociation of molecular oxygen as seen by the following equations (Chapman, 1930):

$$\begin{aligned} O_2 + h\nu &\rightarrow O + O \\ O + O_2 + M &\rightarrow O_3 + M \\ O_3 + h\nu &\rightarrow O + O_2 \\ O + O_3 &\rightarrow O_2 + O_2 \end{aligned} \qquad (5)$$

However the predicted ozone abundances using the pure oxygen Chapman chemistry are too high. Therefore, additional ozone loss processes must exist. Crutzen (1971) and Molina and Rowland (1974) showed that families

of catalytic processes exist that result in the destruction of ozone. These catalytic reactions can be expressed by the following:

$$\begin{aligned} &X + O_3 \rightarrow XO + O_2 \\ &XO + O \rightarrow X + O_2 \\ &\text{net: } O + O_3 \rightarrow 2O_2 \end{aligned} \qquad (6)$$

where X may be H, OH, NO, Cl, or Br. These reactive chemical species can be divided into families of related compounds. As seen in Figure 4, these main families all play a role in determining the mean concentration of ozone in the stratosphere. Further research in this area has shown that ozone layer chemistry is rather complex, requiring a large number of constituents (~50) and photochemical processes (~200) (National Academy of Sciences, 1977).

The balance of the complex cycle depicted in Figure 4 can be upset by the introduction of man-made species into the stratosphere that enhance the destruction of ozone. In 1975, the emissions of chlorofluorocarbons were found to be potentially responsible for the catalytic destruction of stratospheric ozone (Rowland and Molina, 1975). These findings resulted in a world ban on the production and use of chlorofluorocarbons. The emission of NO_x from aircraft gas turbine engines could further upset the natural ozone cycle, increasing the net rate of ozone destruction. This was first

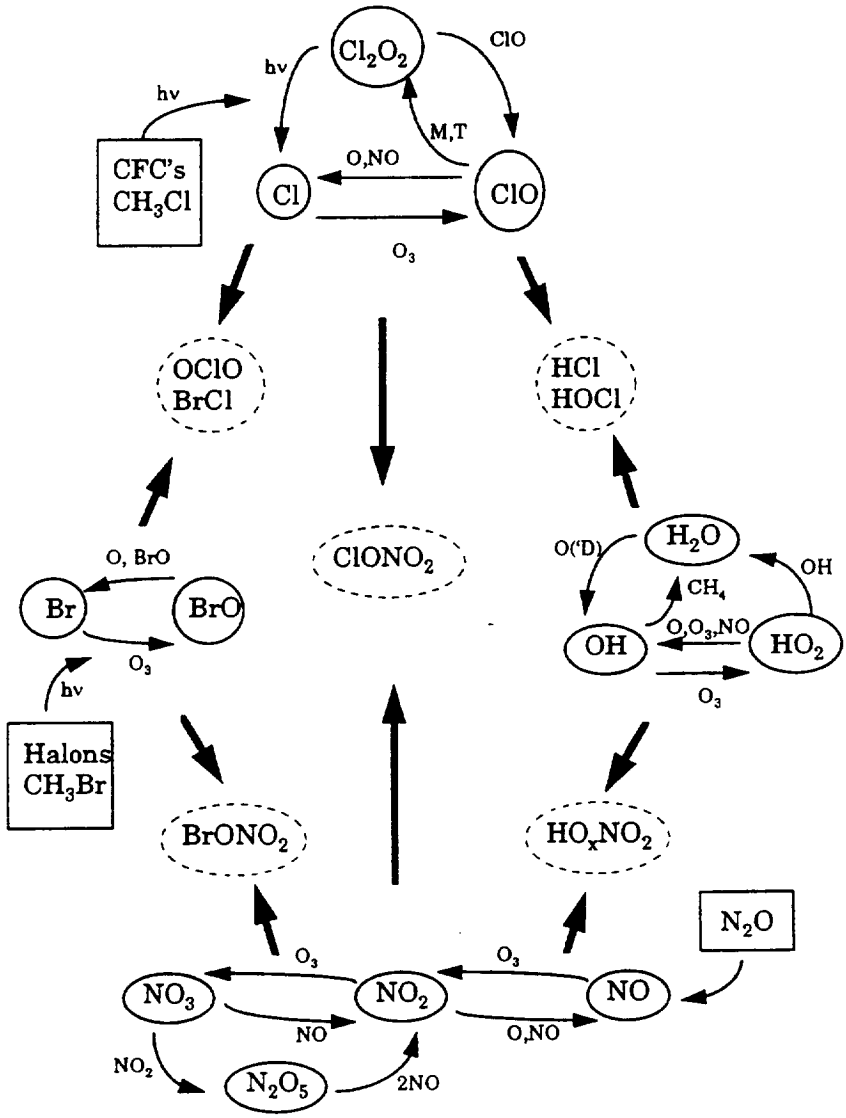

Figure 4 - Stratospheric Chemistry

recognized during the U.S. Supersonic Transport (SST) program (Johnston, 1971). Due to the potentially harmful environmental effects, the SST was not built in America. However, a new National Aeronautics and Space Administration (NASA) program has emerged to develop a supersonic aircraft that will cruise at altitudes in the lower stratosphere. This program is termed the High Speed Civil Transport (HSCT).

Because the HSCT is scheduled to fly in the stratosphere, the program is very concerned with the emissions of NO_x. Much research has begun on predicting the effects a fleet of HSCT's will have on the stratosphere (Ko et. al., 1991). Because the ozone layer chemistry is extremely complex, varying results have been obtained by different research groups. To circumvent this problem, a conservative approach has been adopted which assumes that emissions of NO_x from current aircraft gas turbines are too high for use in an HSCT application. Therefore, reduction in the emission of NO_x is one of the main goals of the HSCT program. NASA has set a program goal of a ten fold reduction in NO_x from the levels currently emitted by conventional combustors (Prather et. al., 1992).

2.5 - The Formation of Oxides of Nitrogen

From previous sections, it is now clear that the reduction of NO_x from combustors has become a crucial element in their design. There are three main mechanisms by which NO_x can be formed. These mechanisms are described as thermal NO, prompt NO, and fuel NO. The chemical processes by which NO_x is formed by each of these mechanisms will be described in detail in the following sections.

2.5.1 - Thermal NO

Thermal NO has been identified as the largest source of NO_x emissions from gas turbine combustors (Lefebvre, 1983). It is generally accepted that the formation of nitric oxide can be described by the following series of reactions (Zeldovich, 1946):

$$\begin{aligned} O_2 &\leftrightarrow 2O \\ O + N_2 &\xleftrightarrow{k_1} NO + N \\ N + O_2 &\xleftrightarrow{k_2} NO + O \end{aligned} \qquad (7)$$

The formation of NO is several orders of magnitude slower than the main heat release reactions and is therefore kinetically limited. The first equation exhibits the equilibrium dissociation of unburned oxygen molecules. Because equilibrium dissociation of nitrogen molecules does not occur at the temperatures seen within a gas turbine combustor, the only

source for nitrogen molecules is the second reaction. This reaction requires high thermal energy in order to break apart the triple-bound nitrogen molecule, and is therefore the rate limiting step in the formation of thermal NO. NO formation is aided by both high temperatures and high oxygen concentrations. Strategies for reducing thermal NO formation center on controlling these factors.

The formation rate, ω, for thermal NO is given by (Correa, 1990):

$$\omega = 2A[N_2]\,[O]\exp\left(\frac{-E_a}{RT}\right) \qquad (8)$$

where A is the pre-exponential term in the Arrhenius rate for the forward step of equation 7 above, and [i] represents the molar concentration of species "i". The activation energy is presented above by E_a and T is the temperature. The empirically determined constant, A, has been reported as 7×10^{13} (Newhall, 1969). The activation energy for this reaction is rather high (E_a=76 kcal/mol). The thermal mechanism for the formation of thermal NO becomes dominant at temperatures above 1800-1900 K due to the high activation energy. The relationship between thermal NO and temperature is illustrated in Figure 5.

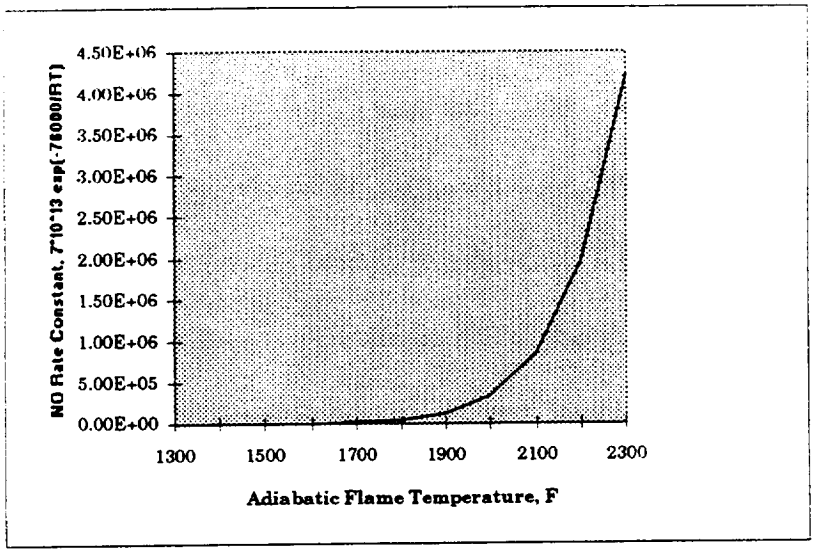

Figure 5 - Dependence on NO rate constant on temperature.

The reaction temperature within a gas turbine combustor is dictated by the amounts of fuel and oxidant injected. Complete combustion of a fuel/air mixture can be represented by the following reaction:

$$C_xH_y + \left(x + \frac{y}{4}\right)O_2 \Rightarrow xCO_2 + \frac{y}{2}H_2O \tag{9}$$

The mixture of fuel and air which yields complete combustion (i.e. no excess oxygen or fuel) is termed a stoichiometric mixture. The stoichiometric air to fuel mass ratio for Jet A fuel ($C_{12}H_{23}$) is calculated to be:

$$\frac{\dot{m}_{Fuel}}{\dot{m}_{Air}} = 0.0681 \tag{10}$$

where m_{Fuel} is the fuel mass flow rate and m_{Air} is the air mass flow rate. When discussing gas turbine combustion, this ratio is often expressed with a similar relationship, the equivalence ratio. The equivalence ratio is defined as the ratio of the actual amounts of fuel and air to the stoichiometric amount of fuel and air. The following equation demonstrates this definition:

$$\phi = \frac{(\dot{m}_{Fuel}/\dot{m}_{Air})_{Actual}}{(\dot{m}_{Fuel}/\dot{m}_{Air})_{Stoichiometric}} \qquad (11)$$

If the equivalence ratio is less than unity, the combustor is operating with excess air. Under these conditions, the combustor is said to be operating lean. If the equivalence ratio is greater than unity, the combustor outputs excess fuel and is described as operating rich. If the ratio is equal to unity, the system is operating at the stoichiometric fuel/air ratio.

The flame temperature developed within the combustor is dependent on the equivalence ratio. If operating lean ($\phi<1$), the excess air serves as a diluent, reducing the flame temperature. Some amount of the thermal energy released in the combustion reaction is consumed in bringing this excess oxygen up to the flame temperature. If operating rich ($\phi>1$), the unburned fuel serves as the diluent, again reducing the temperature attained in the

combustion zone. This relationship between equivalence ratio and flame temperature is presented in Figure 6.

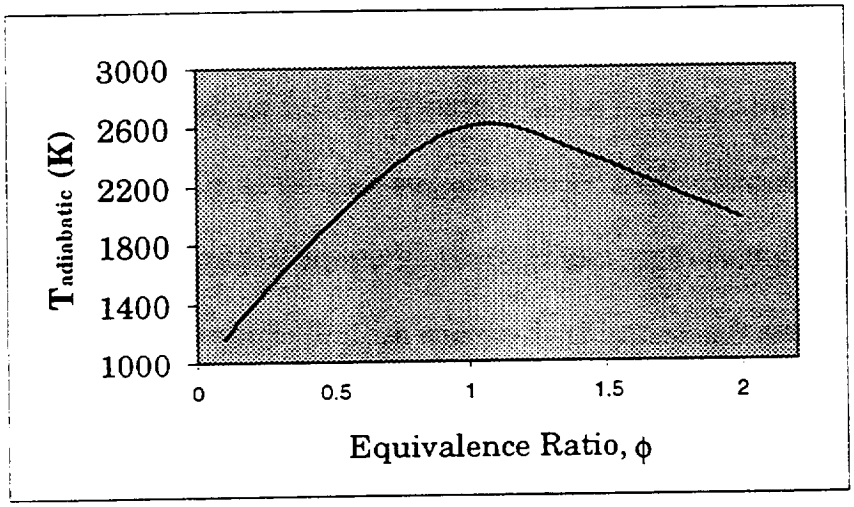

Figure 6 - Adiabatic flame temperature versus equivalence ratio.
Tin = 921 K

Figure 6 displays a plot of the adiabatic flame temperature versus equivalence ratio. The adiabatic flame temperature is a useful concept, often used to represent the maximum possible temperature that can be attained in a combustor. The adiabatic flame temperature assumes no energy loss to the surroundings. In practical applications, there is energy loss to the combustor casing and other elements. As seen in Figure 6, the highest temperature is achieved when operating slightly richer than the stoichiometric equivalence ratio (ϕ=1). Much of the research conducted on reducing thermal NO has therefore centered on combustors operating either very rich or very lean.

2.5.2 - Prompt NO

The second mechanism mentioned responsible for the formation of NO_x in gas turbine combustors is termed prompt NO. This term, "prompt", was adapted due the apparent instantaneous formation of NO observed in some hydrocarbon flames (Fenimore, 1970). Prompt NO forms rapidly in the early part of the flame and is therefore difficult quantify with current measurement techniques (Correa, 1990). The majority of prompt NO is formed via the following reaction (Fenimore, 1970):

$$CH + N_2 \Leftrightarrow HCN + N \tag{12}$$

The N atoms formed from this reaction then proceed to combine with an oxygen molecule to yield NO. Typically, the prompt mechanism contributes only small amounts of NO (<10 ppm) and is dominated by thermal NO at temperatures greater than approximately 1800 K (Correa, 1990).

2.5.3 - Fuel NO

NO formation can also occur due to organically bound nitrogen compounds present in the fuel itself. Light distillate fuels contain small amounts of fuel bound nitrogen (0.06%), but heavy distillates may contain as much as 1.8% (Lefebvre, 1983). The amount of NO formed via this process depends on the concentration of nitrogen within the fuel and the degree of nitrogen conversion. Because jet fuels do not contain significant amounts of nitrogen, aircraft applications are not concerned with the formation of fuel NO.

2.5.4 - NO_2 Emissions

In the previous sections, the three mechanisms for the formation of NO have been discussed. However NO_x consists of both NO and NO_2. The NO formed in the combustion zone is oxidized to NO_2 as soon as the low temperatures required for this reaction are reached (Lefebvre, 1983). This oxidation typically occurs after the exhaust gases leave the engine. This combination of NO and NO_2 are utilized to describe the total NO_x emitted from an engine.

2.6 - Advanced Combustor Concepts

In recent years, environmental concern has resulted in the enactment of regulations limiting the emissions of pollutants from both land-based and aircraft combustion applications. As a result, combustor design criteria have shifted from optimizing thrust to weight ratios to reducing pollutant emissions without significantly sacrificing performance. Emissions of NO_x, CO and UHC have been targeted by these regulations. However, Mother Nature has presented the combustion engineer a challenge in reducing both emissions of UHC, CO and NO_x. Figure 7 presents a plot of UHC, CO, and NO_x emissions versus equivalence ratio. For equivalence ratios near stoichiometric, the reaction temperature is high. These high temperatures are excellent for oxidizing UHC and CO, thereby completing the combustion of all fuel present. The conflict arises in that high temperatures promote the formation of thermal NO_x. The combustion engineer is faced with determining an optimum condition where both UHC, CO and NO_x emissions are limited. To accomplish this for aircraft gas turbines, three major concepts for low pollutant emission combustors are being studied as discussed in the following sections.

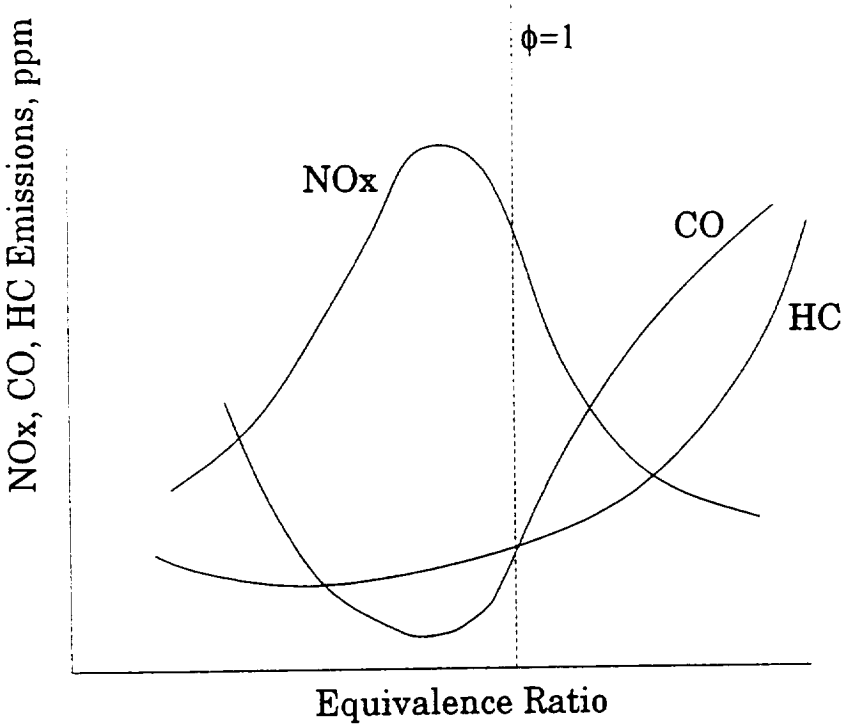

Figure 7 - Pollutant emissions versus equivalence ratio.

2.6.1 - Lean Prevaporized Premixed Combustion

The Lean Prevaporized Premixed (LPP) combustor was the first concept to appear to control NO_x in the early 70's (Tacina, 1990). The design objective of this concept is to attain complete evaporation of the liquid fuel and thorough mixing of the fuel vapor and air before combustion. By avoiding droplet combustion and by operating lean, nitric oxide emissions are drastically reduced. A schematic depicting the configuration of a LPP concept is presented in Figure 8. Problems with this system include

incomplete fuel vaporization and mixing, the danger of autoignition and/or flashback to premixing sections, poor lean blowout characteristics, and difficult light-up (Lefebvre, 1983).

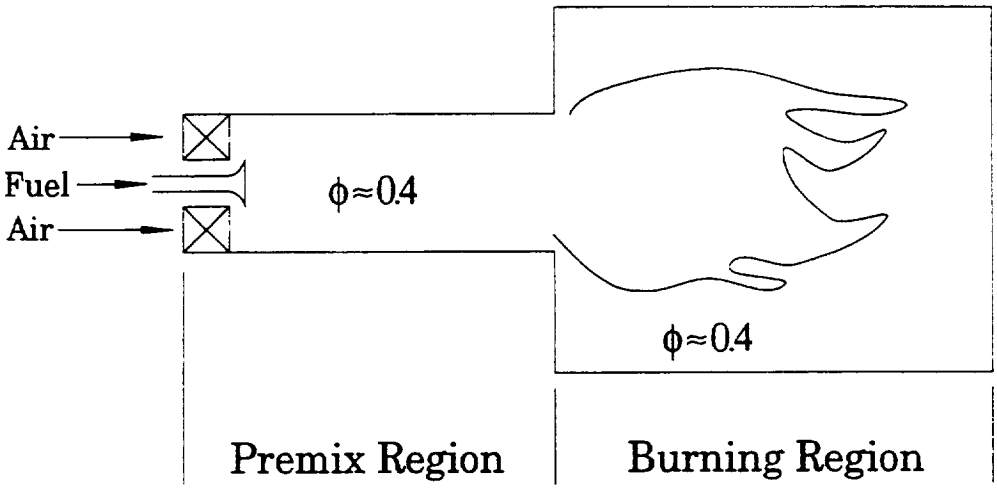

Figure 8 - Lean Premix/Prevaporize combustor concept.

2.6.2 - Rich-Burn/Quick Mix/Lean-Burn Combustor (RQL)

The RQL Combustor was initially developed to control the formation of NO_x from alternative fuels with large concentrations of fuel-bound nitrogen (Tacina, 1990). In the rich primary zone, the fuel bound nitrogen is not converted to NO_x due to the low temperatures and fuel rich environment. After the primary zone, the unburned fuel and hot products enter the quick mix section. The design goal of the quick mix section is to introduce large amounts of air and thoroughly mix the hot products as fast as possible. The

remaining products are then burned lean. The rich and lean burns are employed to prevent the formation of thermal NO. Therefore the quick mix section is crucial to the success of this concept. The quick mix section must mix well enough to prevent the stoichiometric pockets of fuel which lead to thermal NO. The advantage of the RQL combustor is that it provides the stability of a conventional combustor with reduced pollutant emissions. The major drawback is the increased length associated with the three sections. Figure 9 presents a schematic of the RQL combustor concept.

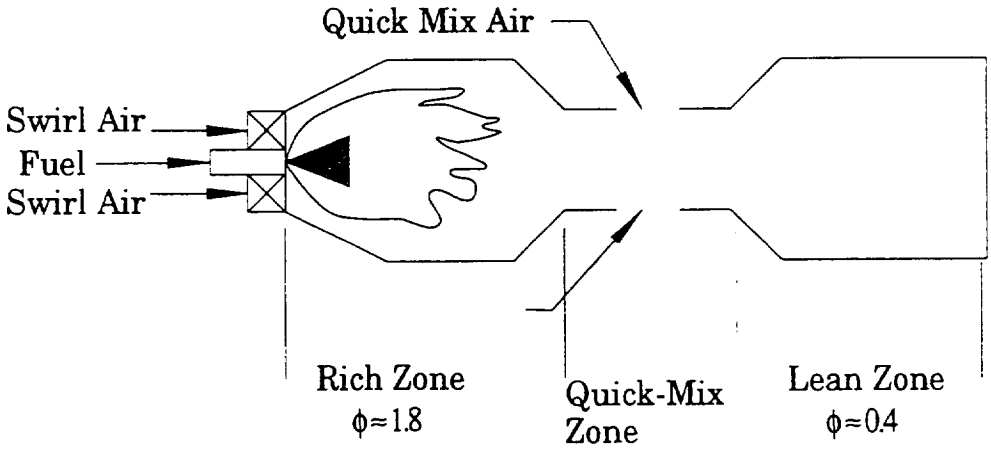

Figure 9 - RQL combustor concept.

2.6.3 - Lean-Burn Direct Injection Combustor (LDI)

For the LDI concept, all the combustion air enters the primary zone and the fuel is injected directly into the dome region. This eliminates the need for downstream mixing and cooling of hot products. Consequently the LDI equivalence ratio in the dome is leaner than conventional combustors. The

formation of thermal NO is reduced by operating the combustor lean. The major advantage of the LDI concept is its reduced complexity and length, which results in a reduction in the overall engine weight. The success of the LDI lies in the injection and mixing of the fuel. All fuel must evaporate and mix with the combustion air before burning to prevent stoichiometric pockets of fuel. Figure 10 displays the setup of the LDI combustor.

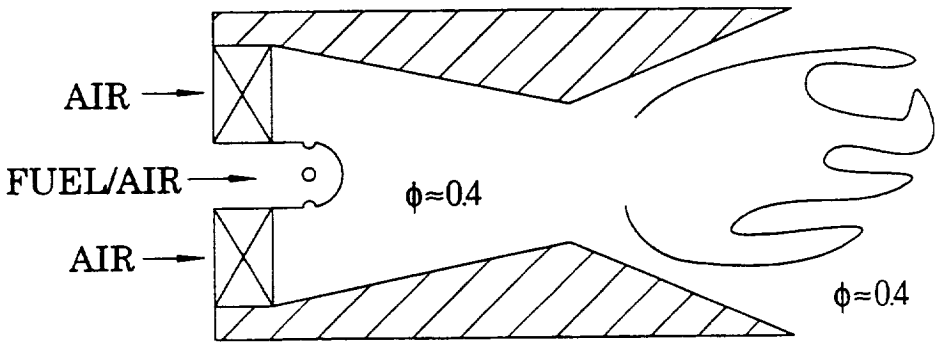

Figure 10 - LDI combustor concept (adapted from Shaffar, 1993).

2.6.4 - LDI Injector

The combustor developed by Shaffar (1993) demonstrates a dramatic reduction in the formation of thermal NO, meeting the NASA goal for emissions of NO_x. Detailed information on the development of this combustor is presented in a separate masters thesis (Shaffar, 1993). The fuel injector employed for this work is an eight port, radial, airblast nozzle. A schematic of the injector is provided in Figure 11. The fuel is injected

from eight evenly spaced 0.0135" holes and is immediately blasted by atomizing air from above and below. The fuel and air then exit through eight 0.088" holes. For the study, one port of this eight port radial injector is duplicated in order to study the factors influencing atomization.

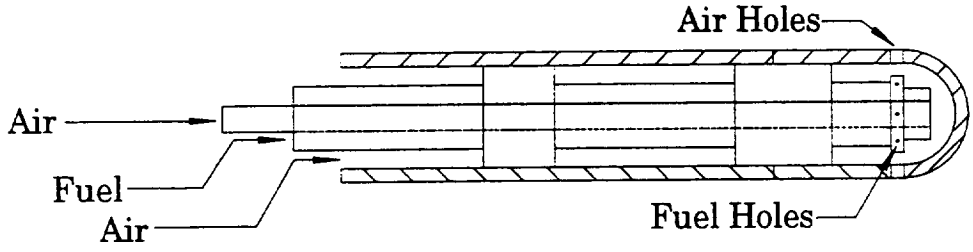

Figure 11 - Sectional view of LDI nozzle

2.7 - Atomization

In virtually all gas turbine aeroengine applications, liquid fuels are employed for both storage and safety reasons. Theses liquids must be atomized before being injected into the combustion zone and burned. Atomization is the process in which a volume of liquid is transformed into a multiplicity of small drops (Lefebvre, 1983). The goal of the atomization process is to produce a high ratio of surface area to mass in the liquid phase, resulting in high evaporation rates. An ideal injector would possess all of the following characteristics (Lefebvre, 1983):

1. Good atomization over the entire range of fuel flows.

2. Rapid response to changes in throttle setting.
3. Freedom from flow instabilities.
4. Low susceptibility to blockage by contaminants and to carbon buildup on the nozzle face.
5. Low susceptibility to gum formation by heat soakage.
6. Low cost, low weight, ease of manufacture, and ease of removal for servicing.
7. Low susceptibility to damage during manufacture and installation.

The following sections discuss airblast atomization and spray characteristics as they relate to the current work.

2.7.1 - Airblast Atomization

As the nozzle technologies have developed, airblast atomization has been adopted for both industrial and aircraft gas turbine applications. Airblast atomization utilizes the kinetic energy of a high speed airstream to disintegrate the liquid jet or sheet into droplets. This type of atomization promotes thorough mixing of the air and fuel before combustion, thereby providing potential for low soot formation and low flame luminosity. The major drawback of airblast injectors is their poor atomization at low air velocities, associated with low engine speeds. Under these conditions, the pressure drop across the liner is rather low and results in low air velocities through the injector. To avoid this problem, many airblast injectors include a pressure atomizing simplex nozzle as a pilot to achieve rapid lightoff and assist in high altitude relight.

Most of the work to date has focused on prefilming injectors. These prefilming injectors first spread the fuel out into a thin, continuous sheet of liquid and then introduce atomizing air from both sides. One example of a prefilming airblast atomizer designed for gas turbine use is depicted in Figure 12.

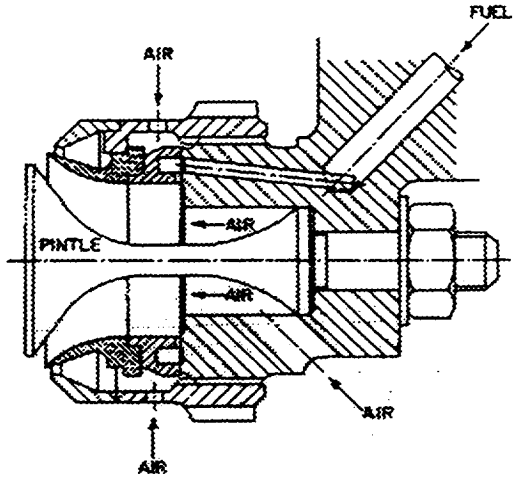

Figure 12 - Prefilming airblast atomizer (Bryan et. al., 1971).

As seen above in Figure 11, the injector developed by Shaffar is a plain-jet airblast nozzle. Under similar conditions, the performance of the prefilming injector appears to be superior to that of the plain-jet injector (Rizkalla and Lefebvre, 1975). However, the prefilming injector design tends to be much more complex than the plain-jet injector. The fuel is introduced through simple holes in the plain-jet injector, which reduces the complexity of the

hardware considerably. The plain-jet injector, seen in Figure 11, provides both excellent atomization and a simple, rugged design.

2.7.2 - Spray Characteristics

Several characteristics of sprays are classified as directly influencing combustor performance (Lefebvre, 1983). These include: mean drop size, drop size distribution, patternation, cone angle, and penetration.

The mean drop size is often used as a method for comparing the atomization qualities of various sprays. One commonly used mean drop size is the Sauter Mean Diameter (SMD). It is defined as the surface area mean diameter based on distribution moments (Sowa, 1992) and is expressed as follows:

$$SMD = \frac{\sum nD^3}{\sum nD^2} \tag{13}$$

Due to the random nature of the atomization process, a wide variety of drop sizes are produced. In modern gas turbine engines, the drop size distribution normally ranges from 10 to 400 μm. The drop size distribution is critical to the performance of the combustor, because large droplets tend to increase emissions of NO_x. Large droplets result in local stoichiometric packets which burn very hot. Using SMD to determine injector performance is sometimes misleading in that two widely different distributions can

result in the same SMD. The distribution minimizing the number of large droplets is normally preferred. An instructive picture of the drop size distribution can be obtained by plotting a histogram of drop sizes, seen in Figure 13. If a sufficiently large sample is recorded, the bin size on the histogram, Δx, can be reduced, yielding the frequency distribution curve, overlaid on Figure 13. In addition to the frequency curve, a cumulative distribution curve is often employed. This is essentially a plot of the integral of the frequency curve and is presented in Figure 14. The cumulative distribution curve represents the percentage of the total surface area or volume of a spray contained in drops below a given size.

Patternation is defined as the uniformity of the circumferential distribution of fuel in a conical spray (Lefebvre, 1983). Poor patternation results in local pockets of fuel and air which are appreciably richer or leaner than the designed fuel/air ratio. This results in a poor pattern factor and increased pollutant emissions. The LDI injector, currently being studied, improves patternation by spraying radially from equally spaced circumferential ports.

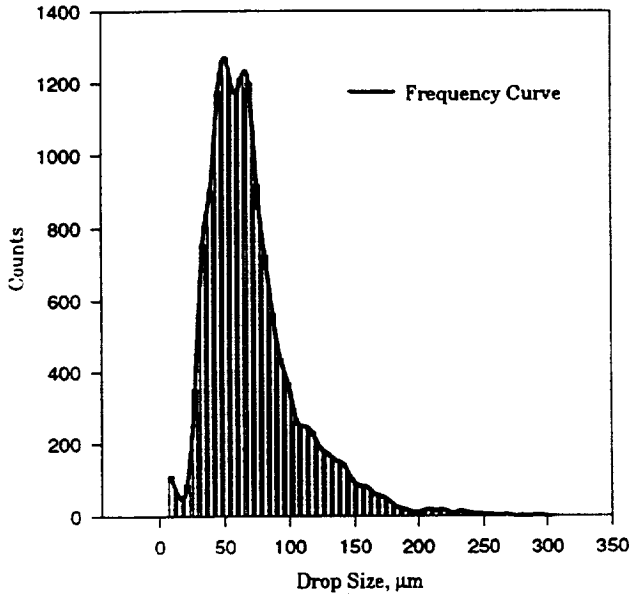

Figure 13 - Histogram of drop sizes and frequency distribution curve.

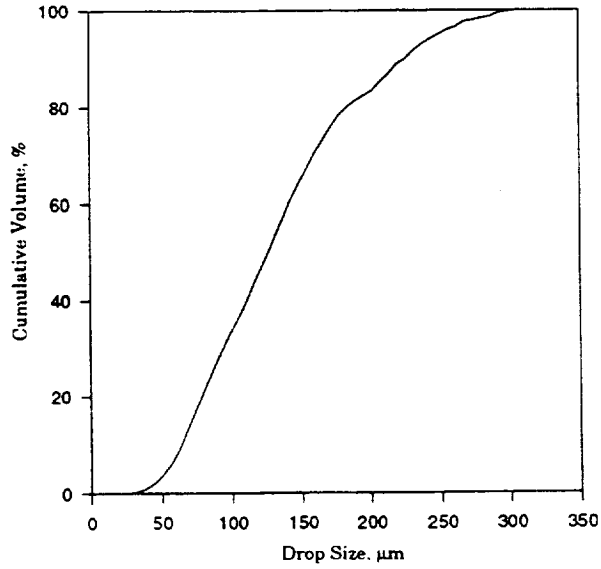

Figure 14 - Cumulative drop size distribution curve.

The cone angle is defined as the angle measured from the centerline of the spray out to the edge of the spray. Typically, a larger cone angle promotes better atomization due to increased exposure to the surrounding air. This spray characteristic is limited to axially spraying nozzles. It is difficult to define a cone angle for the LDI injector, because it sprays radially.

The dispersion of a spray relates to the degree of fuel uniformity over a given combustor space. The degree of dispersion can be thought of as the ratio of the volume of the spray (i.e. the physical space covered by the entire spray) to the volume of the fuel contained within it. An optimum injector produces a perfectly uniform mixture of fuel and air over the desired spray area. The advantage of good dispersion is rapid mixing of the fuel and surrounding gas, resulting in high rates of evaporation and heat release (Lefebvre, 1983). Many statistical functions, including the standard deviation, are employed to determine quantitatively the degree of dispersion. A measure of unmixedness, based on the variance of the fuel concentration distribution, is commonly employed. This measure is termed

the spatial unmixedness and can be calculated with the following equation (Liscinsky et. al., 1995):

$$U_S = \frac{c_{var}}{c_{avg}\left(1 - c_{avg}\right)} \tag{14}$$

where,

$c_{var} = \frac{1}{m}\sum_{i=1}^{m}\left(\bar{c}_i - c_{avg}\right)^2$ = spatial concentration variance

$\bar{c}_i$ = time-averaged concentration at a point

c_{avg} = fully mixed concentration

U_s equal to zero corresponds to a perfectly mixed system, and U_s equal to unity represents a perfectly unmixed system. Additionally, plots of mixture fraction present information on the distribution of fuel within a given spray area.

The penetration of a spray may be defined as the maximum distance the fuel drops reach when injected into the surrounding air. This spray characteristic is governed by the relative magnitudes of two opposing forces: the kinetic energy of the initial fuel/air jet and the aerodynamic resistance of the surrounding gas (Lefebvre, 1983). The penetration of drops is a critical parameter in determining the pattern factor of the combustor and the pollutant emissions. For the radially injected LDI nozzle, penetration must be optimized to improve combustor performance. Underpenetration of the spray results in a hot core of gases surrounded by a ring of cool air.

Overpenetration of the spray creates a situation where drops are colliding with the combustor wall, running down, and dripping away. Obviously, both of these conditions yield increased pollutant emissions and degraded pattern factors.

2.7.3 - Plain-Jet Airblast Injector Studies

The plain-jet injector type has also been the focus of a few studies which will now be discussed. The first study on a plain-jet airblast injector was conducted over 50 years ago (Nukiyama and Tanasawa, 1939). The experimental setup employed for this study is presented as Figure 15. This type of injector is termed co-flowing because the air and fuel are traveling in the same direction. The major conclusion from this study is in the form of the following empirical equation for the SMD:

$$SMD = \frac{0.585}{U_R}\left(\frac{\sigma}{\rho_L}\right)^{0.5} + 53\left(\frac{\mu_L^2}{\sigma\rho_L}\right)^{0.225}\left(\frac{Q_L}{Q_A}\right)^{1.5} \qquad (15)$$

From this equation, several important conclusions can be drawn. For low viscosity fuels, the relative velocity (U_R) between the fuel and air is inversely proportional to SMD. Additionally, for high air-to-liquid ratios, the influence of viscosity on SMD becomes negligible.

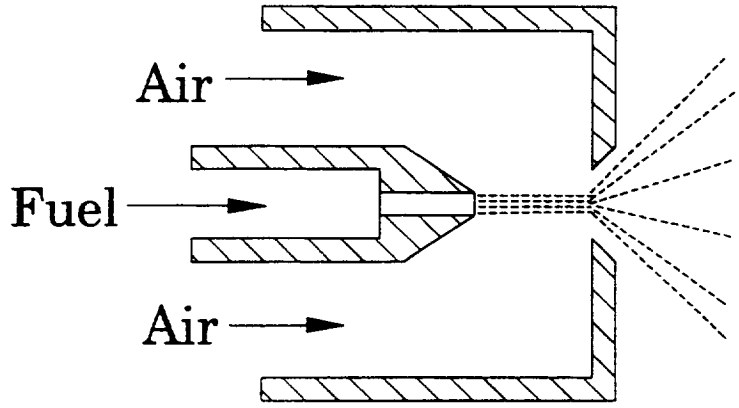

Figure 15 - Plain-jet airblast atomizer (Nukiyama and Tanasawa, 1939).

The performance of plain-jet atomizers was also investigated by Lorenzetto and Lefebvre. This study tested a wide range of liquid properties, flow conditions, and injector geometries (Lorenzetto and Lefebvre, 1977). The experimental setup employed was that of a co-flowing injector and is presented in Figure 16. The major conclusions drawn from this study are as follows:

1. The mean drop size of the liquid spray increases with increases in liquid viscosity and surface tension and decreases in liquid density.
2. Atomization quality is improved by an increase in air/liquid ratio and by a reduction in liquid flow rate.
3. For low viscosity liquids, little improvement in atomization quality is gained by raising the ALR above a value of approximately five.
4. For liquids of low viscosity, the mean drop size is inversely proportional to air velocity.

5. For low viscosity liquids, the size of fuel injection orifice has virtually no effect on drop size. For high viscosity liquids, a reduction in fuel jet diameter improves atomization.

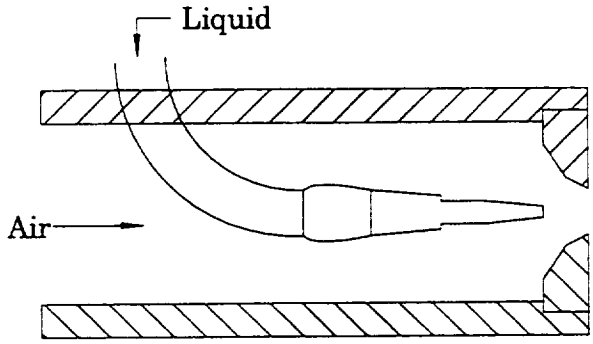

Figure 16 - Lorenzetto-Lefebvre plain-jet airblast atomizer.

2.7.4 - Current Mechanistic Spray Study

For the current study, the focus is centered on proposing and demonstrating an experiment to examine on a mechanistic level, the processes associated with atomization, penetration, and dispersion of a liquid jet introduced from a radial plain-jet airblast injector into a crossflow of air. The experimental setup employed is presented in Figure 17. One major difference between past studies and the present one becomes readily apparent. The air in the current design is not co-flowing and must transition from traveling at a right angle to the fuel to traveling in line with the fuel at the injector air

hole. The major variations center on where the fuel is injected relative to the air hole and the geometry of the fuel injector. Further information on the details of this injector are provided in the experimental setup section.

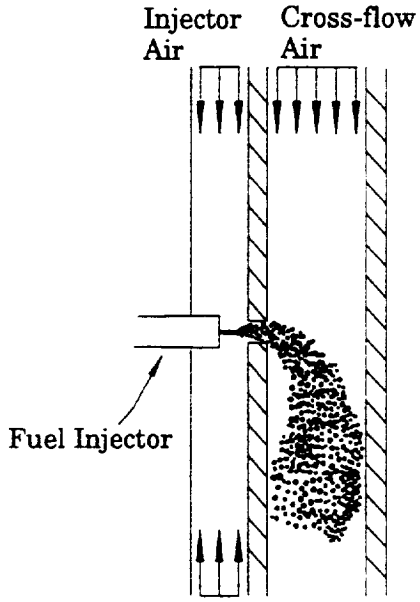

Figure 17 - Mechanistic spray study setup.

Chapter 3.0 - Approach

The approach utilized in this thesis stems directly from the goal of establishing an experiment to (1) obtain a mechanistic understanding of the atomization process, and (2) characterize the fuel preparation and injection characteristics of a liquid jet injected radially into a high velocity cross-stream. The overall performance of the nozzle has previously been demonstrated (Shaffar, 1993). However, optimization and analysis of the current injector design has not been completed. The approach used to satisfy this goal is summarized by the following, five objectives:

- Duplicate and manufacture a single port of the LDI, eight-port injector.
- Design and manufacture a crossflow region to simulate the swirler air from the LDI combustor and provide optimum, optical access to the injector hole exit region.
- Modify spray test facility to provide the desired air and fuel flow rates for both the injector and crossflow region.
- Select appropriate optical diagnostics and apply these diagnostics to the detailed measurement of properties considered important to the characterization of spray performance.
- Analyze and document the experimental data.

The first step was to duplicate a single port of the LDI injector. In addition to this objective, several other design items were required of this single port injector. Variation of fuel injection location and hole size were additional desired features. This lead to the experimental setup described in the following chapter.

Next the air crossflow hardware was designed to accommodate the injector and still provide optical access to the injector hole region. The use of a flat plate for the injector's front face required the crossflow region to be rectangular in shape. Therefore this hardware was required to convert circular pipe flow into a uniform, rectangular region of air flow. The physical items utilized to accomplish this task are detailed in Section 4.2.

The spray facility used for the current testing was modified to incorporate the following features: 1) a frame to support the crossflow and injector assemblies, 2) a three dimensional traverse to allow precise positioning of the hardware, and 3) a high-capacity air circuit to provide the required flow rates to the crossflow region.

Two non-intrusive laser diagnostics were selected to provide the desired information without perturbing the flow of interest. Phase Doppler Interferometry (PDI) was chosen to supply information on droplet sizes and

velocities. Planar Liquid Laser Induced Fluorescence (PLLIF) was selected to provide information on spray area and dispersion. Further detailed information on these diagnostics can be found in Section 4.4.

Finally, all testing was conducted at standard pressure and temperature. Testing at elevated temperatures and pressures more accurately simulates the conditions within a gas turbine engine. However, atmospheric testing provides a much friendlier environment, which is both much simpler and less expensive than high pressure testing. Additionally, atmospheric testing allows easy optical access to the hardware. Due to the use of laser diagnostics, optical access to the spray was of vital importance.

4.0 - Experimental Setup

The description of the experiment is divided into four major sections. The first section deals with the atomizer and associated operating conditions and geometry variations. The second section describes the hardware required to provide a uniform crossflow of air. The third section provides a brief overview of the test facility utilized. The final section describes the two laser diagnostics employed for this spray research.

4.1 - Airblast Injector

As seen in Figure 12, air within the LDI injector approaches the exit holes from above and below via a 0.125 in. (3.18 mm) annulus. The fuel ring portrudes into this annulus a distance of 0.0625 in.(1.59 mm), thereby restricting the flow further before both the fuel and air leave the exit holes. To simulate this design, the current injector depicted in Figure 18 (cross-sectional view) was developed. As seen in the figure, two air circuits are provided to allow air to approach the exit hole from either above and/or below. If desired, either air circuit can be blocked to allow air to enter only from above or below. The air circuits are attached to the injector via two 0.5 in. Swagelock unions (SS-400-1-4W). The air from both circuits then passes into a 0.125 in. by 0.75 in. (3.18 mm by 19.1 mm) rectangular passage. This passage is formed by sealing the injector assembly onto the back of the

injector panel. The injector panel is simply a 0.125 in. thick flat plate (3.75 in. wide by 8.125 in. long) with a 0.088 in. (2.24 mm) hole drilled to provide the exit hole for the injector. The injector panel and injector assembly are held together with a bracket, which provides a bolt hole pattern on the front for the injector panel and a second bolt hole pattern on the back for the injector assembly. The injector assembly and plate are also sealed together with a standard gasket material.

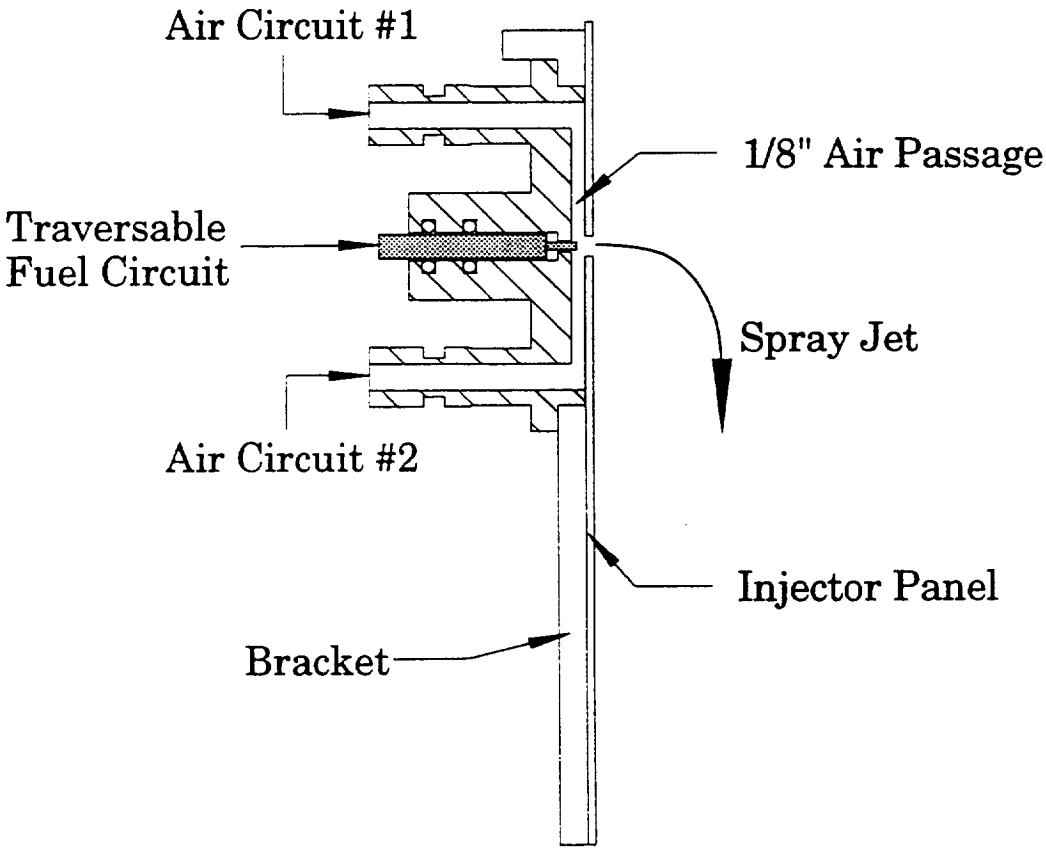

Figure 18 - Airblast injector configuration

A second feature of the injector assembly is a 0.756 in. (19.2 mm) hole which provides a passage for various fuel tubes. This feature allows both variations in the geometry of the fuel tubes and the location of injection of the fuel. The fuel tube is sealed off from the room by a O-ring design. This design was incorporated to allow the fuel to be injected at any height across the 0.125 in. passage between the injector assembly and panel. As stated previously, the fuel tip designed by Shaffar protrudes 0.0625 in. into the 0.125 in. passage. The fuel tubes utilized for the current study are depicted in Figure 19. Figure 19a presents the fuel tube which duplicates the Shaffar design. The width of this tip and the fuel hole were sized to match Shaffar's design. The other two variations in geometry were included to determine the effect geometry has on the atomization quality. The fuel hole size for the angled tip injector is similar to the Shaffar design (0.0135 in. dia., 0.343 mm), but the hypodermic injector hole size is 0.023 inch (0.584 mm) in diameter.

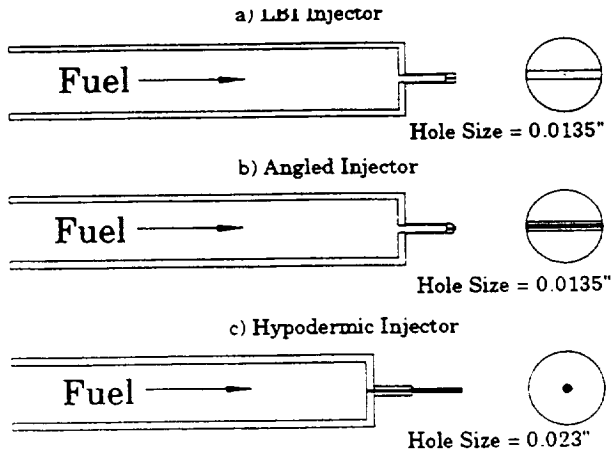

Figure 19 - Fuel tube configurations

This configuration, with injector assembly, bracket, and injector panel, also allows the size of the exit hole to be easily varied. By simply unscrewing the injector panel from the bracket, a new panel with a different hole size or shape can be tested.

4.2 - Crossflow Air

As seen in the schematic of the LDI combustor concept, Figure 10, swirler air passes by the injector holes and bends the spray downstream. To simulate this design, crossflow air is required. Therefore this study was conducted in a 3 in. by 4 in. (76.2 mm by 101.6 mm) wind tunnel, with the airblast injector panel serving as one wall. A schematic of the wind tunnel setup is presented in Figure 20. Air first enters the 5.25 in. (133.5 mm) diameter tunnel plenum via a 2 in. diameter pipe. This air immediately passes through a section of very fine grid to distribute the air more uniformly. However, at this point the air is still in the form of a discrete jet. To breakup this air jet, a circular impingement plate is placed immediately downstream of the first grid. Five 0.5 in. (12.7 mm) holes drilled in this plate prevent a large recirculation zone downstream of the plate, while still serving to breakup the jet and distribute the air across the entire plenum section. The air then passes through two additional pieces of screen to ensure a uniform velocity profile within the wind tunnel plenum.

However, the air is still in the form of circular pipe flow. A transition piece was designed to convert circular pipe flow to the desired rectangular crossflow. This piece was designed to provide a very smooth transition, free from vorticies. After passing through the transition piece the crossflow air enters the main testing section. This section is the previously described 3 in. by 4 in. wind tunnel. One wall of this rectangle is the injector panel specified in Section 4.1. Opposing the injector panel is a solid steel panel. Optical access to the test section is provided by two optical quality 0.125 in. quartz windows. These two windows oppose each other and complete the rectangular wind tunnel test section.

A uniform velocity profile is crucial to accurate measurements within the test section. Any high or low velocity regions in the test section will certainly affect the penetration and dispersion of the spray. Therefore, extensive Laser anemometry measurements were conducted to verify the presence of a uniform velocity profile over the entire cross-sectional area. The results of these measurements can be found in Appendix A.

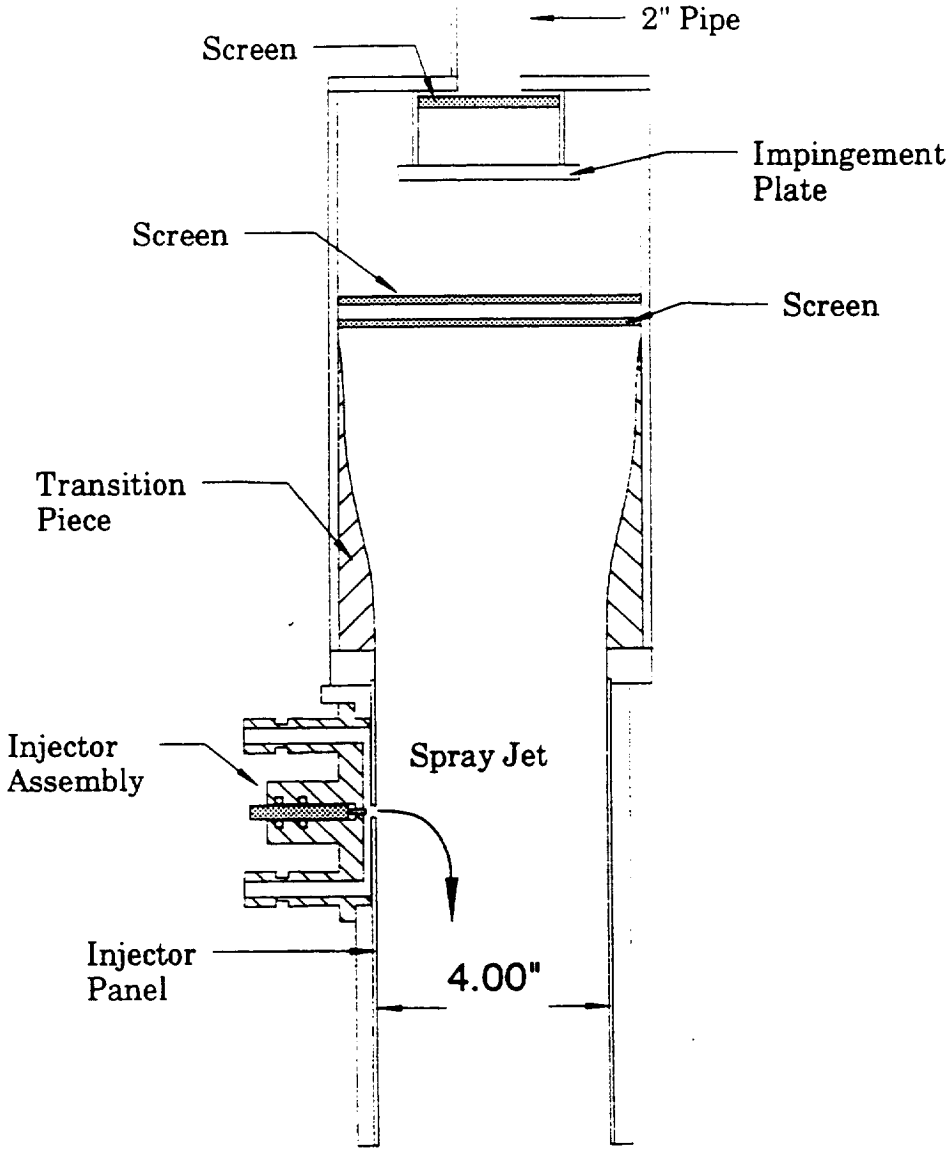

Figure 20 - Crossflow air hardware setup

4.2.1 - Reduced Cross-sectional Area Hardware

A second set of experimental hardware for the crossflow air has also been designed and fabricated. This new hardware is designed to provide a much smaller cross-sectional area. For the previously defined hardware, the distance from the injector panel to the opposing wall is 4 inches. This setup simulates an unconfined jet-in-crossflow. The second set of hardware is required to simulate the distance from the injector holes to the quarl wall in Shaffar's LDI combustor concept. The distance from injector holes to the opposing wall for this setup is 0.712 inches (18.1 mm). This hardware provides a confined test, in which the dispersion and penetration of the spray can be determined for the actual LDI geometry. Three additional pieces of hardware are required to convert the wind tunnel down to the reduced cross-sectional area: a transition piece, transition piece endplate, and smaller quartz windows.

4.3 - Spray Test Stand

The spray test stand flow delivery circuits are presented in Figure 21. The Engineering Laboratory Facility (ELF) has three Ingersoll-Rand compressors that each supply the laboratory with 1200 SCFM of dried air at a nominal pressure of 150 psig. The air from these compressors is first

dried and then filtered before entering the test cells. After entering the test cell, the air is divided into a low capacity line and a high capacity line. The high capacity air line was installed to deliver the large SCFM air flows required by the crossflow air. Following the high capacity line, the air is first filtered (Norgren model # F18-C00-A3DA) and regulated down to a pressure of 110 psig (Norgren model # R18-C06-RGSA). The air then flows into a manifold where it supplies two high capacity rotometers. The back pressure on the rotometers is first set by a second regulator (Norgren model # R17-B00-RNLA). The air then travels through the rotometer (Rotometer: Brooks model # R-12M-25-5 / Float: Brooks model # 12-LJ-740 SS) and is metered with a needle valve on the exit side of the rotometer. Both rotometers in this parallel circuit were calibrated with a Merriam Laminar Flow Element (LFE Model # 50MC2-6). The maximum airflow through each rotometer was found to be approximately 500 SCFM. Air from each rotometer was then sent to the 2 in. pipe which supplies the crossflow section described in Section 4.2. For the 3 in. by 4 in. wind tunnel hardware, both rotometers were required to achieve the desired crossflow velocities within the test section. For the 3 in. by 0.712 in. wind tunnel hardware, only one rotometer was typically required.

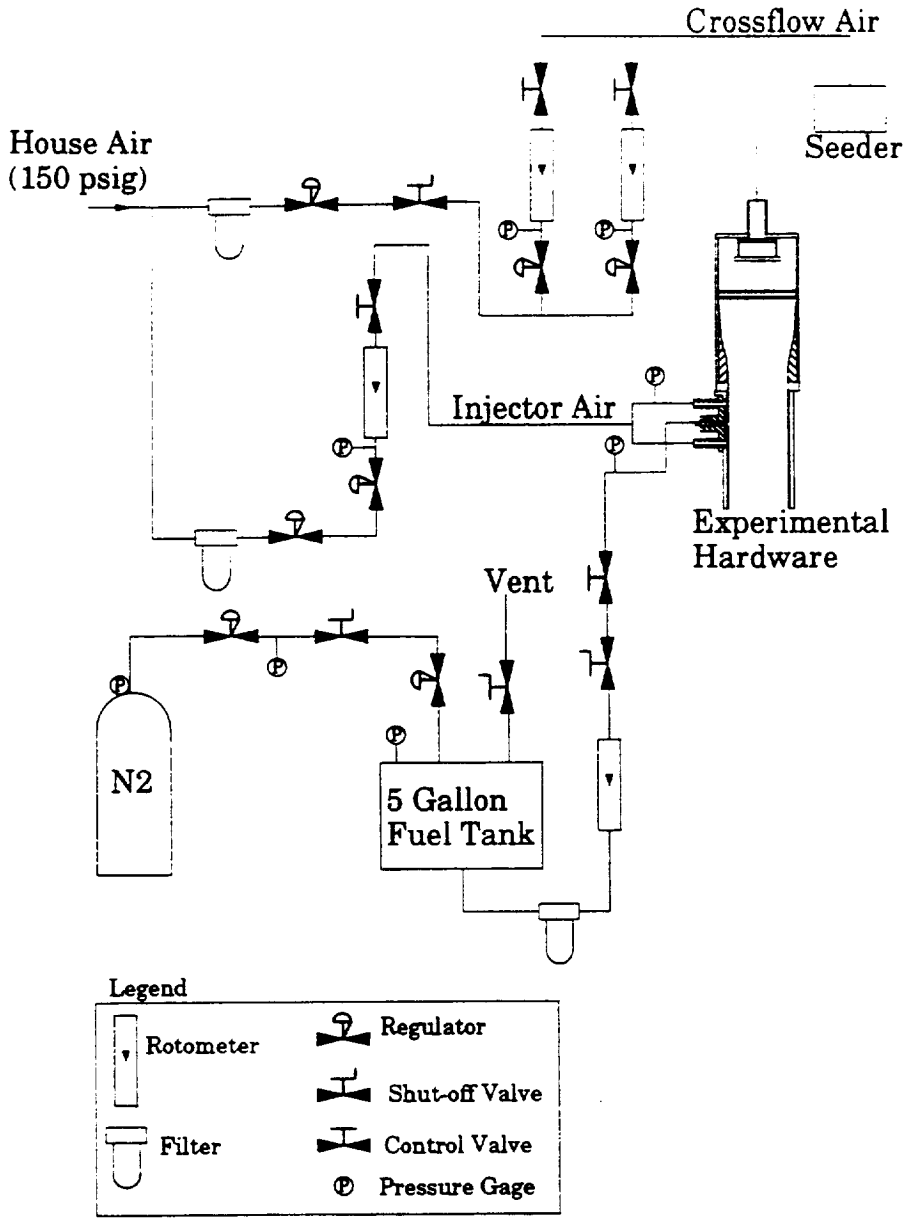

Figure 21 - Test facility flow schematic

The air required by the injector is delivered from a rotometer on the low capacity air circuit. For this circuit, air is filtered and regulated down to 80 psig. A similar configuration to the crossflow rotometer is applied with the

regulator, rotometer, and needle valve. A small float (Brooks model # R-8M-25-4) was employed to provide fine adjustment for the delivery of nozzle air. This float/rotometer system provided a range of 0-5 SCFM over the 0-100 scale reading. The air was then sent to the injector and divided to provide air to both air circuits, described in Section 4.1.

The fuel delivery system is also depicted in Figure 21. Fuel was supplied from a 5 gallon stainless steel tank that was pressurized with nitrogen. The nitrogen tank was regulated down to a pressure of 100 psig and then sent into the test cell. A second regulator, located at the fuel tank, was used to set the desired fuel flow rate. The fuel was then filtered and sent through a calibrated rotometer (Brooks model # R-2-15-B) and delivered to the fuel tube.

Bubbles in the fuel line presented a major problem especially at low fuel flow rates. As bubbles violently pass through the fuel tube, a great improvement in atomization is realized and pulsations in the fuel delivery result. These bubbles are typically formed by cavitation as the fuel progresses past the needle valve on the back side of the rotometer. To avoid this problem the needle valve was completely opened and the pressure within the fuel tank was set just high enough to drive the desired fuel flow rate to the fuel tube. Secondly, if left pressurized for long periods of time,

the nitrogen used to pressurize will diffuse into the fuel and result in more bubbles upon delivery. To prevent this problem the fuel tank was relieved of pressure when not in operation.

4.4 - Diagnostics

Two laser diagnostics were utilized throughout the course of this spray study. Phase Doppler Interferometry (PDI) was used to make spatially-resolved measurements of droplet size, veloctiy, and mass flux as well as continuous phase velocity. This technique has proved extremely useful in characterizing droplet interactions in complex flows such as airblast atomization (McDonell and Samuelsen, 1988). PDI also has the distinct advantage of differentiating the continuous phase (i.e. gas) from the discrete phase (e.g. droplets). For the current study, PDI was mainly utilized to provide a quantitative measure of atomization within the spray. Further discussion of theory and hardware associated with PDI is provided in Sections 4.4.1 and 4.4.2.

The second laser technique employed in this spray research is Planar Liquid Laser Induced Fluorescence (PLLIF). This technique uses a Charged Coupled Device (CCD) camera to take a photograph of the spray. PLLIF provides a relatively quick method for quantitatively describing the area

and dispersion of a spray. However, no information on the level of atomization is determined with this technique. Therefore coupling PLLIF with PDI results in a complementory setup, which provides extremely detailed spray information. Further information on the theory and setup of the PLLIF system is described in Sections 4.4.3 and 4.4.4.

4.4.1 - Phase Doppler Interferometry Theory

The phase Doppler (PD) approach is an interferometric based optical scattering method. An interferometer, defined in Webster's Dictionary, is any of several optical, acoustical, or radio-frequency instruments that use interference phenomena between a reference wave and an experimental wave, or between two parts of an experimental wave, to determine wavelengths, wave velocities, distances, and directions. With PDI, the probe volume consists of a region of light and dark fringes, similar to laser anemometry. Droplets passing through the probe volume scatter light which produces a far field interference fringe pattern (Bachalo, 1987). The spacing between these projected fringes is directly proportional to the drop diameter. Two detectors (photomultipliers), located in space with known separation, are employed to measure this interference fringe pattern (Bachalo and Houser, 1984). A schematic of this phase shift is presented as Figure 22. The phase shift is then determined by measuring the time

between zero crossings from detectors 1 and 2 and dividing by the measured Doppler period. This phase shift is then related to the particle size. To eliminate ambiguity associated with spatial phase shifts of over 360 degrees, and to extend the dynamic range, a third detector is included in the receiving optics (Bachalo, 1987). The temporal frequency of the measured signal is proportional to the particle velocity component in the plane of the beams (Bachalo and Houser, 1984).

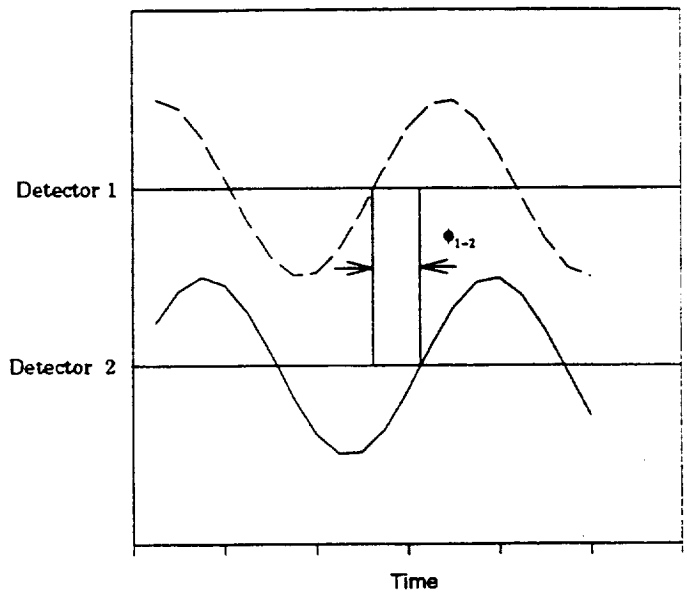

Figure 22 - Simultaneous signals from detectors 1 and 2

4.4.2 - Two-Component Phase Doppler Instrument

Figure 23 presents a schematic of the two-component phase Doppler interferometric system. The transmitter optics (Aerometrics Model 1100-3S) can be seen in Figure 23a. A 1 watt Ar^+ Laser (Lexel Model 85) drives the transmitter. A dichroic mirror within the transmitter splits the beam into a green beam (514.5 nm) and a blue beam (488.0 nm). The beams are next passed through a chromatic filter to ensure that no other wavelengths are present in the probe volume to be formed (McDonell and Samuelsen, 1988). Additionally, the polarization of the blue beam is rotated 90 degrees from that of the green beam. The resulting beams are then focused onto a diffraction grating which splits each beam into ordered pairs. To discriminate flow direction and to broaden the velocity range, the diffraction gratings are rotated to provide frequency shift. The two first order beams of each wavelength are then collimated, and focused by a transmitter lens to form the two-component probe volume.

The layout of the receiving optics and detectors (Aerometrics Model 2100-3) is depicted in Figure 23b. A f/5 receiver lens collects the light scattered by particles passing through the probe volume. The interference fringe pattern image collected by the front lens is focused onto a 100 micron by 1mm slit. The resulting image is then collimated and split into four areas as indicated

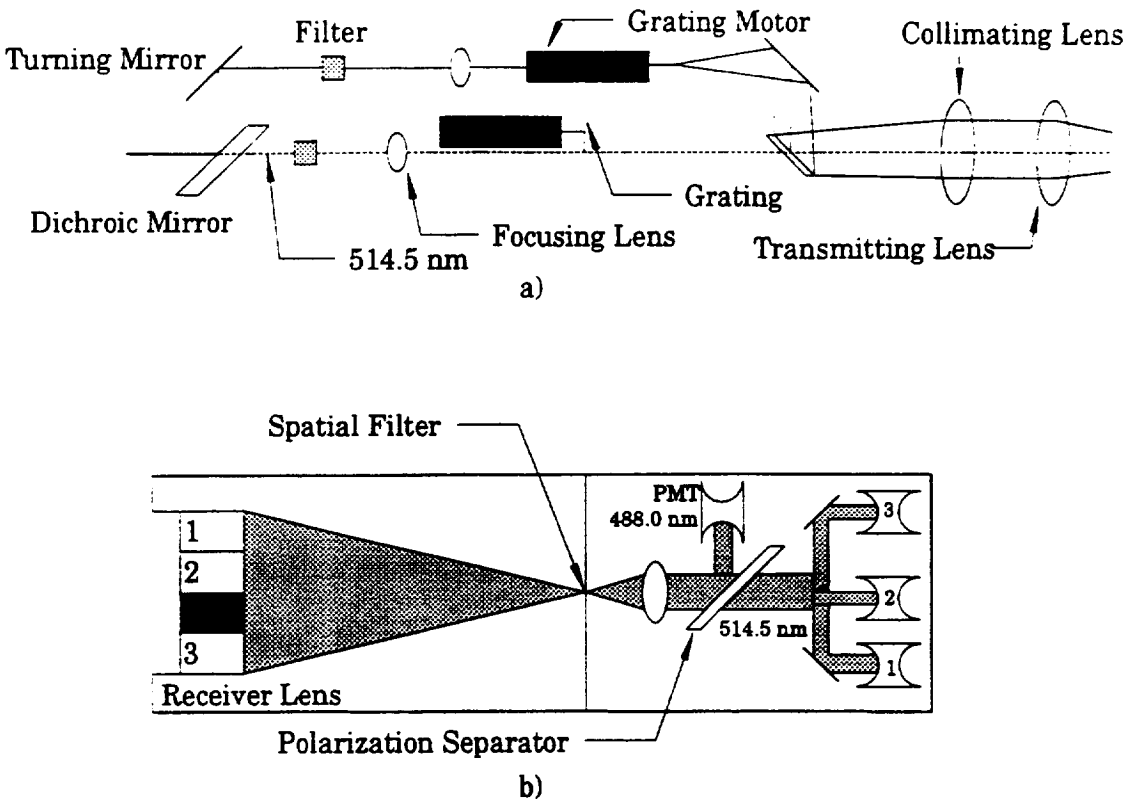

Figure 23 - Phase Doppler transmitter and receiver

in Figure 23b. Three of the four areas are examined by a different photomultiplier. As discussed previously, one component of velocity is determined by the temporal frequency of the Doppler burst obtained by detector 1. A polarization beam splitter separates the signals from each component, and a fourth detector is used to obtain the signal for the second component of velocity (McDonell and Samuelsen, 1988).

The photodector gains, signal processing, frequency shifting, and data reduction are accomplished with a Compaq personal computer. A software

package is furnished with the hardware that allows the user to input all required information for operation of the unit, such as desired velocity and drop sizing ranges, etc. Additionally, a data reduction package is supplied which allows analysis of the aquired data. However, for the current study, most of the PDI information was extracted into a useful form via computer programs written by members of the UCI combustion laboratory. These programs output in column format a variety of desired information, such as each component of velocity, drop sizes, drop size distribution, corrected counts, shear stress, etc.

4.4.3 - Planar Laser Induced Fluorescence Theory

Laser induced fluorescence (LIF) is a well-established technique for detecting population densities of atoms and molecules in specific quantum states (Hanson, 1986). Recently LIF has been recognized as a powerful fluid mechanics diagnostic with the potential for monitoring flowfield parameters such as mixture mole fractions, temperature, velocity, and distribution of mass in sprays (Hanson, 1986). For the current spray work, PLLIF was utilized to provide a quantitative measure of the distribution and dispersion of liquid droplets.

A laser source is tuned to excite a specific electronic absorption transition in a species of interest. Typcially, the liquid or gaseous flowfield is doped with a chemical species known to fluoresce when excited by a particular wavelength of light. Following the absorption process, collisional redistribution in the electronically excited state may occur prior to either collisional quenching or radiative de-excitation (fluoresence) of the molecule back to a lower electronic state (Hanson, 1986). The emission, which occurs over a range of wavelengths, is usually collected at right angles and filtered spectrally at the photodetector. This is typically accomplished with a CCD camera fitted with an appropriate filter to only pass the fluoresence while blocking out the other emission wavelengths. The governing equation for the LIF signal, S, can be expressed as follows (Hanson, 1986):

$$S = CEVN_S BF_{vj}(T)[A/A+Q] \tag{16}$$

Here, C is a group of constants specific to the experimental setup, E is the laser energy per pulse per unit area per unit frequency, V is the measurement volume for the detector element, N is the number density of the absorbing species, F_{vj} is the population fraction for the pumped state, B is the Einstein coefficient for absorption, A is the Einstein coefficient for spontaneous emission, T is the temperature, and Q is the electronic quench rate. By making the assumption that these values remain fairly constant for a given system, the following expression can be utilized:

$$S \propto VN_S \propto \text{mass} \tag{17}$$

For the current study, this is the basic premise utilized. A quantitative measure of the exact amount of mass present at any given pixel was not required for the current work. Therefore equation 17 allows a measurement of the distribution of mass within the spray.

4.4.4 - Planar Liquid Laser Induced Fluorescence Setup

The source for the planar laser sheet was an argon ion CW laser emitting at 488nm. Throughout the experiment, the power was set to 1 watt. The beam was directed through a series of mirrors before entering a cylindrical lens. The cylindrical lens forces the beam to begin expanding radially outward. The beam, which was now an expanding sheet (~120 X 0.3 mm^2), was next passed through a convex lens, which neutralized the expansion, and resulted in a collimated sheet. The edges of the sheet were then blocked such that the sheet passed immediately adjacent the opposing steel walls of the wind tunnel.

The images were acquired using an intensified CCD camera (Xybion Model ISG-250) with a f/2.5 zoom lens (Canon Model V6x 18-2.5). A sharp cut filter (HOYA Y-52) was also placed on the camera to eliminate scattered laser light while allowing fluorescence emissions to pass through. The camera gating and gain were controlled through a camera control unit

(Xybion Model CCU-01). A frame grabber (Imaging Technologies PC Vision Plus), installed on a i486 personal computer, was employed to acquire the images. The images were obtained through multiple exposures (32) and held in RAM. The gating time of the camera was set at 9 μsec for each exposure. These 32 images were then averaged and saved on disk. For all the images recorded, the camera was positioned at an angle of approximately 23 degrees relative to the horizontal plane. Physical limitations prevented the camera from being positioned more perpendicularly to the laser sheet.

The spray fluid utilized for all testing was Methanol (Fischer Scientific A400 ACS Certified) doped with fluorescein dye (Aldrich F245-6). Although Jet-A is a more common fuel for aircraft applications, fluorescein and Jet-A are immiscible. Because the density, viscosity, and surface tension of methanol reasonably approximates that of Jet-A, methanol was selected as the working fluid for all testing. The concentration of fluorescein was held constant at a value of 0.1 mmol/liter. Further information on the PLLIF setup, utilized for this study, is described elsewhere (Igushi et. al., 1993). Additional work, validating the accuracy of this setup, has also been completed (Thamban et. al., 1994).

4.5 - Spray Test Stand

The setup of the two diagnostic systems and the experimental hardware is presented in Figure 24. In this figure, the back side of the injector and injector panel is seen. The crossflow air is travelling vertically downward toward the exhaust section. The experimental hardware is fastened to a X,Y,Z traverse, which allows precise positioning of the hardware at any location with respect to the laser diagnostics. Both laser diagnostics remained in place for the duration of the testing and the experiment was simply traversed back and forth between the diagnostics.

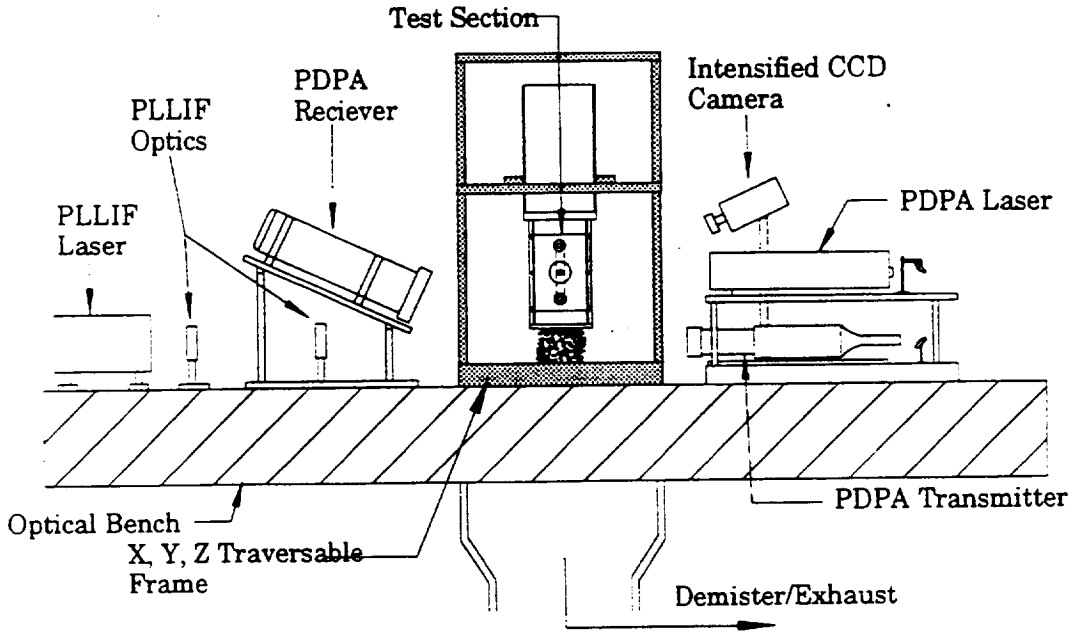

Figure 24 - Spray test stand setup

Chapter 5.0 - Results

Chapter 5 is divided into five major sections. The first section (Section 5.1) presents results on the characterization of a baseline radial injector at various flow conditions. Using PDI and PLLIF measurements, injector performance is described utilizing four flow characteristics: *penetration, spray area, fuel uniformity,* and *atomization*. For the current work, *penetration* is defined as the distance from the injector panel wall to the center of mass of the spray. The center of mass is determined utilizing PLLIF images and an imaging package termed Image Pro Plus. *Spray area* is defined as the physical coverage of the spray and is again calculated utilizing Image Pro Plus. For Image Pro Plus to calculate the *spray area*, a gray-level value must be specified. Any value below the specified is classified as out of the *spray area*. For all images presented here, the *spray area* is determined using a value of 50 as the cutoff. The *fuel uniformity* is also calculated from the PLLIF images and is defined in Section 2.7.2. The level of *atomization* is presented in two forms, Sauter Mean Diameter (SMD) and drop size distribution.

The second section (Section 5.2) presents data for the variation in fuel tip positioning. In this case, PDI data and PLLIF images are presented for four different tip positions across the 0.125 in. air channel, described in Section

4.1. The atomization quality of each case was analyzed by examining the Sauter Mean Diameter (SMD) at each tip position. Data on the variation of the fuel tip geometry are described in Section 5.3. The three tip geometries presented in Figure 19 are compared using PDI data. The fourth section (Section 5.4) presents data on the variation of air hole size. Data acquired for two different hole sizes, 0.088 in. (2.24 mm) dia. and 0.125 in. (3.18 mm) dia., are provided. In Section 5.5, penetration data for varying crossflow velocities are presented.

5.1 - Baseline Injector Characterization

This section introduces results on a baseline injector configuration. The baseline configuration was adopted to simulate the discrete injectors selected by Shaffar (1993) in a rapid mixing, LDI concept designed for a practical application. As a result, the injector air hole size for this testing was 0.088 inch in diameter. The tip was recessed a distance of 0.0625 in. (1.59 mm) back from the inside of the injector panel wall. This corresponds to a position half-way across the 0.125 in. channel. The fuel hole size was also held constant at 0.0135 inch (0.343 mm) in diameter with an associated flow number of 3.11 lb/hr/(psig)$^{0.5}$ (Lefebvre, 1983). The mainstream air velocity for this testing was maintained at 124.7 ft/sec (38 m/sec).

The data are presented and analyzed in the following sections. Penetration, spray area, and atomization are examined in detail for a variety of injector flow conditions. Section 5.1.1 presents results on a variation in air-to-liquid ratio (ALR), while Section 5.1.2 provides information on pressure drop variations.

5.1.1 - Air-to-Liquid Variations

Penetration, spray area, and atomization are examined in detail for ALR's varying from 0 to 4.67. Figure 25 presents four processed PLLIF images and corresponding PDI data for variations in the air-to-liquid ratio (ALR). For the PLLIF images, the view is that of the mainstream air approaching the fuel injection hole, with the left, vertical axis representing the wind tunnel wall (i.e., injector panel). This top view presents the jet penetrating from the y-axis out into the crossflow of air in the x direction. A 10-level gray scale is employed to represent contours of fuel mass fraction from 0 to 1.0. A value of 0 (white in color) denotes a zero concentration of fuel and therefore can be considered pure mainstream flow. A value of 1.0 represents the highest concentration of liquid. For convenience, the highest fuel mass fraction (0.95 - 1.0) is depicted as black in Figure 25. These images have been overlaid onto PDI data taken in the plane of the injector hole. All images and PDI data presented are at a plane located 10 mm

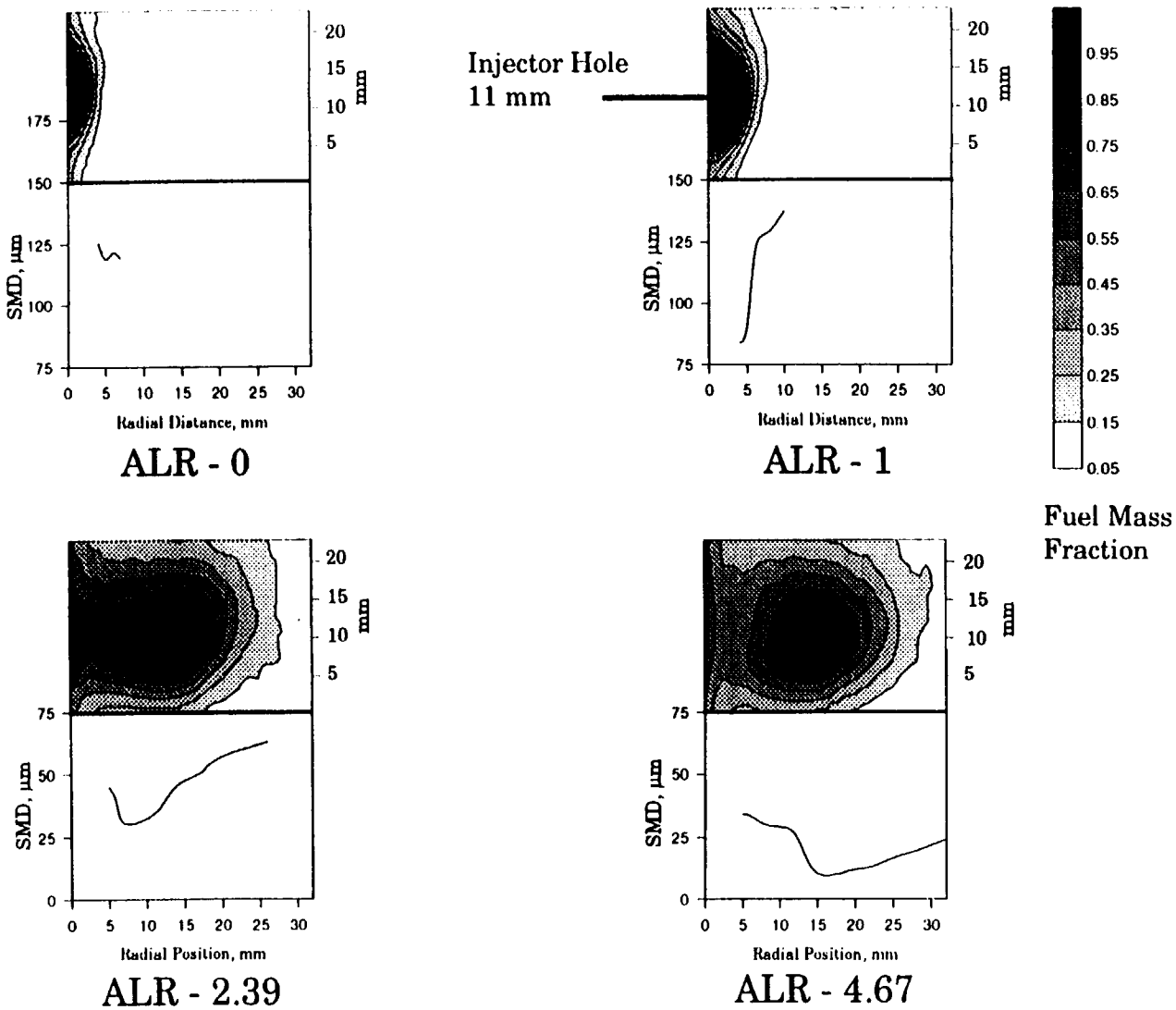

Figure 25: PLLIF images (top view) and PDI data for ALR variations, Z = -10 mm.

downstream of the injector hole. Due to clipping on the receiver, no PDI data could be acquired closer than 5 mm from the injector panel. Additionally, the radial distance outward was limited by the number of drops present. Occasionally the PDI data extends past what appears to be the edge of the PLLIF image. In these areas, some drops were present but not in sufficient number to be detected by the PLLIF system. Table 1 below presents flow information for the ALR conditions discussed in this section.

	Fuel Mass Flow	Fuel Velocity	Air Mass Flow	Air Velocity	Pentration	Spray Area
	g/sec	m/sec	g/sec	m/sec	mm	mm^2
ALR - 0	0.146	2.00	0.000	0.00	1.00	59.7
ALR - 0.947	0.146	2.00	0.139	36.20	2.00	98.9
ALR - 1.66	0.146	2.00	0.243	63.40	6.94	263.9
ALR - 2.39	0.146	2.00	0.349	91.20	11.30	317.9
ALR - 2.77	0.146	2.00	0.405	105.70	11.74	319.5
ALR - 3.14	0.146	2.00	0.459	119.71	12.04	372.8
ALR - 3.89	0.146	2.00	0.570	148.66	11.94	353.5
ALR - 4.67	0.146	2.00	0.684	178.50	11.80	340.5

Table 1 - ALR Flow Conditions

A substantial change in both penetration and dispersion can be observed as the air-to-liquid ratio is increased from 0 to 4.67. The mass flow of fuel was held constant for all ALR variations at 0.146 g/sec (3.22×10^{-4} lb/sec).

For the ALR - 0 case, no atomizing air is introduced. As seen in Figure 25, the fuel is only able to penetrate into the mainstream a distance of approximately 7 mm (0.276 in.). The majority of the fuel is confined to the boundary layer and, when running at this condition, fuel drips down the

tunnel wall. This condition yields poor dispersion and mixing of the fuel. The atomization of the liquid jet is also very poor at this condition. The SMD remains fairly constant at a value of approximately 120 microns for all radial locations. For the ALR - 0.947 case, not much improvement is attained. Although the small amount of atomizing air (0.139 g/sec) provides sufficient momentum to transport the fuel further into the crossflow, it is still not capable of distributing the fuel uniformly. The PDI data clearly demonstrate that the atomizing air propels the fuel outward. Smaller SMD drops are found very near the wall. The SMD then rises steeply when moving out directly under the fuel jet.

A significant improvement in dispersion and penetration is evidenced when operating at the ALR - 2.39 case. For this condition, the air flow is increased to 0.349 g/sec. The fuel penetrates out approximately 28 mm (1.1 in.) into the crossflow and is distributed more uniformly. A noticeable improvement in atomization is also observed at this condition. The maximum SMD detected is 60 microns, with the largest drops penetrating further into the crossflow. Only a slight improvement in penetration and spread is evidenced when increasing the air further to the ALR - 4.67 case (0.6838 g/sec air). The maximum concentration of the fuel is reduced one level down to the 0.75 - 0.85 band, but the penetration is essentially the same. The atomization for this condition is dramatically reduced. A

reasonably uniform SMD profile was attained, with most drops below 25 microns.

The leveling off in penetration experienced between ALR - 2.39 and ALR - 4.67 is more clearly seen in Figure 26. This plot presents penetration of the center of mass of the spray versus momentum flux ratio. The density term for the jet is calculated as:

$$\rho_{Jet} = \left(\dot{m}_{fuel}\rho_{fuel} + \dot{m}_{air}\rho_{air}\right)/\dot{m}_{total} \qquad (18)$$

Included on this plot is an empirical prediction of jet penetration based on data for air jet penetration through a combustor liner (Lefebvre, 1983). For the lower jet momentums, the equation underpredicts the jet penetration. This is a result of the increased momentum associated with the liquid. Because the equation uses air density rather than the density of methanol, underprediction in penetration is expected. The equation is also not capable of predicting the leveling off in penetration for higher jet momentums. An unknown amount of the atomizing air kinetic energy is consumed in stripping, atomizing, and mixing the liquid. The PDI data demonstrate this with the steadily decreasing SMD's as ALR is increased. Because the equation uses the *initial* jet momentum to predict penetration, it excludes additional energy sinks associated with the atomization and transport of the liquid. Therefore, pure air, or liquid (Reinecke, 1978) jet in crossflow predictions are not sufficient for describing the phenomenon seen here.

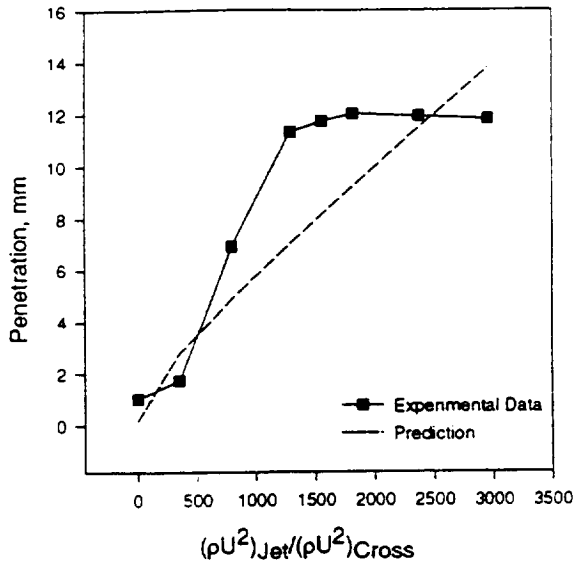

Figure 26: Penetration versus Air to Liquid Ratio.

A second parameter considered when describing the performance of an injector is the spray area. As seen in Figure 25, the spray "coverage" over the tunnel does not increase appreciably between the ALR - 2.39 and ALR - 4.67 cases. However, the spray area can be a deceiving parameter to examine when comparing the performance of the injector at various conditions. Therefore a quantitative measure of unmixedness is required to determine the injector's performance. A measure of unmixedness (U_S), based on the variance of the concentration distribution has been developed and is described in Section 2.7.2 (Liscinsky et. al., 1995). $U_s = 0$

corresponds to a perfectly mixed system, and U_s = 1 represents a perfectly unmixed system.

Figure 27 presents a comparison plot of spray area and the spatial unmixedness parameter versus momentum flux ratio. For higher jet momentum (i.e., increased ALR's) both the spray area and spatial unmixedness begin to level off. Although for this setup, the spray area and spatial unmixedness follow similar trends, both parameters must be examined to ensure a reasonable uniform mixture over any given area. For the present application, a completely uniform mixture over the largest possible area is desired. From the figure, the injector performs best where the spatial unmixedness is at a minimum (U_s = 0.129). This corresponds to an ALR of 3.89.

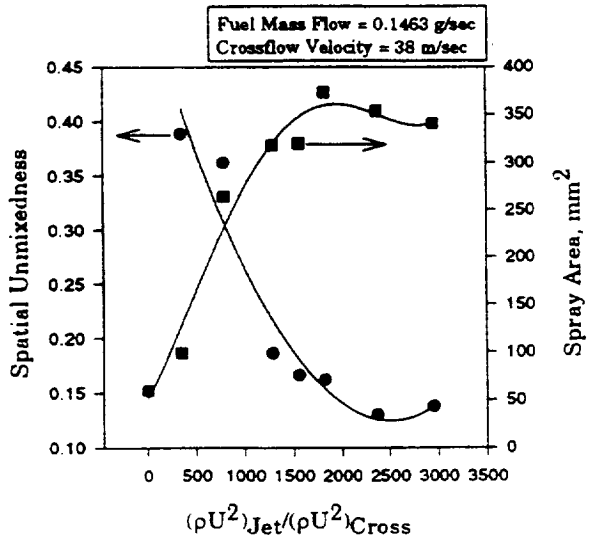

Figure 27: Comparison Plot of Spatial Unmixedness and Spray Area versus Air to Liquid Ratio.

5.1.2 - Pressure Drop Variations

Studies were also completed on the effect of fuel and air pressure drops on the penetration an dispersion performance of the injector. Data for fuel pressure drops of 5 psid and 30 psid and air pressure drops of 0 psid (0%) and 0.882 psid (6%) are described in the following section. The PLLIF images, overlaid on PDI data, are presented in Figure 28. All data shown in Figure 28 were taken at a distance 10 mm downstream of the injector hole. Table 2 presents the flow data for these pressure drop cases.

Fuel ΔP	Air ΔP	Fuel Mass Flow	Air Mass Flow	ALR	Fuel Velocity	Air Velocity	Penetration	Spray Area
psid	%	g/sec	g/sec		m/sec	m/sec	mm	mm^2
5	0	0.412	0.000	0.000	5.6	0.0	4.5	98
5	6	0.365	0.377	1.033	5.0	98.4	11.2	103
30	0	1.173	0.000	0.000	16.1	0.0	14.1	226
30	6	1.152	0.361	0.313	15.8	94.2	14.8	221

Table 2: Pressure Drop Flow Conditions

For the upper left image in Figure 28, the pressure drop across the fuel tube is 5 psid and no air is supplied to the injector. Comparing this image to the ALR - 0 case in Figure 25, several differences are apparent. The penetration and spread are much greater for the 5 psid case. This is a result of the higher pressure (5 psid vs. 0.5 psid), which results in a higher jet velocity. The SMD data for the 5 psid case also varies substantially from the ALR - 0 case. Smaller drops (75 microns) are found very

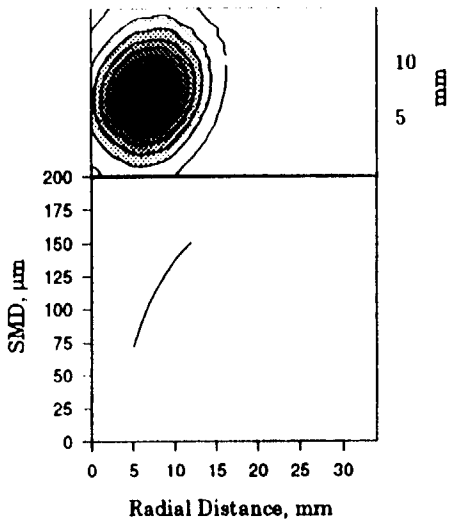

Fuel 5 psid, Air = 0%

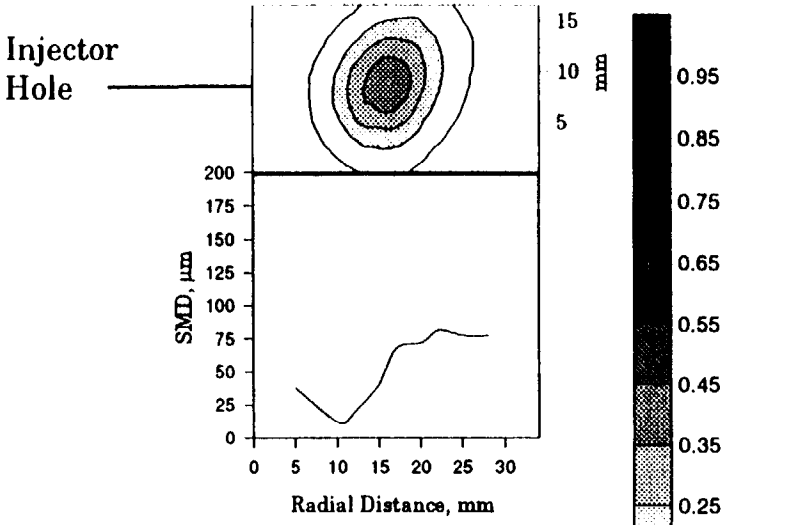

Fuel - 5 psid, Air - 6%

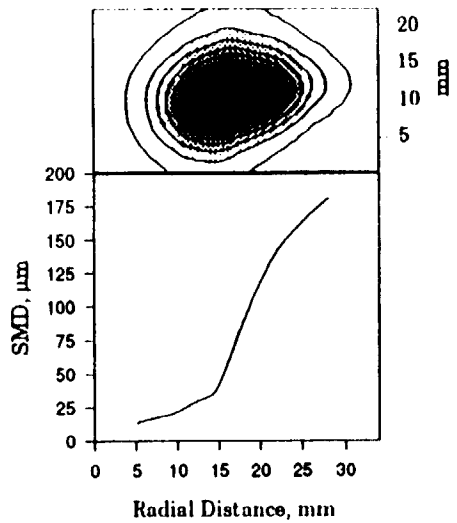

Fuel - 30 psid, Air - 0%

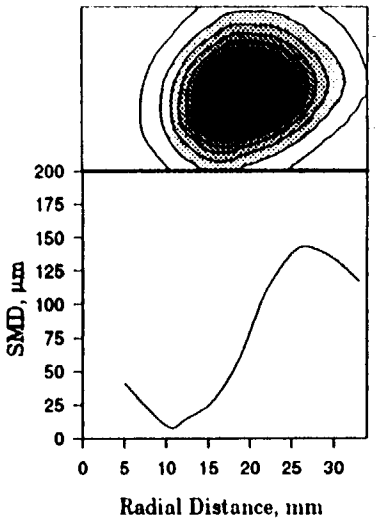

Fuel - 30 psid, Air - 6%

Figure 28: PLLIF images (top view) and PDI data for pressure drop variations, Z = -10 mm

near the wall and SMD increases sharply as proceeding out into the crossflow. These smaller drops are produced due to the increased relative velocity associated with the higher liquid jet velocity. This increased relative velocity effects better atomization and improves the spray area.

When a 6% air pressure drop is applied to the injector for the same fuel flow, the distribution and spread of the fuel is substantially enhanced. As seen in Figure 28, the highest mixture fraction is reduced to the 0.45-0.55 level. This demonstrates improved mixing of the fuel and air. The atomization of the liquid jet is also much improved for this case. Values for SMD now range from approximately 10 microns up to a maximum of 75 microns. The largest SMD drops are found at the same location as the center of mass from the PLLIF image.

For the 30 psid case, the penetration and area of the spray is increased further due to higher velocity, resulting from the greater pressure drop. The SMD data for this case rise from 15 microns at the wall up to 180 microns at the farthest spray measurement location. The PLLIF image associated with this condition seems to contradict the presence of small drops very near the wall. However this can be explained because the mass associated with the smaller drops near the wall is rather small. Therefore the PLLIF images do not reflect the presence of fuel in this area. In

actuality, small droplets are stripped off the liquid jet in the near-wall region and are forced down immediately by the crossflow air. The larger drops are found in the region from the center of mass out to the edge of the spray.

For the same fuel flow (30 psid), the 6% air pressure drop has little effect on the penetration and spray area. The penetration of the center of mass of the spray increases from 14.1 mm to 14.8 mm and the spray area remains virtually the same. Additionally, only a slight improvement in the atomization is realized. The maximum drop size observed for the 6% case is approximately 150 microns, while the maximum drop size with no air is approximately 175 microns. The injector air of the 6% case is providing some atomization of the liquid jet, evidenced by the smaller drop sizes at the edges of the spray. However the relative velocity (78.4 m/sec) is not capable of disrupting the liquid jet substantially. The air appears to be protecting the jet from the crossflow air, resulting in the slightly improved penetration.

Figure 29 presents penetration of the center of mass versus downstream distance for the four pressure drop conditions discussed above. The 5 psid case with no air was unable to penetrate more than 7 mm from the wall even at the lowest downstream distance. The overwhelming momentum of the mainstream air forced the fuel down immediately by the wall. The 6%

air drop provided much improved penetration, which continued to grow as the fuel moved downstream. The larger penetration of the 30 psid cases is shown to be due to the increased fuel velocity at these conditions. Also included in Figure 29 are the penetration predictions from Lefebvre (1983). The empirical constant in this equation was altered from 0.82 to provide a better fit. The modified equation was of the form:

$$Y = 1.2 D_{Jet} (\rho_{Fuel} U_{Jet}^2 / \rho_{air} U_{Cross}^2)^{0.5} (Z / D_{Jet})^{0.33} \qquad (19)$$

where Y = Penetration
D_{Jet} = Air Hole Diameter
U_{Jet} = Liquid Jet Velocity
U_{Cross} = Crossflow Velocity
Z = Downstream Distance

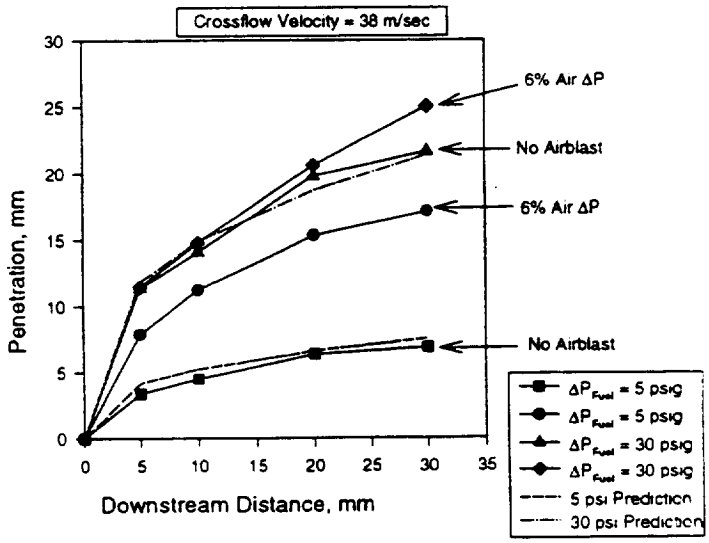

Figure 29: Penetration versus downstream distance for various pressure drop conditions

As seen in Figure 29, the equation is capable of predicting the penetration reasonably well for the pure liquid conditions, despite being derived to predict penetration of a pure air jet. Attempts were made to apply this equation to the 6% air pressure drop cases. However, non-uniform *initial* density and jet velocity for the fuel/air mixture precluded reasonable predictions. This illustrates the need to determine how much of the air's kinetic energy is consumed in atomization and how much serves to transport the droplets into the crossflow.

The explanation for the reduced effect of the 6% air pressure drop for the 30 psid fuel injection case is associated with atomization. Although the relative velocity between fuel and air is fairly large, the small amount of injector air relative to fuel (0.31 by mass) is unable to greatly assist in the atomizing process. This is evidenced again when comparing the pressure drop images to the ALR images in Figure 25. All the images for the pressure drop cases are elliptical in shape and disconnected from the wall. For the higher ALR cases, the distribution of fuel is continuous from the wall out to the center of mass of the spray. This is due to improved atomization for the high ALR cases, which produced very small drops. These smaller drops become entrained by the crossflow air and are, as a result, confined to the boundary region near the wall. Additionally, the high ALR conditions distribute the fuel more uniformly, which allows the CCD

camera to resolve the smaller droplets. For the pressure drop cases, drops are present even at the wall, but the concentration of mass in one area effectively forces the camera to be "blind" to the smaller droplets, due to dynamic range limitations. PDI measurements, presented in Figure 30, identify the relative trajectory of drops as a function of size and show that only drops less than 30 microns in diameter are entrained into the near wall region. Figure 30 presents a trajectory plot for two drop size classes, 1-10 micron and 41-50 micron drops. The data rate, in counts/sec, is also overlaid on these plots. The data presented in this figure is from the ALR - 2.39 case. This injector condition was capable of atomizing the liquid jet into drops in the size range of 1-10 microns. However, at this condition, the airblast was not as great as to prevent the presence of larger drops (70-90 microns). Therefore this case was selected to examine the trajectory of various drop sizes into the crossflow region.

The 1-10 micron drops are immediately forced down at the injector panel wall by the crossflow air. As seen in the figure, no drops of this size range are capable of penetrating further than approximately 8 mm (0.315 in.) from the injector wall. In the near wall region (<6 mm, <0.236 in.), the smallest droplets are moving almost directly downward.

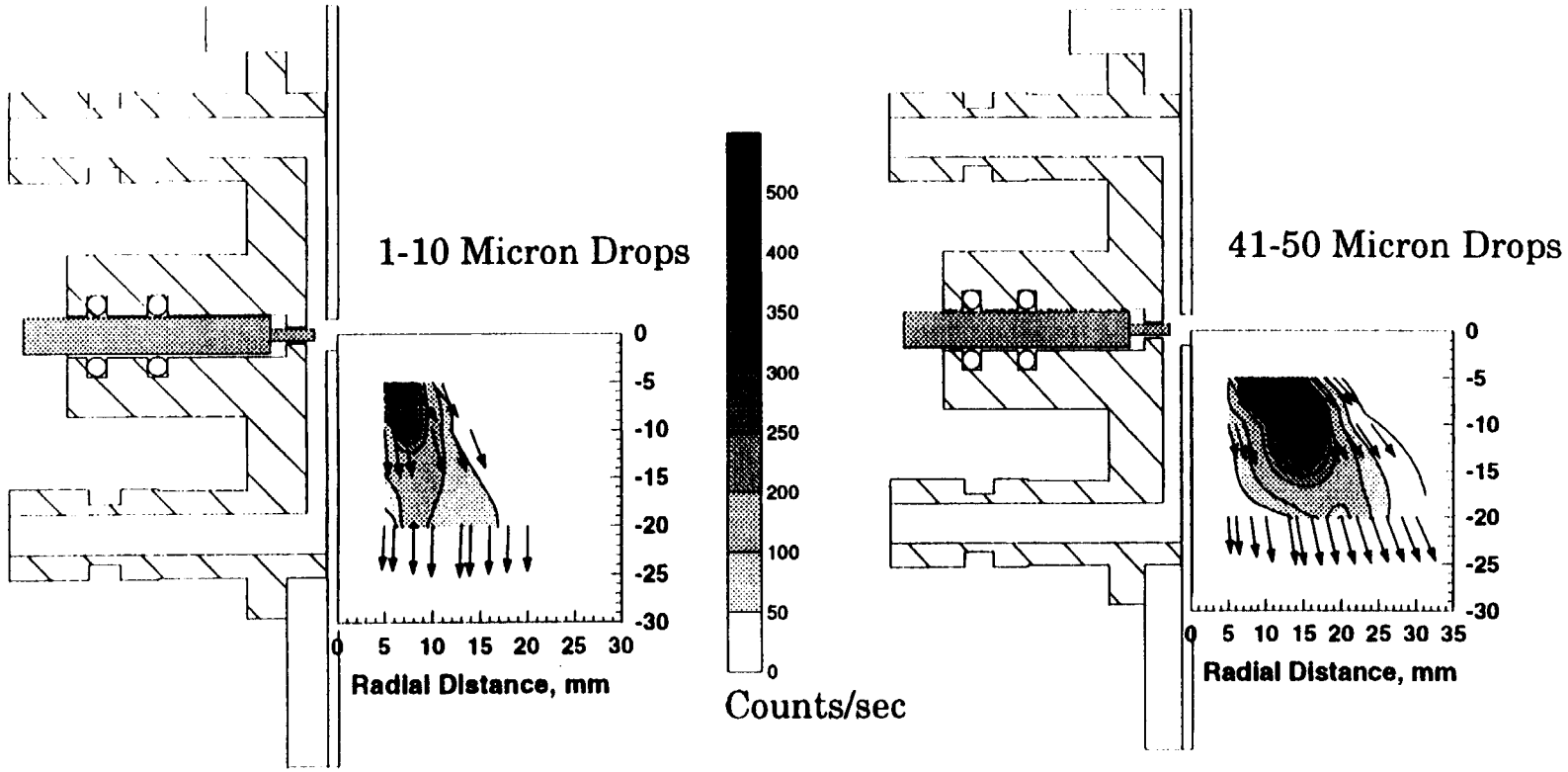

Figure 30: Trajectory Plots for ALR 2.39 injector flow condition.

The 41-50 micron drops are centralized at a radial distance of 8-20 mm (0.315 in. - 0.787 in) from the wall. Additionally, the trajectory of these drops is much less vertical and appears to be dominated by the injector air. Although data for larger drop sizes are not presented here, a similar trend to that demonstrated by the 41-50 micron drops is observed.

5.1.3 - Baseline Injector Summary

The results of the baseline injector characterization yield the following conclusions:

- An experiment has been successfully designed and demonstrated that addresses the mechanics of atomization and dispersion of a liquid jet injected radially into a high velocity cross-stream.
- Momentum-flux ratio is an important parameter in describing spray *penetration*.
  - Since a portion of the atomizing air kinetic energy is consumed in stripping and atomizing the liquid jet, pure air or liquid jet in crossflow predictions are not capable of describing the trends seen in the airblast injector.
  - However, an equation based on air jet penetration data was found to reasonably predict penetration of pure liquid jet cases.

- The cross-sectional *spray area* can, in some cases, be used to determine the performance of an injector. An index of mixing (i.e. *fuel uniformity*) within this area is also useful. The use of PLLIF permits mixing to be assessed.
- *Atomization* is a key factor affecting the spray *penetration* and *area*.
  - For higher ALR's, small droplets are formed which become entrained in the crossflow air and are forced down immediately by the wall.
  - For lower ALR's, the small drops are fewer in number and an elliptical spray pattern is developed which penetrates into the crossflow air.

5.2 - Tip Position Variations

Figure 31 presents a schematic of the injector hardware with the fuel injection location described by X. The goal of varying this parameter is to determine if an injection location exists where atomization, spray area, and penetration is optimized. The four injection points tested are also included in the figure. The 0.016 in. (0.406 mm) tip position is close to the air exit hole and results in high blockage of the air hole. The 0.031 in. (0.787 mm) position lies halfway between the midpoint of the channel and the injector wall. The 0.063 in. (1.6 mm) tip position is centered exactly at the midpoint

of the injector air channel. The 0.125 in. (3.175 mm) position is flush with the back wall of the air passage. Both PDI and PLLIF data are utilized to determine the penetration, spray area, and atomization at each injection location.

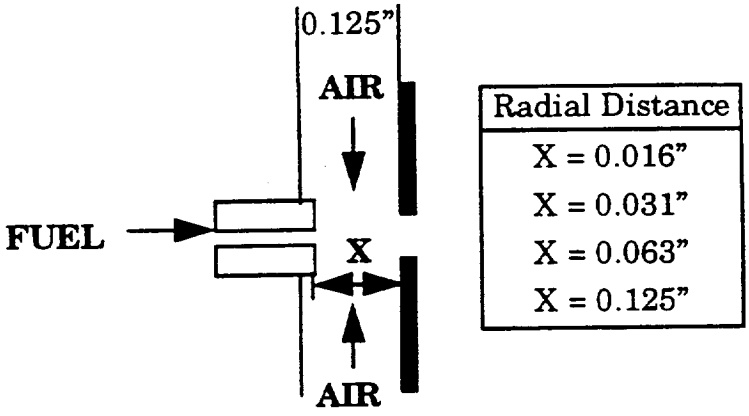

Figure 31: Fuel Tip Positions

For all testing of the fuel tip placement, the crossflow velocity is held constant at a speed of 38 m/sec. Two injector flow conditions are utilized to determine the effect of tip position: ΔP_{Fuel} = 5 psid - ΔP_{Air} = 3%; ΔP_{Fuel} = 5 psid - ΔP_{Air} = 6%. The specific flow information for each tip is presented in Table 3. The fuel velocity presented is the initial velocity of the liquid jets as it emerges from the fuel hole. The air velocity listed is an approximation for the air velocity at the exit hole, calculated by subtracting the fuel hole area from the air hole area.

Tip Position	ΔP_{fuel}	ΔP_{air}	Fuel Mass Flow	Air Mass Flow	Fuel Velocity	Air Velocity	AC_d
in	psid	%	g/sec	g/sec	m/sec	m/sec	in^2
0.016	5	3	0.412	0.201	5.6	52.5	0.0047
0.016	5	6	0.412	0.280	5.6	73.1	0.0047
0.031	5	3	0.412	0.252	5.6	65.7	0.0057
0.031	5	6	0.400	0.318	5.5	83.1	0.0057
0.063	5	3	0.400	0.282	5.5	73.6	0.0060
0.063	5	6	0.400	0.371	5.5	96.9	0.0060
0.125	5	3	0.412	0.282	5.6	73.1	0.0063
0.125	5	6	0.412	0.371	5.6	96.4	0.0063

Table 3: Tip position variation flow conditions.

The blockage of the air passage for the 0.016 in. case is evidenced by the lower air mass flow rates for similar pressure drops. The AC_d for this case is also the lowest. The AC_d values continue to rise as the injector tip is pulled back away from the injector panel wall. However, the air flow rates for the 0.0625 in. and 0.125 in. cases are exactly the same. The tip is far enough removed at the 0.0625 in. position to not affect the flow of air out the injector hole.

It is clear that air flowing within the injector panel is accelerating as it approaches the injector hole. Because the relative velocity between the liquid and air has been proven to be a dominate parameter in atomization, the tip position which injects the fuel into the highest velocity region should provide superior atomization. For the 3% air pressure drop case, air is flowing through the injector channel at 3.22 m/sec (10.6 ft/sec) and accelerates to a velocity from 52 to 73 m/sec (170.6 to 239.5 ft/sec) depending

on the tip position. For the 6% pressure drop, the velocity in the channel is 4.47 m/sec (14.7 ft/sec).

The highest velocities are achieved within the injector air hole itself. Therefore the fuel tip which injects the fuel as close to this region as possible should outperform other positions. As is the case with most systems though, a compromise between tip position and air flow must be achieved. Less air is provided to the injector for tip positions close to the air hole. The optimum tip position is analyzed in the following paragraphs, utilizing PDI and PLLIF.

The characterization of the fuel injection location is first evaluated using PDI. Figure 32 presents a plot of radial distance versus SMD for the 3% air pressure drop case. Data for all four tip positions are displayed on this graph. The atomization quality of each position is rather similar. The curves are separated at most by approximately 25 microns. This demonstrates that the positioning of the fuel tip does not have much effect on the atomization quality of the injector. However, one tip position does demonstrate slightly better atomization than any other tip. This tip position is 0.0625 in. back from the injector wall. Previous research has shown that PDI results are very dependant on user-controlled settings (McDonell and Samuelsen, 1990). Therefore, settings utilized for this study

are optimized and held constant for all comparison plots. A discussion of the user controlled settings and the accuracy of the data is presented in Appendix E. Due to the care taken in selecting user-controlled settings, the seemingly small variations in the plot below are real.

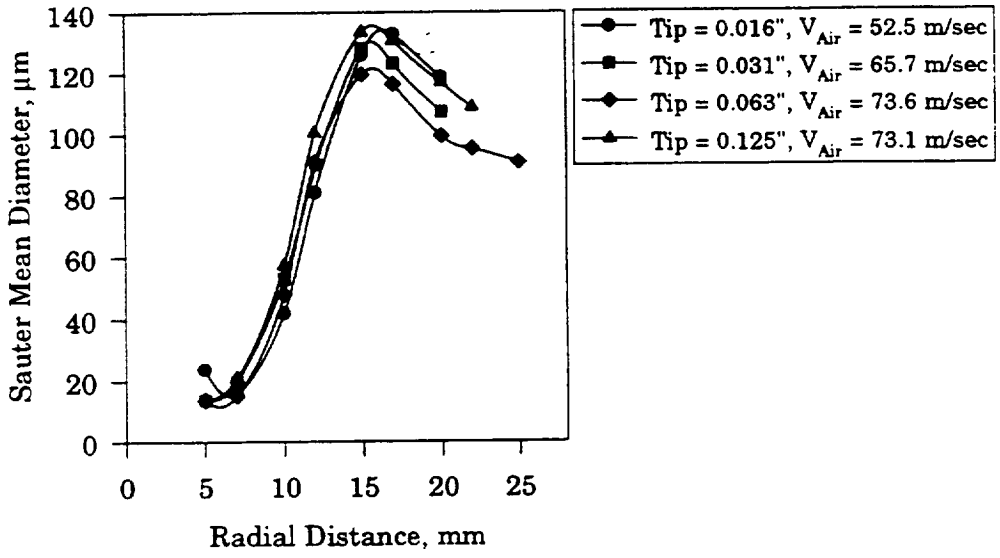

Figure 32: Tip position variation for 3% air pressure drop case (Z = -10 mm).

Figure 33 displays a second plot of SMD for each tip position. Data for the 6% air pressure drop are presented here. Again the performance of each position is rather similar. However the 0.0625 in. position again slightly outperforms the other locations. This improvement in atomization can be attributed to two factors. First, the 0.0625 in. position is far enough removed to prevent blockage of the air hole. As a result more air is provided

to the injector for any given pressure drop. This creates higher air velocities at the exit hole and within the injector. Secondly the tip is positioned close enough to the hole to supply the fuel to a region of high velocity. To effect atomization the low velocity fuel must be injected into a region of high velocity air such that the air provides a stripping force. For the 0.125 in. tip position, similar air velocities are achieved, but the fuel is injected into a region of lower velocity. As the fuel approaches the exit hole, it is accelerating along with the air. This results in a lower stripping force.

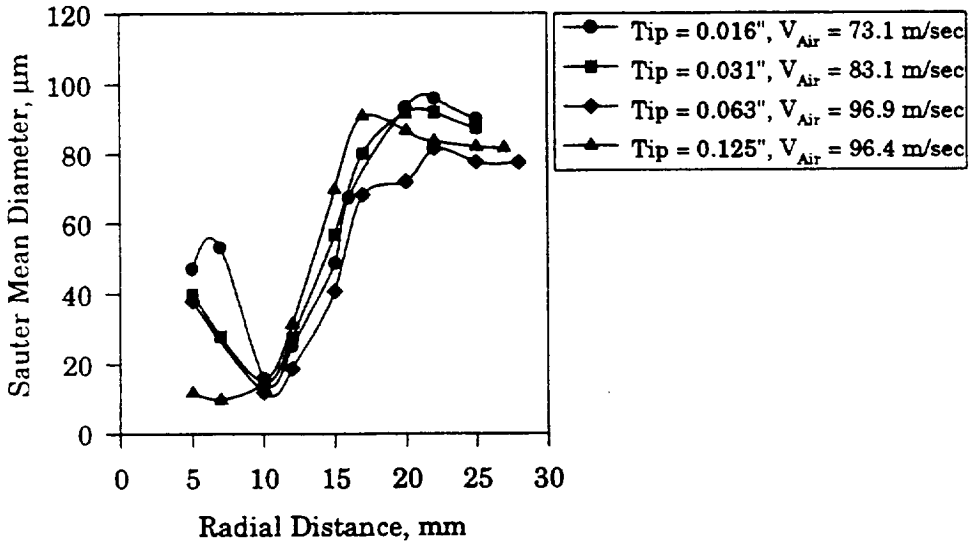

Figure 33: Tip position variations for the 6% air pressure drop condition (z = -10 mm).

To determine the actual performance of the injector, the SMD value alone is not sufficient. Figure 34 presents a plot of the drop size distribution for

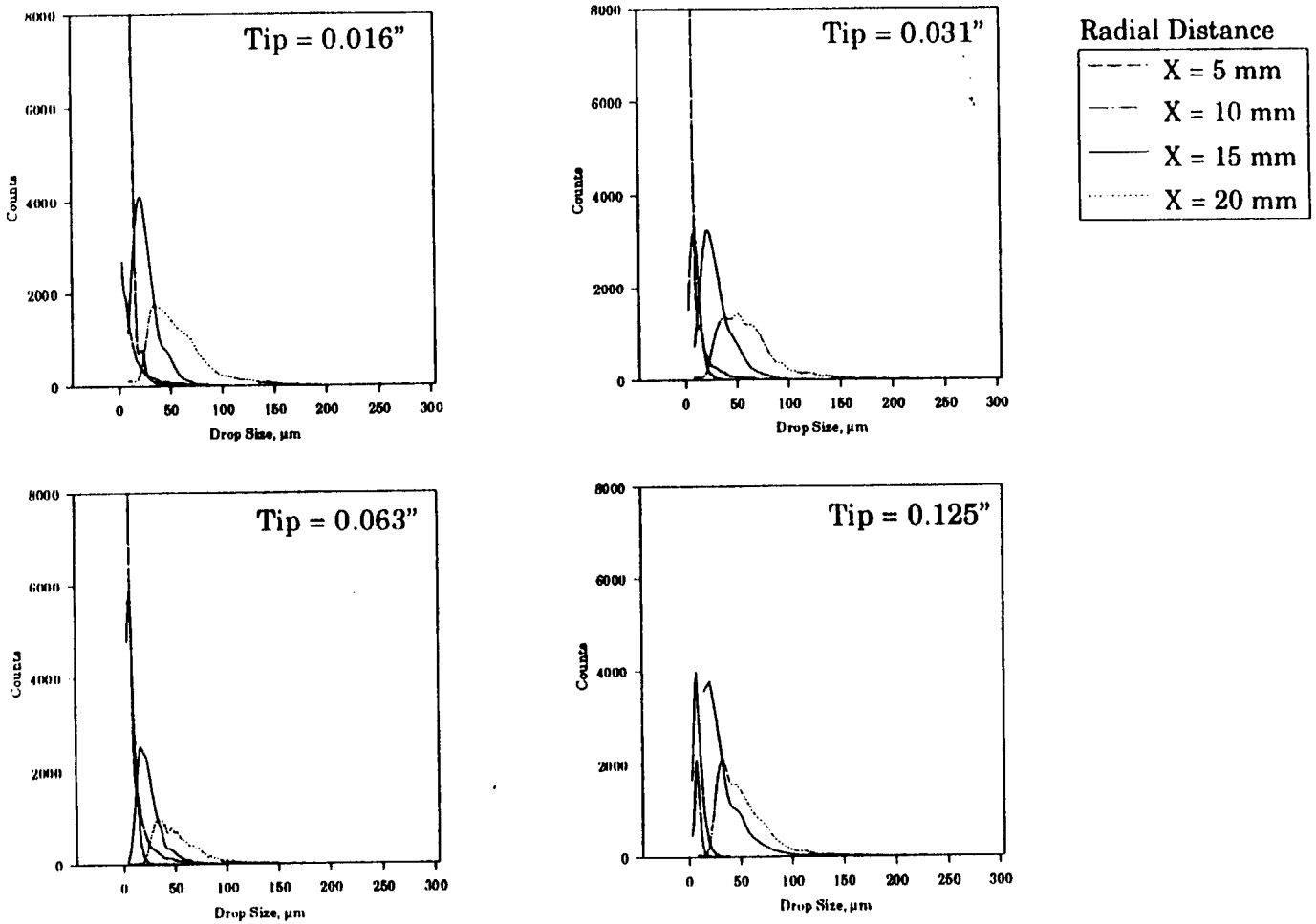

Figure 34: Drop size distributions for the 6% air pressure drop condition, Z = -10 mm.

each tip position for the 6% air pressure drop condition. For these plots, the x-axis represents the drop size, while the y-axis provides the number of counts at a given size. Four radial distances are displayed on each plot, 5, 10, 15, 20 mm. For the X = 5, 10 mm locations, the majority of drops are less than 50 microns in size for every tip position. Moving away from the injector wall, the distributions begin to vary between tip positions. The 0.0625 in. tip position again seems to be superior. The distributions for this case are for the most part below 100 microns, with absolutely no drops greater than 150 microns. For the other tip positions, the drop distribution curves are shifted further to the right. For the 0.016 in. and 0.031 in. tip locations, a small number of drops are present in the 200 micron range.

PLLIF images were also acquired for each tip position at a variety of injector flow conditions. Figure 35 presents four images for each tip position for the 6% air pressure drop condition. The contour plots shown can be considered fuel mass fraction plots, with white representing pure crossflow air. The four images are very similar in shape, which demonstrates that the fuel tip position does not greatly affect the penetration and spray area of the injector. For the 0.031 in. tip position, a continuous dispersion of fuel, from the injector wall out to the center of mass, is evidenced. This can be explained by the larger drops present at the wall for this case. These large drops contain enough mass for the PLLIF system to resolve them. For the

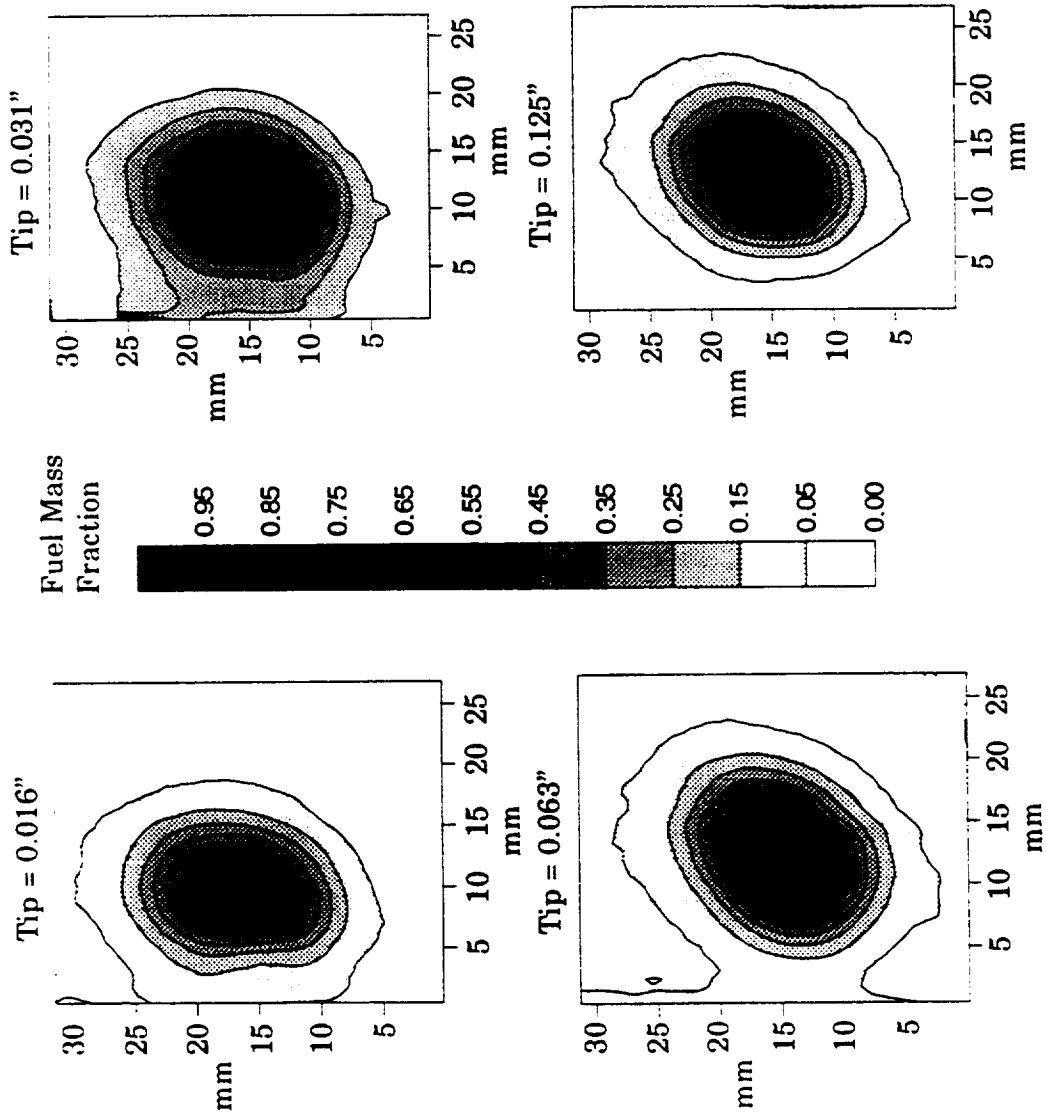

Figure 35: PLLIF images for the 6% air pressure drop condition, Z = -10 mm.

0.0625 in. and 0.125 in. positions, small drops are present but are not picked up by the PLLIF system. Overall, the tip position does not have a substantial effect on the performance of the injector.

5.2.1 - Tip Positioning Summary

The results of the tip position parametric study yield the following conclusions:

- Tips positions close to the air exit hole produce higher ACd's an result in less air provided to the injector for any given pressure drop.
- *Penetration* of the center of mass remains constant for all four tip positions.
- *Spray area* is relatively unchanged for all tip positions. *Fuel uniformity* is slightly improved for the closest three tip positions.
- The 0.0625 in. tip position demonstrates slightly improved *atomization* performance over the other tip positions.
    - The 0.0625 in. tip position is recessed far enough to prevent blockage of the exit air hole. This yields higher air flows and air velocities.

5.3 - Fuel Tip Geometry Variations

Fuel tip geometry is also identified as a parameter which could affect the performance of the injector. Three tip geometries are employed in the current work and are presented in Figure 19. The fuel tip which simulates the LDI injector (Shaffar, 1993) is displayed as Figure 19a. The second injector (Figure 19b) is designed to allow air closer to the fuel injection hole. The fuel tip angle is 45 degrees and provides a more aerodynamic design. This tip is also selected due to its similarity to previous work (Nukiyama and Tanasawa, 1939). The third fuel tip employed (Figure 19c) is the most aerodynamic of the three designs. This tip is essentially a hypodermic needle which extends into the injector air channel. The needle results in very little blockage (i.e. larger effective area) and therefore allows larger air mass flow rates, compared to the other tips, for similar pressure drops. The following sections present SMD data for three flow conditions: 5 psid fuel pressure drop with 0, 3, and 6 percent air pressure drops for the three tip geometries. In the final section, a comparison of the three tips is presented.

5.3.1 - LDI Geometry

The injector setup for this testing consists of the 0.088 in. diameter air hole and the LDI tip geometry recessed 0.0625 in. from the back of the injector

panel. The AC_d for this setup was measured experimentally and found to be 0.006 in^2. The settings for the three flow conditions tested are presented in Table 4. Looking at the table, it is apparent that the air setting has a direct effect on the fuel setting. As the pressure drop on the air circuit is increased, less fuel is required to achieve the desired 5 psi drop across the fuel circuit. This was observed for all fuel tips.

Fuel ΔP	Air ΔP	Air ΔP	Fuel Mass Flow	Air Mass Flow	ALR	Fuel Velocity	Air Velocity
psid	psid	%	g/sec	g/sec		m/sec	m/sec
5	0.000	0	0.44	0.000	0.00	5.9	0.0
5	0.441	3	0.40	0.282	0.71	5.5	73.6
5	0.882	6	0.38	0.371	0.98	5.2	96.9

Table 4: LDI fuel tip flow conditions

The atomization of the LDI fuel tip was measured using PDI. Figure 36 displays SMD data for the three flow conditions previously described. For the ALR - 0 case, a discrete fuel jet penetrates out a small distance into the crossflow air. This is demonstrated by the gradual increase in SMD with increasing radial distance. Drops are stripped off the fuel jet and pulled immediately down by the wall. These drops tend to be smaller in diameter than the drops within the main fuel jet. As the atomizing air is increased to the ALR - 0.71 case, the SMD falls off slightly. The maximum drop sized observed at this condition is approximately 120 microns. The penetration and atomization is further improved when increasing the air to the ALR - 0.98 condition. The maximum drop size obtained here is approximately 80

microns. However, the maximum penetration of the spray increases only 2mm.

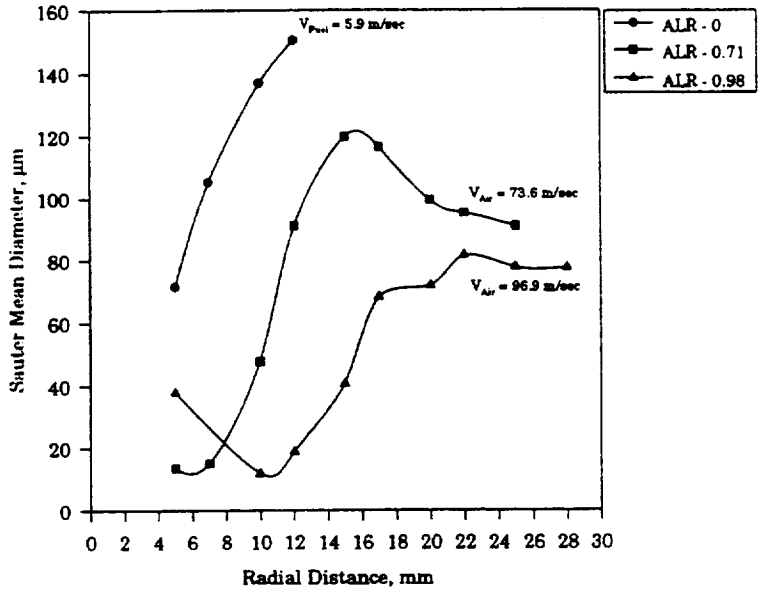

Figure 36: LDI fuel tip SMD profiles (ΔP_{Fuel} = 5 psid, ΔP_{Air} = 0, 3, and 6%).

5.3.2 - Angled Tip Geometry

As discussed previously, the angled tip is utilized to provide a more aerodynamic design which allows air to encounter the fuel jet at a different angle. The hole size utilized for this test is also 0.088 in. in diameter with an AC_d of 0.006 in^2. The fuel tip is recessed 0.0625 in. from the back of the injector panel. Table 5 provides flow data for the three conditions tested. The flow conditions for the angled tip geometry are very similar to the

specifications for the LDI tip. Therefore the angled geometry has not affected the flow pattern within the injector dramatically. The only difference is a very slight increase in the amount of fuel delivered to the injector.

Fuel ΔP	Air ΔP	Air ΔP	Fuel Mass Flow	Air Mass Flow	ALR	Fuel Velocity	Air Velocity
psid	psid	%	g/sec	g/sec		m/sec	m/sec
5	0.000	0	0.44	0.000	0.00	5.9	0.0
5	0.441	3	0.42	0.282	0.66	5.8	73.6
5	0.882	6	0.42	0.371	0.88	5.8	96.9

Table 5: Angled fuel tip flow conditions

Figure 37 displays the PDI data taken for the three flow conditions utilizing the angled fuel tip geometry. This plot is very similar to Figure 36 above. The maximum drop sizes and drop size trends for the 0, 3, and 6% air pressure drops are almost exactly those seen with the LDI fuel tip. This demonstrates that the angled tip does not affect the performance of the injector.

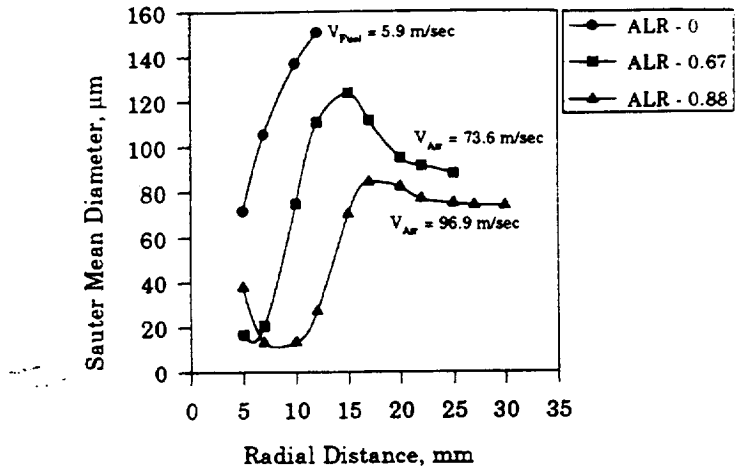

Figure 37: Angled fuel tip SMD profiles
(ΔP_{Fuel} = 5 psid, ΔP_{Air} = 0, 3, and 6%).

5.3.3 - Hypodermic Needle Tip Geometry

The hypodermic needle geometry provides minimum blockage of the injector air hole. The air hole size utilized for this test is 0.088 in. (2.24 mm) in diameter with a AC_d of 0.006 in^2 ($3.87x10^{-2}$ cm^2). The fuel tip is recessed 0.019 in. (0.483 mm) from the back of the injector panel wall. The fuel hole for this geometry is larger than the previous two cases, 0.023 in. (0.584 mm) dia. versus 0.0135 in. (0.343 mm) dia. Previous research has shown that the effect of fuel orifice size is relatively insignificant for geometries similar to the current setup (Lorenzetto and Lefebvre, 1977). Therefore any change in injector performance can be reasonably attributed to the shape of the fuel

injector tip. Table 6 below presents flow information for the needle geometry. Although the AC_d of the injector hole is similar to previous geometries, it is clear from the table that a larger portion of air is supplied for similar pressure drops. This results in greater air velocities through the injector hole and should improve the atomization for this case.

Fuel ΔP	Air ΔP	Air ΔP	Fuel Mass Flow	Air Mass Flow	ALR	Fuel Velocity	Air Velocity
psid	psid	%	g/sec	g/sec		m/sec	m/sec
5	0.000	0	0.45	0.000	0.00	2.10	0.0
5	0.441	3	0.39	0.297	0.76	1.83	81.3
5	0.882	6	0.40	0.383	0.96	1.89	104.8

Table 6: Hypodermic needle flow conditions.

Figure 38 displays a plot of Sauter Mean Diameter versus radial distance for the three flow conditions described above. For the ALR - 0 condition, the SMD actually decreases from 155 to approximately 120 as radial distance is increased. This trend is exactly opposite of that seen for the previous two cases and can only be attributed to changes in the fuel hole size. Also, the atomization for the 3% and 6% air pressure drop cases is slightly improved when compared to the previous cases. This is most likely attributed to the increase in relative velocity between the fuel and air for this geometry. Therefore one major benefit of the needle geometry is the increased amounts of air that can be supplied for similar pressure drops.

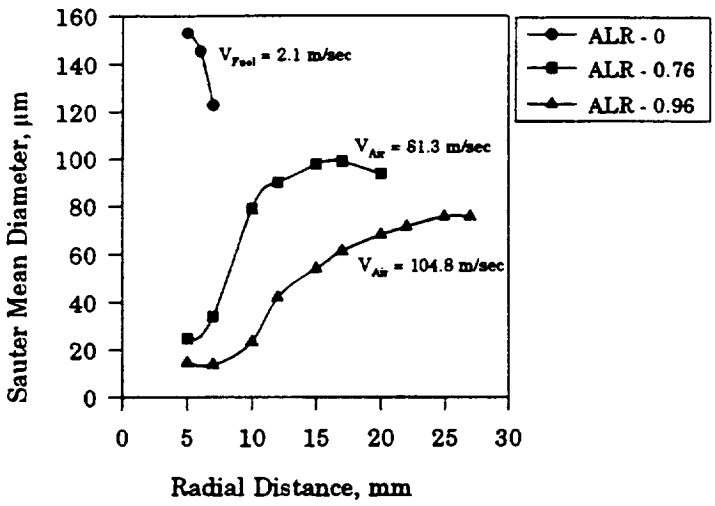

Figure 38: Hypodermic needle SMD profiles.
(ΔP_{Fuel} = 5 psid, ΔP_{Air} = 0, 3, and 6%).

5.3.4 - Geometry Comparison

Figure 39 presents a comparison plot for the 5 psid fuel pressure drop and the 6% air pressure drop case. Included on this plot are data for the LDI geometry, the angled tip geometry, and the needle geometry. The needle geometry provides slightly better atomization for this given flow condition, due to the increased relative velocity associated with this fuel tip. To prove this effect, another condition was run, providing the same air flow to the needle geometry as was applied to the angled and LDI geometries. This case is displayed as Needle 2 data in the figure. The SMD profile for this

condition is slightly higher than Needle 1 data and closely mimics the LDI data. Therefore, relative velocity is the most likely reason for the slightly improved atomization for the needle tip. However, overall the atomization does not vary considerably. This demonstrates that tip geometry is not an important factor in determining the atomization performance of the injector.

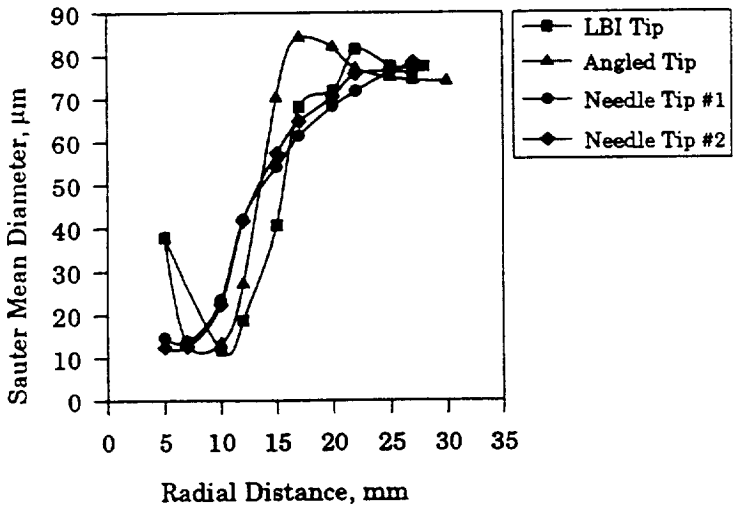

Figure 39: Fuel tip geometry comparison.

5.3.5 - Tip Geometry Summary

The results of the tip geometry parametric study yield the following conclusions:

- Tip geometries which minimize blockage of the exit air hole allow higher relative velocities for any given pressure drop.

- No PLLIF images are available to determine *penetration* of the center of mass of the spray. However the maximum penetration of the spray can be determined using PDI data. All fuel tip geometries penetrated approximately the same distance for the 6% air pressure drop condition.
- *Spray area* calculations and *fuel uniformity* are not presented due to the lack of PLLIF images for these conditions.
- Fuel tip geometry does not have a substantial effect on the *atomization* performance of the injector.

5.4 - Hole Size Variation

The following section presents results from a study on the variation in injector air hole size. Two hole sizes were employed for the current work. The first hole size is 0.088 inch in diameter with an AC_d of 0.006 in^2 ($3.87x10^{-2}$ cm^2). The second hole size is 0.125 inch in diameter with an AC_d of 0.009 in^2 (0.0581 cm^2). Three injector flow conditions were selected to compare these two hole sizes. These conditions are ALR - 2.39, ALR - 4.67, and ΔP_{Fuel} = 5 psid, ΔP_{Air} = 0.88 psid. The associated flow information for these conditions is presented in Table 7.

Air Hole Size	Fuel DP	Air DP	Fuel Mass Flow	Air Mass Flow	ALR	Fuel Velocity	Air Velocity
in	psid	psid	g/sec	g/sec		m/sec	m/sec
0.088	0.75	0.700	0.146	0.349	2.39	2.00	91.2
0.088	2.50	2.960	0.146	0.684	4.67	2.00	178.5
0.088	5.00	0.880	0.400	0.371	0.98	5.16	96.9
0.125	0.10	0.250	0.146	0.349	2.39	2.00	44.7
0.125	0.50	0.883	0.146	0.647	4.62	2.00	82.7
0.125	5.00	0.880	0.423	0.617	1.47	5.79	78.8

Table 7: Hole size variation flow conditions.

Obviously, the 0.125 in. hole size delivers more air than the 0.088 in. hole for the same pressure drop. However the air velocity is generally lower for the larger hole size. This is illustrated in Table 7. For a 0.88 psi drop on the air circuit, the 0.125 in. hole yields an ALR of 1.47 with an air velocity of 78.8 m/sec (258.5 ft/sec). For the same 0.88 psi drop, the 0.088 in. hole results in an ALR of 0.98 with an air velocity of 96.9 m/sec (317.9 ft/sec). To determine if one hole size is better than another, PDI is utilized to measure the quality of atomization for each condition with each hole size. Figure 40 presents a plot of SMD versus radial distance for the ALR - 2.39 and 4.67 conditions. The 0.088 in. hole renders much lower drop sizes for both ALR conditions. This is due to the much higher air velocity associated with this hole size, which results in a high pressure drop on the air circuit. For the ALR - 2.39 case, the pressure drop is still within a reasonable range, 4.8%. However, for the ALR - 4.67 condition, the pressure drop on the air circuit is 20.1%. This value is well outside the range typically encountered for airblast-type injectors. The 0.125 in. hole sizes allows operation at the ALR - 4.67 case while still keeping the pressure drop reasonable (6%). Therefore,

the 0.125 in. hole size, operating at an ALR of 4.67 provides the best atomization for any reasonable flow condition.

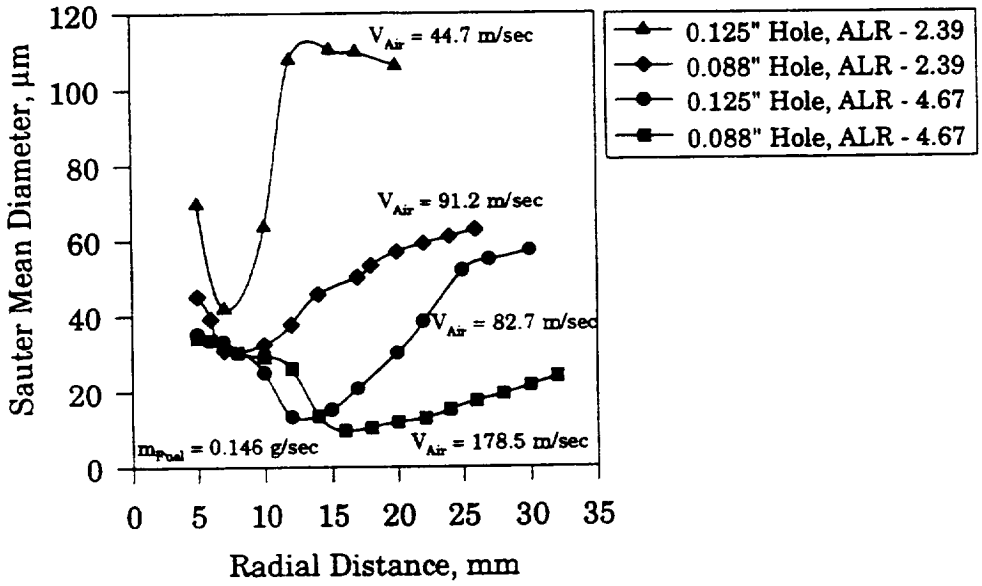

Figure 40: ALR variations for the 0.088 in. and 0.125 in. hole sizes.

A compromise between air velocity and air mass flow rate is presented here. To determine if one parameter is superior to the other, similar fuel flow rates and air circuit pressure drops are supplied to each hole size. The condition selected is that of a 5 psid fuel pressure drop and a 6% air pressure drop. A fuel flow rate of approximately 0.40 g/sec is provided for each hole size. The differences in air flow rate for each hole is described above in Table 7. Figure 41 displays a plot of SMD versus radial distance

for these two conditions. The SMD profiles remain fairly consistent in the near-wall region of the spray. However, when moving toward the center of mass of the spray, the SMD profile for the 0.088 in. hole size begins to level off before the 0.125 profile. This is due to the higher air velocity associated with the 0.088 in. hole and demonstrates that relative velocity plays a stronger role in the atomization process than ALR.

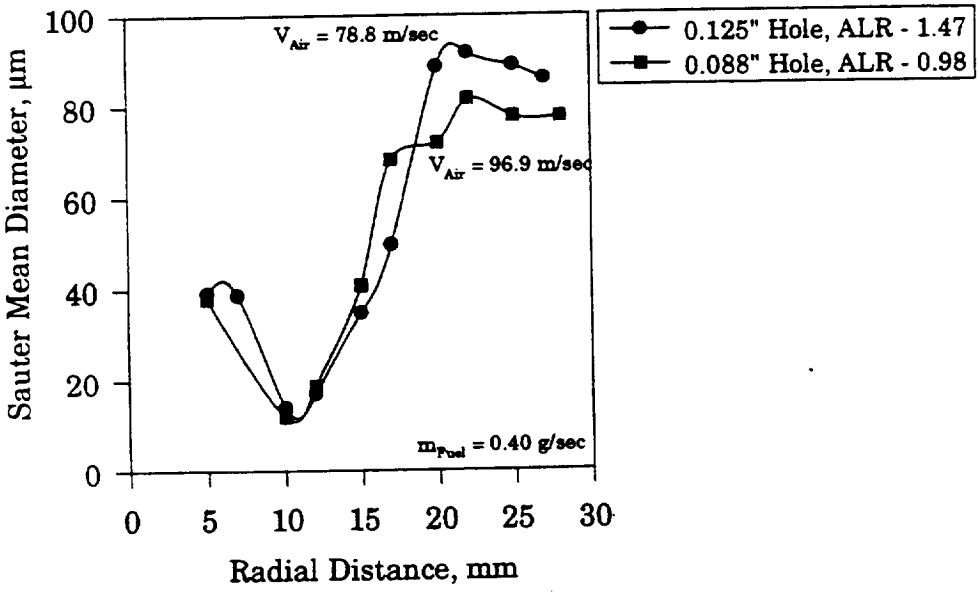

Figure 41: 0.088 in. and 0.125 in. hole size comparison.

5.4.1 - Hole Size Variation Summary

The results of the hole size variation yields the following conclusions:

- Maximum *penetration* of the spray increases with air velocity for both air hole sizes. Lack of PLLIF images prevents presentation of information of the penetration of the center of mass.
- No information on *spray area* or *fuel uniformity* is available.
- Relative velocity plays a more dominant role in the *atomization* process than ALR for the flow conditions and geometries examined.
    - Smaller SMD's are obtained for conditions with lower ALR's but higher relative velocities.

5.5 - Crossflow Velocity Variations

The penetration of the fuel jet into the crossflow air is a crucial parameter to the performance of the injector being studied. When operating, underpenetration of the liquid jet results in a core of hot products surrounded by cool unburned air. Overpenetration of the spray results in coating of the combustor walls and can lead to difficulties in light-up and problems with emissions. Therefore optimum placement of the fuel spray across the combustor chamber is crucial to the success of the injector. To gain information on this topic, the reduced cross-sectional area hardware, described in Chapter 4, is utilized. For this setup, the distance from the injector wall to the opposing wall is 0.712 in (18 mm). This corresponds to the distance from the injector to the quarl section wall in the LDI combustor

developed by Shaffar (1993). This hardware allows the optimum penetration to be readily identified.

The momentum flux ratio, $(\rho U^2)_{Jet}/(\rho U^2)_{Mainstream}$, is identified as a critical parameter in describing the penetration of liquid jets or air jets in a crossflow (Holdeman, 1993; Nguyen and Karagozian, 1992; Lefebvre, 1983). In the previous four sections, flow conditions of the nozzle are varied while the crossflow air is held constant. This provides a series of momentum flux ratios which could supply information on the penetration quality of the injector. In Section 5.1, the penetration was found to level off as the ALR was increased above 2.39. For this case, an increase in ALR results in an increase in momentum flux ratio, because the crossflow velocity is held constant for all cases. Further penetration data is now presented for the reduced cross-sectional area crossflow geometry. For these tests, the injector flow conditions are held constant, while the crossflow air velocity is increased from 50 m/sec (164 ft/sec) to 75 m/sec (246.1 ft/sec) to 100 m/sec (328.1 ft/sec). This increase in crossflow velocity results in a decrease in the momentum flux ratio. Table 8 below presents the relevant flow information for the crossflow velocity variations. The hole size used for this testing is 0.088 inch in diameter. The LDI fuel tip geometry is also employed and is recessed back a distance of 0.0625 in. from the injector panel.

Crossflow Velocity	(ρU^2)Cross	Fuel Mass Flow	Injector Air Mass Flow	Fuel Velocity	Injector Air Velocity	(ρU^2) Jet	Momentum Flux Ratio
m/sec	$kg/m*sec^2$	g/sec	g/sec	m/sec	m/sec	$kg/m*sec^2$	
50	3000	0.146	0.379	2.00	98.9	2.08E+06	692.7
75	6750	0.146	0.379	2.00	98.9	2.08E+06	307.9
100	12000	0.146	0.379	2.00	98.9	2.08E+06	173.2

Table 8: Crossflow Velocity Flow Parameters

A series of plots are presented in Figures 42, 43, and 44 which display the trajectories of several drop sizes for the three crossflow velocities. These figures were created from PDI data taken at four axial heights, z=5, 10, 20, and 30 mm downstream of the injector hole. The data are radial profiles taken in line with the injector hole. The X-axis of every plot extends from 0 mm to 18 mm. This represents the actual width of the crossflow hardware. The left Y-axis can be considered the injector panel wall, and the right Y-axis represents the opposing wall. The fuel injector hole is located at a downstream distance of 0 mm. The crossflow air velocity is represented by the vectors directed down at the 10 mm mark. Also overlaid on these trajectory plots are contour plots of the counts/sec for each drop size. Because the data rate for the three drop sizes for the three crossflow velocities varied dramatically, each plot includes a legend for its particular contour plot. Please note the large changes in data rate for various sizes and conditions.

Figure 42 presents trajectory and contour plots for the 1-10 micron drop size range. For the 50 m/sec case (leftmost plot), the 1-10 micron drops are capable of penetrating into the center of the crossflow area and reach the opposing wall at a downstream distance of approximately -22 mm. Additionally, the trajectory of these drops demonstrates that they are colliding with the far wall. For the 75 m/sec condition (middle plot), the 1-10 micron drops seem to be equally distributed across the width of the channel at the highest measurement position. However, only very few drops were detected by the PDPA at further downstream distances. This could be due to the PDPA settings. For the 100 m/sec condition (rightmost plot), the 1-10 micron drops are traveling almost vertically. The concentration of these drops is initially (-5 mm) very close to the injector panel wall. The force associated with the crossflow air pushes these small drops immediately down by the wall. At downstream distances, a concentration of 1-10 micron drops suddenly appears in the middle of the crossflow channel. This demonstrates that the crossflow air is assisting in the atomization process. Larger drops at -5 and -10 mm downstream are breaking into 1-10 micron drops are are first observed at the -20 mm downstream distance. Very few 1-10 micron drops are capable of penetrating to the opposite wall for this flow condition.

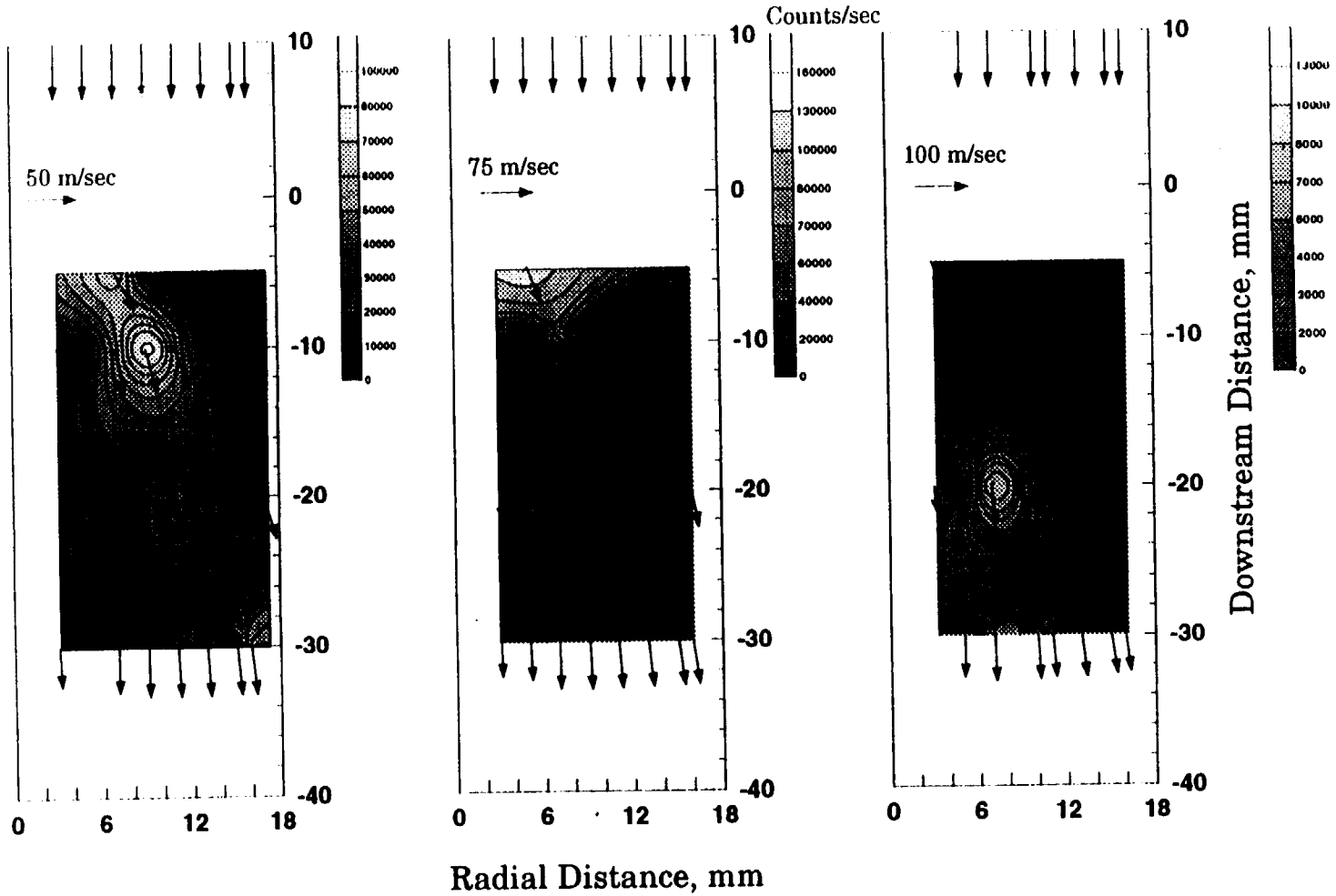

Figure 42: Trajectory plots for the 1-10 micron drop size class.
Crossflow velocities of 50, 75, and 100 m/sec are presented.

Figure 43 presents similar trajectory and contour plots for the 21-30 micron drop size class. For the 50 m/sec crossflow velocity, these drops are definitely penetrating to the opposite wall. The trajectory of the drops very close to the wall clearly demonstrate this. Additionally, while running at this condition, intermittent drops of fuel were found to drip from the opposing wall. For the 75 m/sec case, the collision of drops with the wall is pushed further downstream. Drops for this condition are colliding with the wall at the -20 downstream distance. This was also observed during the testing, but no drops were found to drip off the wall further downstream, indicating minimal wetting of the wall. The 100 m/sec crossflow velocity seems to prevent the 21-30 micron droplets from reaching the opposite wall. Very little wetting of the far wall was evidenced for this condition.

Figure 44 displays the same trajectory and contour plots for the 41-50 micron drop sizes. Similar results to the 21-30 drop size class are obtained. For the 50 m/sec condition, fuel penetrates to the opposing wall at a downstream distance of -10 mm. For the 75 m/sec case, the wetting of the far wall is prevented down to the -20 mm mark. Again, the 100 m/sec case appears to prevent most drops from reaching the opposite wall.

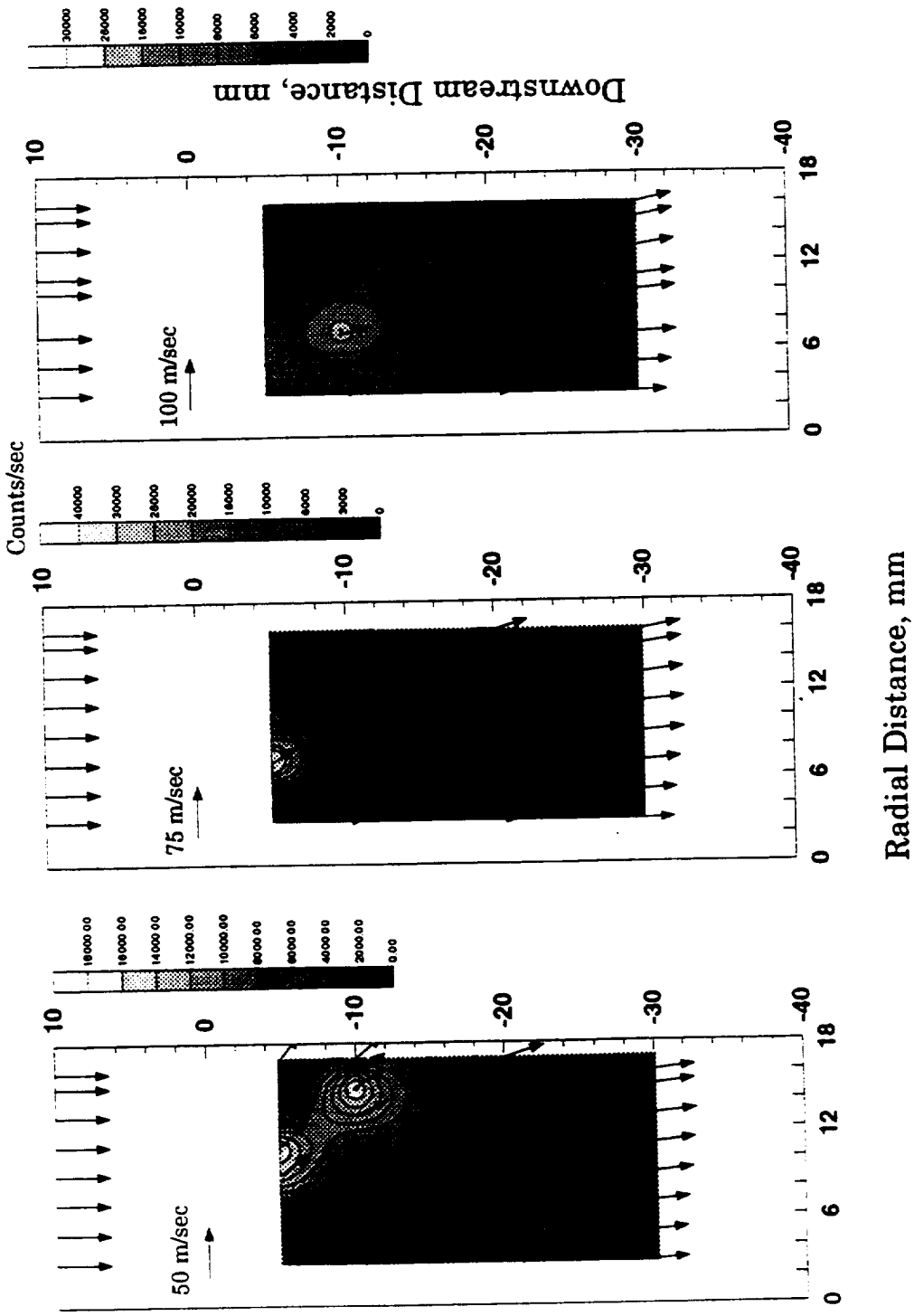

Figure 43: Trajectory plots for the 21-30 drop size class. Crossflow velocities of 50, 75, and 100 m/sec are presented.

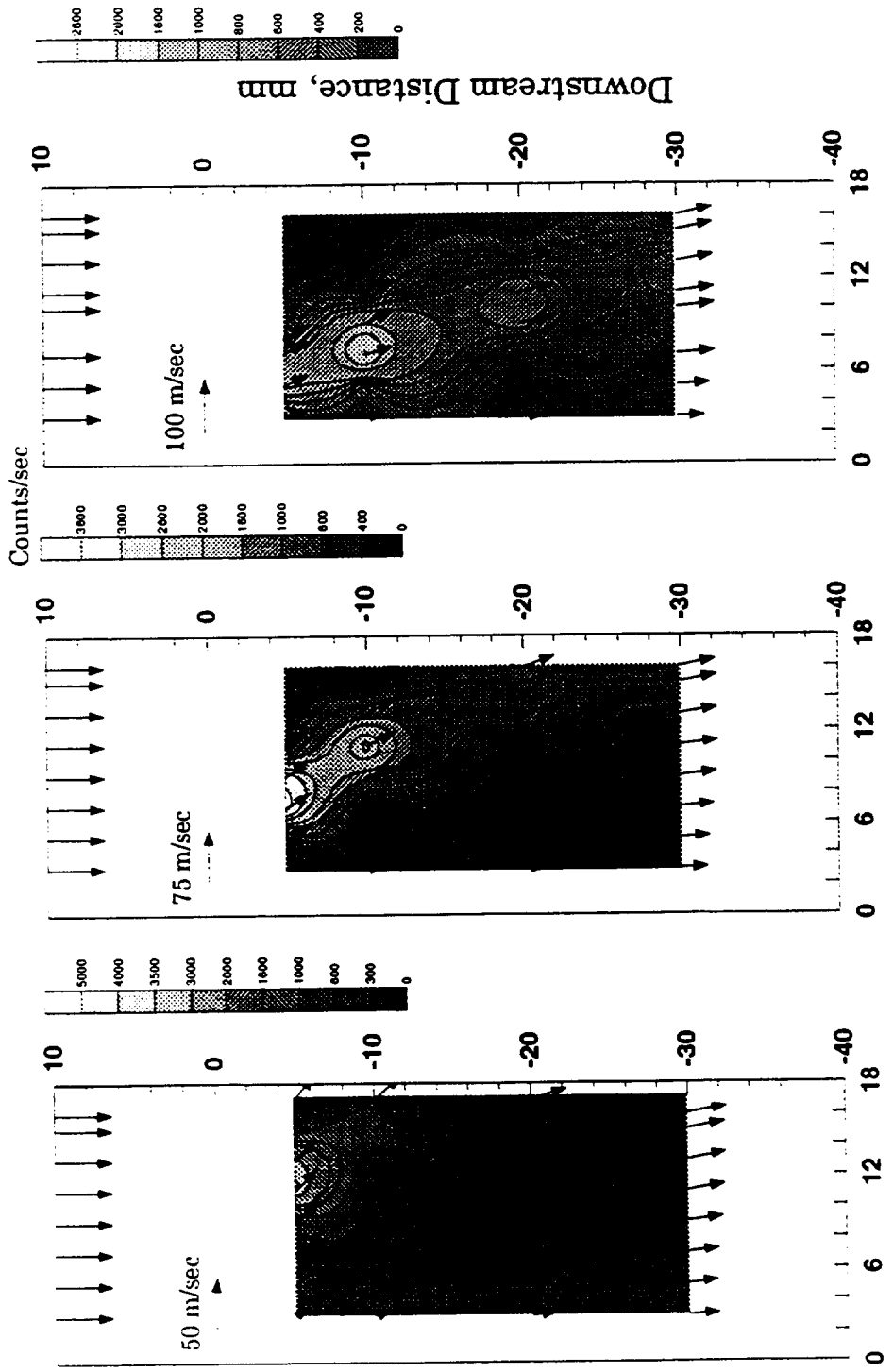

Figure 44: Trajectory plots for the 41-50 micron drop size class. Crossflow velocities of 50, 75, and 100 m/sec are presented.

As discussed in Section 5.1, the application of semi-empirical predictions (Lefebvre, 1983) to the current setup did not yield reasonable results for injector flow conditions where injector air was introduced. Equation 19 in Section 5.1.2 performs well in predicting the penetration of the liquid jet cases, but overpredicts dramatically for cases with injector air. This is attributed to the difficulty in defining an *initial* jet density and velocity. However, by tailoring the empirical constant in this prediction again, a reasonable estimate of penetration can be obtained for flow conditions utilizing injector air. The following equation is altered to provide a penetration prediction for the current setup (Lefebvre, 1983):

$$Y = 1.35 * D_{Jet} J^{0.5} \left(\frac{Z}{D_{Jet}} \right)^{0.33} \qquad (20)$$

where,

Djet = Air hole size
J = Momentum flux ratio
Z = Downstream distance

The ρ_{Jet} term in J is approximated using equation 18 found in section 5.1.1 and U_{Jet} is defined as the relative velocity between fuel and air. The empirical constant in the equation is altered to provide a reasonable prediction for the center of mass of the spray for the 50 m/sec case. This was accomplished by examining the data presented in Figure 44 on 41-50 micron droplets. In previous work, these drop sizes tended to be located around the center of mass of the spray. The empirical constant was varied

until a reasonable fit was yielded for 50 m/sec case. Figure 45 presents three plots of the 41-50 drop size for the 50, 75, and 100 m/sec crossflow velocity conditions. Overlaid on these contour plots is the prediction from equation 20 above. The empirical constant selected resulted in reasonable predictions for the 75 and 100 m/sec crossflow velocities. Therefore this equation should prove useful for predicting penetration for injector conditions with similar levels of atomization. The empirical constant for this prediction was modified to account for the initial jet density and velocity for the injector flow condition utilized in this test. This equation is still not capable of predicting the leveling off in penetration seen at higher levels of atomization. The explanation for this is that the equation was developed to predict penetration for various downstream distances rather than for various injector flow conditions.

5.5.1 - Crossflow Velocity Variations Summary

The results of the crossflow velocity variation study yields the following conclusions:

- Spray *penetration* can be accurately described using the momentum flux ratio.
- Under- and over-*penetration* of the spray must be prevented for radial injector applications.

  - Underpenetration can result in a hot core of products surrounded by cool unburned air.
  - Overpenetration can cause wetting of the combustor liner, which results in poor light-up and increased pollutant emissions.

- Equation 20 above can be used to make *penetration* predictions for conditions with similar levels of atomization.
- No PLLIF images were recorded for the crossflow velocity variations. Therefore no information on *spray area* or *fuel uniformity* is available.
- The crossflow air assists in the *atomization* of the spray jet. This is evidenced by the smaller number of 41-50 micron drops located at downstream distances.

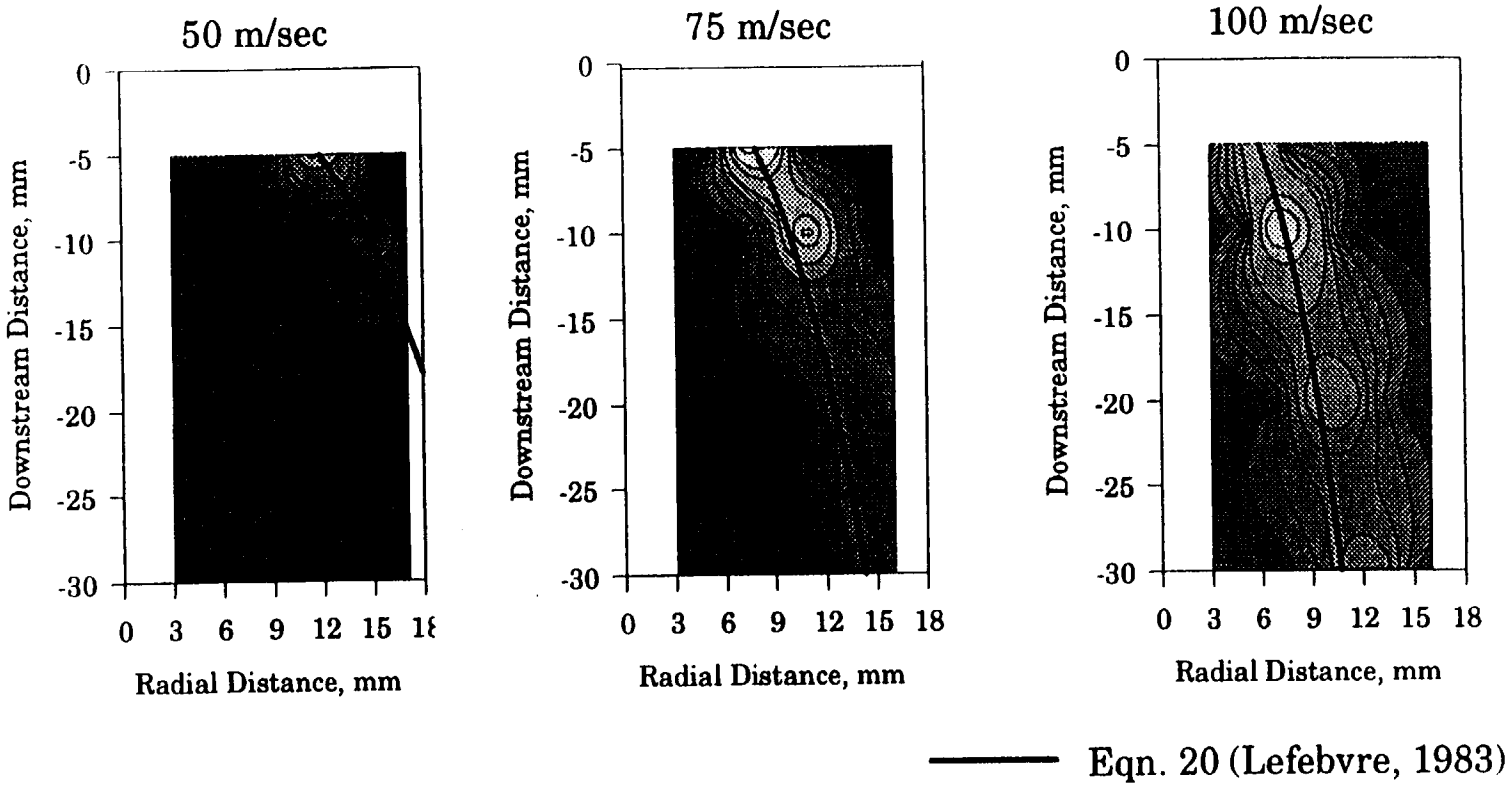

Figure 45: Spray contour plots with penetration prediction.

Chapter 6.0 - Summary, Conclusions, and Recommendations

An experimental study of a liquid jet injected radially into a high velocity cross-stream is presented. The study is directed toward developing an understanding of the atomization process and optimizing the fuel preparation and injection characteristics of a liquid jet injector. The following sections present a summary of the work conducted, conclusions based on the results of the study, and recommendations for liquid jet injection.

6.1 - Summary

The current experimental study is focused on the injection of a liquid jet from a radial airblast injector into a high velocity crossflow of air. Atomization, spray area, and penetration are presented to describe the performance of the injector. Two laser diagnostics are utilized to characterize the spray: Phase Doppler Interferometry (PDI) and Planar Liquid Laser Induced Fluorescence (PLLIF).

Extensive phase Doppler interferometry measurements are provided to relate information on the atomization quality for various flow conditions. Data collected on both the droplet sizes and two components of velocity assist in examining not only the penetration and dispersion characteristics

of the liquid jet, but also the degree to which this jet is atomized. The PDI data supply information on the following spray characteristics: 1) Mean drop diameters for a variety of injector flow conditions; 2) Drop size distributions for various injector flow conditions; 3) Trajectories of different drop sizes; and 4) Concentrations of drop size classes.

Planar laser induced fluorescence provides information on the spray area and penetration of the liquid jet. As stated previously, these two parameters are crucial to the performance of any given injector. The "optimal" fuel injector for this application provides a completely uniform mixture of fuel and air over the desired flow area. The PLLIF spray diagnostic affords a quick measure of the distribution of the mass of fuel in the spray. For the current study, PLLIF is utilized to provide information on: 1) Penetration of the center of mass of the spray; 2) Total "coverage" (i.e., spray area) of a given spray condition; 3) Distribution of mass within the spray area.

The experimental study of this radial airblast injector is divided into five major parametric studies: 1) Injector flow variations; 2) Fuel injection positioning; 3) Fuel tip geometry; 4) Injector air hole size; and 5) Crossflow velocity variation. The first parametric study is centered on varying the air-to-liquid ratio and pressure drops associated with the

injector. PDI and PLLIF data are acquired for ALR's ranging from 0 to 4.67. Fuel pressure drops of 0.5 psid, 5 psid, and 30 psid are examined for air pressure drops of 0, 3, and 6%. The second parametric study investigates the effect of fuel tip positioning on atomization. Four locations are characterized utilizing PDI. The fuel tip geometry variation is also an attempt to optimize the flow through the injector with the goal of improving atomization. The fuel hole size study is conducted to determine the relative importance of ALR versus air velocity on the atomization process for the current setup. The final parametric study is presented to examine the relationship between momentum flux ratio and spray penetration.

6.2 - Conclusions

The examination and analysis of the data from the five parametric studies yields the following conclusions.

- An experiment has been successfully designed and demonstrated that addresses the mechanisms of atomization and dispersion of a liquid jet injected radially into a high velocity crossflow.

- Momentum-flux ratio is an important parameter in describing the spray *penetration*.
  - Since a portion of the atomizing air kinetic energy is consumed in stripping and atomizing the liquid jet, pure air or liquid jet in crossflow predictions are not capable of describing the trends seen in the current airblast injector. These pure jet analyses are capable of predicting penetration conditions utilizing no injector air (i.e., pure liquid jet conditions).

  - However these pure jet equations can be modified to reasonably predict penetration of cases with injector air. By modifying the empirical constant in the prediction, the problems associated with

defining *initial* jet density and velocity can be avoided. Equation 20 can be applied to cases with similar levels of atomization.

- The cross-sectional *spray area* can, in some cases, be used to determine the performance of an injector. An index of mixing (i.e. *fuel uniformity*) within this area is also useful. The use of PLLIF permits this level of mixing to be assessed.

- *Atomization* is one key factor affecting spray penetration and area.
  - For higher ALR's, small droplets are formed which become entrained early in the crossflow air and are convected immediately in close proximity to the wall.
  - For lower ALR's, the smaller drops are fewer in number and an elliptical spray pattern is developed, which penetrates the crossflow away from the wall.

- Fuel tip positioning affects the flow characteristics within the injector, but does not appreciably affect the overall *atomization, penetration*, and *spray area* of the injector for the flow conditions examined. There is, however, an optimum position for the fuel tip which is found to be at the midpoint of the air channel.

- Fuel tip geometry does not appreciably affect the levels of *atomization, penetration* and *spray area*. However tip geometries which minimize the blockage of the exit air hole are preferred, because more air is supplied to the injector for any given pressure drop (i.e., higher relative velocities and ALR's).

- Variations in injector hole size result in a tradeoff between relative velocity and ALR.
  - Relative velocity plays a more dominant role in the *atomization* process than ALR for the flow conditions and geometries examined. Smaller SMD's are obtained for conditions with lower ALR's but higher relative velocities.

- Penetration equations, utilizing momentum flux ratio, are capable of predicting penetration versus downstream distance for various crossflow velocities.

6.3 - Recommendations

Several recommendations associated with this radial airblast injector are now provided in terms of design considerations and future studies:

Design Considerations

- Operating the injector at ALR's higher than approximately 3 does not yield substantial improvements in atomization, penetration, or area of the fuel.

- PLLIF images alone are not sufficient for describing the performance of the injector. PDI data are required as well.

- Fuel tip positioning is optimized for the 0.0625" (1.59 mm) distance. This provides an excellent compromise between injecting the liquid into a high velocity region and blocking the injector air hole.

- The 0.088 in. (2.24 mm) diameter air hole size provides slightly improved atomization over the 0.125 in. (3.18 mm) air hole size. However further studies on both larger and smaller diameter holes are recommended.

- Tip geometries which minimize air hole blockage are preferred.

Future Studies

- Because gas turbine combustors operate with air at elevated temperatures and pressures, further work on temperature and pressure effects on the spray are recommended.

- The injector configuration studied here is that of an eight-port radial airblast nozzle. Therefore a study on the interaction of a series of injector holes could provide useful information on placement and optimum number of ports.

- The close proximity of the injector holes to the swirl vanes in the LDI concept (Shaffar, 1993) has resulted in questions about the placement of these vanes with respect to the air holes. A parametric study of the placement of swirler vanes is also recommended.

References

Bachalo, W.D., Aerometrics Phase Doppler Particle Analyzer 2-Component Operations Manual, August 1987.

Bachalo, W.D., and Houser, M.J., "Development of the Phase/Doppler Spray Analyzer for Liquid Drop Size and Velocity Characterizations," AIAA-84-1199, Presented at the Twentieth Joint Propulsion Conference, Cincinnati, Ohio, June 1984.

Bryan, R., Godbole, P.S., and Norster, E.R., "Characteristics of Airblast Atomizers," *Combustion and Heat Transfer in Gas Turbine Systems*, Cranfield International Symposium Series, Vol. 11, pp. 343-359, 1971.

Chapman, S., "On Ozone and Atomic Oxygen in the Upper Atmosphere," Phil. Mag. Ser. 7, Vol. 10, No. 64, pp. 369-383, 1930.

Correa, S.M., "Esitmates of Lean Direct-Injection Combustion for NOx Suppression," 90CRD266, GE Research and Development Center, December 1990.

Crutzen, P.J., "Ozone Production Rates in an Oxygen, Hydrogen, Nitrogen Oxide Atmosphere," J. Geophys. Res., Vol. 76, pp. 7311-7327, 1971.

Fenimore, C.P., "Formation of Nitric Oxide in Premixed Hydrocarbon Flames," *Thirteenth Symposium (International) on Combustion*, The Combustion Institute, Pittsburgh, pp. 317-380, 1970.

Fishman, J., "The Global Consequences of Increasing Tropospheric Ozone Concentrations," Chemosphere, Vol. 22, No. 7, pp. 685-695, 1991.

Haagen-Smit, A.J., "Chemistry and Physiology of Los Angeles Smog," Ind. Eng. Chem., Vol. 44, pp. 1342-1346, 1952.

Haagen-Smit, A.J. and Fox, M., "Ozone Formation in Photochemical Oxidation of Organic Substances," Ind. Eng. Chem., Vol. 48, pp. 1484-1487, 1956.

Hanson, R.K., "Combustion Diagnostics: Planar Imaging Techniques," *Twenty-first Symposium (International) on Combustion*, The Combustion Institute, pp. 1677-1691, 1986.

Holdeman, J.D., "Mixing of Multiple Jets with a Confined Subsonic Crossflow," *Prog. Energy Combust.* Sci, Vol. 19, pp. 31-70, 1993.

Holman, J.P., Thermodynamics, 4th Edition, McGraw-Hill, Inc., New York, 1988.

Igushi, T., McDonell, V.G., and Samuelsen, G.S., "An Imaging System for Characterization of Liquid Volume Distributions in Sprays," Sixth Annual Conference of Liquid Atomization and Spray Systems, Worcester, MA. Extended Abstracts pp. 142-146, May 1993.

Johnston, H., "Reduction of Stratospheric Ozone by Nitrogen Oxide Catalysts from Supersonic Transport Exhaust," Science, No. 173, pp. 517-522, 1971.

Ko, M.W.K. et. al., "Effects of Engine Emissions from High-Speed Civil Transport Aircraft: A Two-Dimensional Modeling Study, Parts I and II," NASA CR 4346, Part I and II, 1991.

Lefebvre, A.H., Gas Turbine Combustion, Hemisphere Publishing, New York, 1983.

Liscinsky, D.S., True, B., and Holdeman, J.D., "Crossflow Mixing of Noncircular Jets," AIAA-95-0732, Presented at the Thirty-Third Aerospace Sciences Meeting and Exhibit, Reno, Nevada, January 1995.

Lorenzetto, G.E., and Lefebvre, A.H., "Measurements of Drop Size on a Plain-jet Airblast Atomizer," *AIAA J.*, Vol. 15, No. 7, pp. 1006-1010, 1977.

McDonell, V.G. and Samuelsen, G.S., "Application of Two-Component Phase Doppler Interferometry to the Measurement of Particle Size, Mass Flux, and Velocities in Two-Phase Flows," *Twenty-Second Symposium (International) on Combustion*, The Combustion Institute, pp. 1961-1971, 1988.

McDonell, V.G. and Samuelsen, G.S., "Sensitivity Assessment of a Phase-Doppler Interferometer to User-Controlled Settings," Liquid Particle Size Measurement Techniques: 2nd Volume, ASTM STP 1083, American Society for Testing and Materials, Philadelphia, pp. 170-189, 1990.

McDonell, V.G., Seay, J.E., and Samuelsen, G.S., "Characterization of the Non-reacting Two-phase Flow Downstream of an Aero-engine Combustor Dome Operating at Realistic Conditions," ASME 94-GT-263, Presented at International Gas Turbine and Aerosengine Congress and Exposition, The Hague, Netherlands, June, 1994.

Molina, M.J. and Rowland, F.S., "Stratospheric Sink for Chlorofluoromethanes: Chlorine-Catalyzed Destruction of Ozone" *Nature* **249**, pp. 810-812, 1974.

Nature Academy of Sciences, Ozone and Other Photochemical Oxidants, Washington, 1977.

Newhall, H.K., *Twelfth Symposium (International) on Combustion*, Combustion Institute, Pittsburgh, 1969.

Nukiyama, S. and Tanasawa, Y., "Experiments on the Atomization of Liquids in an Airstream," *Trans. Soc. Mech. Eng. Jpn.*, Vol. 5, pp. 68-75, 1939.

Nguyen, T.T., and Karagozian, A.R., "Liquid Fuel Jet in Subsonic Crossflow,", *J. Propulsion*, Vol. 8, No. 1, January 1992.

Prather, M.J. et. al., "The Atmospheric Effects of Stratospheric Aircraft: A First Program Report," NASA RP 1272, 1992.

Reinecke, W.G., "Drop Breakup and Liquid Jet Penetration," AIAA Journal, Vol.16, No. 6, 1978.

Rizkalla, A.A. and Lefebvre, A.H., "The Influence of Air and Liquid Properties on Airblast Atomization," *J. Fluids Eng.*, Vol. 97, No. 3, pp. 316-320, 1975.

Rowland, F.S. and Molina, M.J., "Chlorofluoromethanes in the Environment," Rev. Geophys. Space Phys., Vol. 13, pp. 1-35, 1975.

Shaffar, S.W., "Reduction of Oxides of Nitrogen from a Liquid Fueled Gas Turbine Combustor," Masters Thesis, University of California - Irvine, 1993.

Sowa, W.A., "Interpreting Mean Drop Diamters Using Distribution Moments," Atomization and Sprays, vol. 2, pp. 1-15, 1992.

Stanford Research Institute, " The Smog Problem in Los Angeles County, A Report by Stanford Research Institute on Studies to Determine the Nature and Causes of Smog," Western Oil and Gas Association, January 1954.

Tacina, R.R., "Low Nox Potential of Gas Turbine Engines," NASA Lewis Research Center, AIAA-90-0550, Presented at the Twenty-Eighth Aerospace Sciences Meeting, Reno, Nevada, January 1990.

Thamban, A.T.S, Talley, D.G., McDonell, V.G., and Lee, S.W., "Visualizing Laser Sheet Illumination of Sprays with Restricted Optical Access," 7th Annual Conference on Liquid Atomization and Spray Systems, Bellevue, Washington, Extended Abstracts, pp. 138-142, June 1994.

Turco, R.P., Climate System Modelling, Cambrige University Press, pp. 201 - 240, 1990.

Zeldovich, J., "The Oxidation of Nitrogen in Combustion and Explosions," Acta Physicochimica, URRS, Vol. 21, No. 4, pp. 577-628, 1946.

Appendix A - Crossflow Velocity Characterization

A uniform crossflow velocity within the 3 in. by 4 in. wind tunnel test section was essential in order to achieve accurate results on penetration and area. A great deal of work was focused on achieving a uniform velocity profile over the entire wind tunnel cross-sectional area. As described in Chapter 4 on the experimental setup, a series of grids and screens were utilized. Additionally, an impingement plate was included to break-up the initial air jet exiting the 2" pipe. Many variations on this setup were attempted and tested and the configuration described was found to be optimal. The following two plots are presented to demonstrate the level of uniformity in the wind tunnel test section. The first plot (Figure A.1) shown is a 3-D plot of the axial velocity. For most testing this value was set to 38 m/sec. The velocities in the plot vary from 38.1 m/sec to at most 39.9 m/sec with an average velocity of 38.6 m/sec. The second plot is also a 3-D plot of the transverse velocity. For air traveling straight down, the value for this component of velocity should be 0 m/sec. As seen in Figure A.2, the velocity varied from -1.2 m/sec to 1.0 m/sec with an average velocity of -0.13 m/sec.

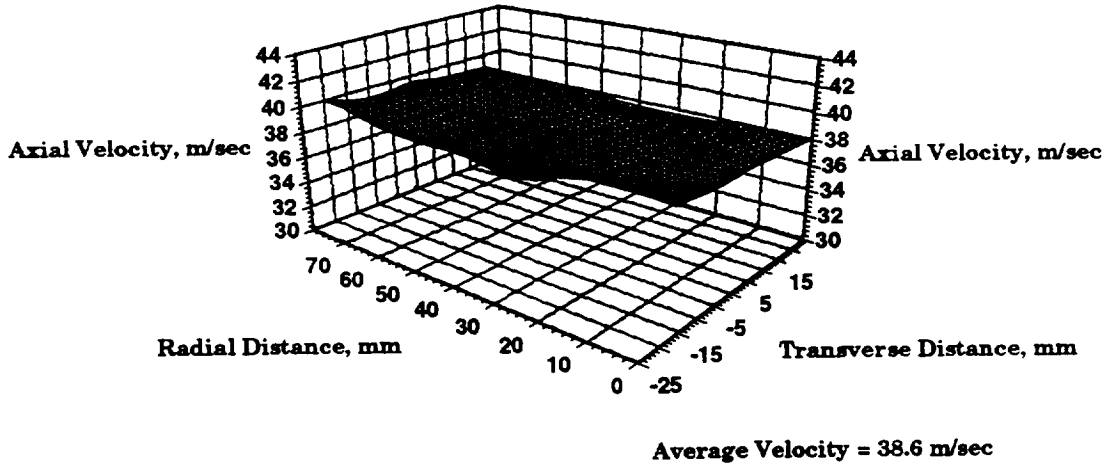

Figure A.1 - Axial velocity within 3" by 4" wind tunnel test section, Z = 0 mm.

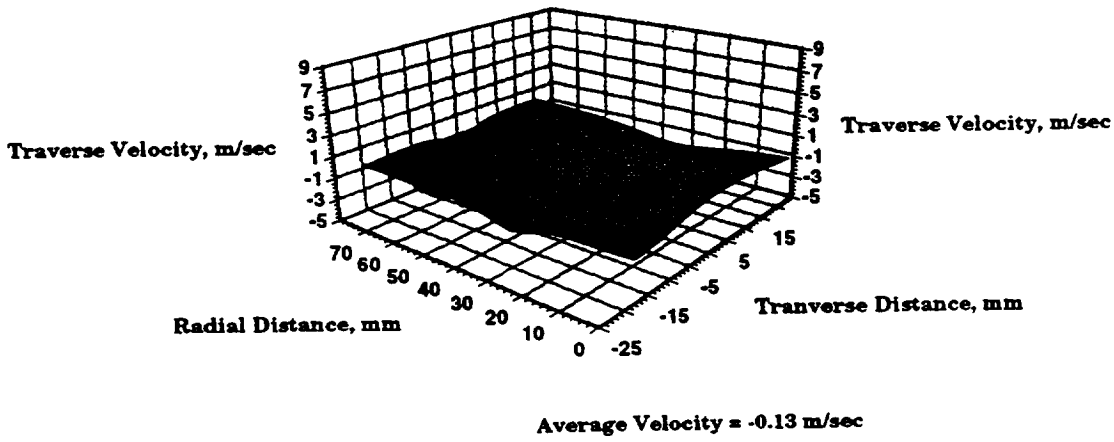

Figure A.2 - Transverse velocity profile within wind tunnel test section, Z = 0 mm.

Appendix B - PLLIF Processing Program

After a PLLIF image has been acquired, a great deal of processing is required to obtain information on mixture fraction, dispersion, uniformity, and other statistical functions. All PLLIF images taken for the current testing began in the form of a picture file termed a .TIF file. This is a standard file for storing picture information and is basically a string of numbers describing the location of each pixel and a gray level value from 0 to 255. Depending on the capabilities of the CCD camera utilized, the range of values for gray level could be either lower or much greater. The TIF files can be viewed with a number of PC-based or Unix-based packages.

For the present study, all images were processed on a Unix workstation. A package termed XView was utilized for its capabilities in converting .TIF files into another form, .PGM (ascii) files. The first step in the process requires this conversion from .TIF to .PGM (ascii) files. This conversion allows the images to be processed by a program developed by a visiting scientist in the UCI Combustion lab, named Yutaka Iuchi. The program written by Yutaka takes the .PGM files as the input. The program then converts the information into a more friendly form, triplets format. The output of the program is in the form of three columns of data: X pixel location, Y pixel location, and a gray level associated with each X, Y location. The size of the original image (i.e. # of pixels by # of pixels)

dictates the length of the output file. Once in triplets format, the files can then be processed by a variety of PC-based programs such as Microsoft Excel, Surfer, or Stanford Graphics. However a 640 x 640 sized image results in close to 20,000 lines of text in triplets format. Therefore many PC-based programs have difficulty with processing this much information. For the current work, most of the files processed were closer to 300 x 300 pixels (approximately 3000 lines in triplets format). The program written by Yutaka is presented below.

```
/********
Data form translation xv format to triplet format
********/

#include <stdio.h>
#include <stdlib.h>
#include <string.h>
#include <math.h>

main (int argc, char **argv)
{
        FILE *fp;
        FILE *fp2;
        char buff[256];
        int flag;
        char pool[3];
        int i;
        int j;
        int x;
        int y;
        int k;
        float r;
        int rowlength;
        int columlength;
        static unsigned int Data[650][490];
        static unsigned int Databuff[17];
```

```
printf("Hallo file comb. \n");
        if((fp = fopen(argv[1], "rt" )) == NULL)
                printf("Somethings wrong %s\n","100.txt");
        else
        {
                fgets(buff,256,fp);
                printf( "%s\n",buff);

                buff[0] = '#';
                while(buff[0] == '#')
                {
                        fgets(buff,256,fp);
                        printf( "%s\n",buff);
                }

                /*fgets(buff,256,fp);*/
                /*printf( "%s\n",buff);*/

                for(i = 0; i <= 2; i++)
                        pool[i] = buff[i];
                columlength = atof(pool);
                printf( "%d\n",columlength);

                for(i = 0; i <= 2; i++)
                        pool[i] = buff[i+4];
                rowlength = atof(pool);
                printf( "%d\n",rowlength);

                fgets(buff,256,fp);
                printf( "%s\n",buff);

                x = 1; y = 1;

                while((fgets(buff,255,fp) != NULL ))
                {
                        k=0;
                        for(i = 0; i <= 64; i+=4)
                        {
                                for(j=0; j<=2; j++)
                                        pool[j] = buff [i+j];
                                /*strncpy(pool,pool,3);*/
                                if(k>16)
                                        k=0;
                                Databuff[k] = atof(pool);
                                k++;
```

```
                }

                /*printf("\n");*/
                for(j = 0; j <= 16; j++)
                {
                        Data[x][y] = Databuff[j];
                        /*printf( "%d, %d, %d\n", x, y, Data[x][y]);*/
                        x++;
                        if(x>columlength)
                        {
                                y++;
                                x = 1;
                        }
                }
        }

}
fclose(fp);

fp2 = fopen(argv[2], "wt");

for(y = 1; y <= rowlength; y++)
{
        for(x = 1; x <= columlength; x++)
        {
                fprintf(fp2, "%d, %d, %d\n", x, y, Data[x][y]);
        }
}

fclose(fp);

}
```

Appendix C - Fuel Mass Fraction Program

For the current work, most of the PLLIF images presented are in the form of fuel mass fraction plots. To obtain data on fuel mass fraction a FORTRAN program was written to convert gray scale information to fuel mass fraction. The following equation was utilized:

$$F = \frac{G_{X,Y}}{255}$$

where F = fuel mass fraction

$G_{X,Y}$ = gray level at a given X,Y pixel

The program utilized to obtain information on fuel mass fraction is presented below.

```
INTEGER a, b, c, j
    REAL f, ijet, imain
    character*16 name, output
    write(*,*)'Please input data filename.'
    read(*,*)name
    write(*,*)'Please enter output filename '
    read(*,*)output
    open(unit=10,file=name,status='old')
    open(unit=9,file=output,status='unknown')
    ijet=255
    imain=0
100   If (b .LT. 216) then
       read(10,*)a,b,c
       f=(c-imain)/(ijet-imain)
       j=j+1
        if (j .eq. 25) then
         write(9,*)a, b, f
```

```
        j=0
       endif
     goto 100
     endif
   close(10,status='keep')
   close(9,status='keep')
   stop
   end
```

Appendix D - Spatial Unmixedness Program

A FORTRAN program was also developed to provide information on the spatial unmixedness and statistical functions associated with the images. This file takes the triplet format from the Yutaka program and outputs the required information. The program is presented below.

```
INTEGER a, b, c
     REAL average, denom, num, cvar, tot, us, cavg
     REAL ci,diff,sum,stddev,numer,ctop,den,use,tote
     REAL caver,iten,ca,top,grab,stuff,gober,deno
     INTEGER total, count
     character*16 name, output
     write(*,*)'Please input data filename.'
     read(*,*)name
     write(*,*)'Please enter output filename '
     read(*,*)output
     open(unit=10,file=name,status='old')
     open(unit=9,file=output,status='unknown')
     total=0
     count=0
100    If (b .LT. 218) then
       count=count+1
       read(10,*)a,b,c
       total=total+c
       iten=255*count
     goto 100
     endif
     if (count .ge. 0) then
       write(6,*)'Average is:',float(total)/count
     else
       write(6,*)'Input file is empty'
     endif
     average=float(total)/count
     close(10,status='keep')
     a=0
     b=0
     c=0
```

```
      tot=0
      num=0
      count=0
      tote=0
      sum=0
      cavg=float(average)/255
      caver=float(total)/iten
      denom=cavg*(1-cavg)
      den=caver*(1-caver)
      deno=total*(1-total)
      open(10,file=name,status='old')
200    If (b .LT. 218) then
       count=count+1
       read(10,*)a,b,c
       ci=float(c)/255
       num=(ci-cavg)*(ci-cavg)
       tot=tot+num
       ca=float(c)/iten
       diff=(c-average)*(c-average)
       sum=sum+diff
       stddev=sqrt(sum/count)
       numer=(ca-caver)*(ca-caver)
       tote=tote+numer
       top=(c-total)*(c-total)
       grab=grab+top
      goto 200
      endif
      stuff=float(grab)/count
      gober=float(stuff)/deno
      stat=float(stddev)/average
      cvar=float(tot)/count
      us=float(cvar)/denom
      ctop=float(tote)/count
      use=float(ctop)/den
      write(6,*)'The spatial unmixedness is:',cvar,denom,us
      write(6,*)'The standard deviation statistics are:', stddev,stat
      write(6,*)'The Us using total/iten:', ctop, use
      write(6,*)'The Us using total:',stuff,gober
      write(9,*)name
      write(9,*)'The spatial unmixedness (Us) via Holdeman=',us
      write(9,*)'The standard deviation=',stddev
      write(9,*)'standard deviation/mean=',stat
      write(9,*)'Us using total/iten',use
      write(9,*)'The Us using total:',gober
      write(9,*)'The average intensity=',average
```

```
write(9,*)'The sum of intensities=',total
write(9,*)'255 times the number of pixels=',iten
close(10,status='keep')
close(9,status='keep')
stop
end
```

Appendix E - Sensitivity and Repeatability of PDI Measurement

Previous research on Phase Doppler Interferometry (PDI) has shown that user-controlled settings have an influence on the measured quantities (i.e., velocities and drop sizes) (McDonell and Samuelsen, 1990). Specifically, photomultiplier tube (PMT) voltage, frequency shift, and maximum sizing are considered important variables to standardize.

PMT voltage can have dramatic effects on the drop sizes measured. Figure E.1 presents a plot of D10 and SMD versus PMT voltage. As the voltage is increased, the drop sizes begin to fall off sharply. The measured Sauter Mean Diameter then levels off at higher voltages, while the D10 continues to fall. The manufacturer's recommended setting is one which provides a minimum value of D10 without saturating the detectors. For the present study, this voltage was found to be 250 mV and was held constant for all testing.

Frequency shift is the second user-controlled parameter which can affect results. The manufacturer's procedure for setting the shift is to 1) set the filter just high enough to eliminate pedestal feed through, 2) add frequency shift equal to approximately the mean of the flow velocity, and 3) increase the shift if needed to bring the frequencies of all scores to within the filter

defined limits. For all current testing, the frequency shift was adjusted and held constant for all cases.

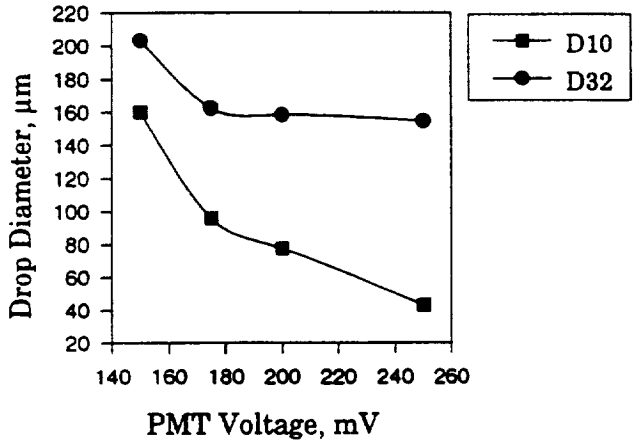

Figure E.1 - Drop sizing variations versus PMT voltage (ALR - 1 Condition).

Finally the maximum diameter sizing has been shown to affect outputted data. Figure E.2 presents data taken for a single injector flow condition with a PMT voltage of 250 mV. The data shown were acquired at the same time with the only variation being maximum drop size. A maximum variation in Sauter mean diameter of 6 microns was observed. For all comparison data, the maximum drop size was maintained at 304 microns.

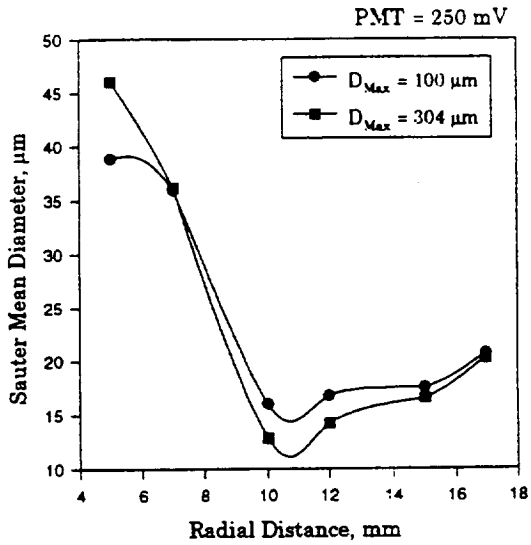

Figure E.2 - Sauter Mean Diameter variations for two maximum drop size settings (ALR 6 Condition).

Finally, to ensure accuracy in PDI measurements for the given user-controlled settings, a repeatability check was completed. Data for the ALR 2.39 condition are presented in Figure E.3. The injector flow conditions, PMT voltage, frequency shift, and maximum sizing were all held constant for the two data sets displayed. The only variation was the time the data was recorded. Two third order polynomial regressions have been fitted through the data sets and fall almost exactly on one another. Therefore, for the PDI user-controlled settings mentioned above, the system provided excellent repeatability and accuracy.

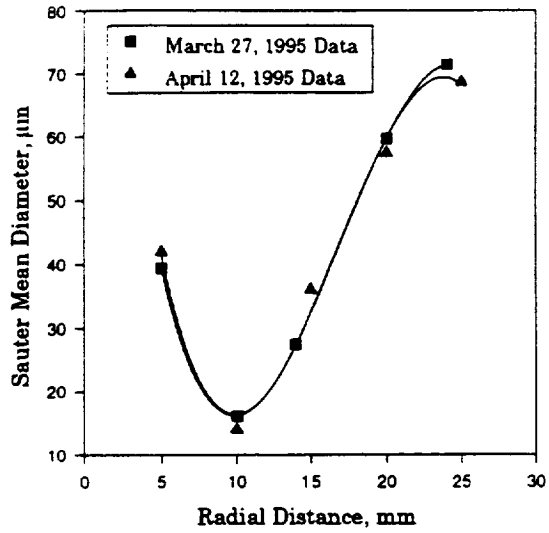

Figure E.3 - Repeatability check on PDI system for ALR - 2.39 condition.

REPORT DOCUMENTATION PAGE

Form Approved
OMB No. 0704-0188

Public reporting burden for this collection of information is estimated to average 1 hour per response, including the time for reviewing instructions, searching existing data sources, gathering and maintaining the data needed, and completing and reviewing the collection of information. Send comments regarding this burden estimate or any other aspect of this collection of information, including suggestions for reducing this burden, to Washington Headquarters Services, Directorate for Information Operations and Reports, 1215 Jefferson Davis Highway, Suite 1204, Arlington, VA 22202-4302, and to the Office of Management and Budget, Paperwork Reduction Project (0704-0188), Washington, DC 20503.

1. AGENCY USE ONLY (*Leave blank*)	2. REPORT DATE	3. REPORT TYPE AND DATES COVERED
	November 1996	Final Contractor Report

4. TITLE AND SUBTITLE

Atomization and Dispersion of a Liquid Jet Injected Into a Crossflow of Air

5. FUNDING NUMBERS

WU-537-05-20
G-NAG3-1124

6. AUTHOR(S)

J.E. Seay and G.S. Samuelsen

7. PERFORMING ORGANIZATION NAME(S) AND ADDRESS(ES)

University of California
Irvine, California 92717-3550

8. PERFORMING ORGANIZATION REPORT NUMBER

E-10507

9. SPONSORING/MONITORING AGENCY NAME(S) AND ADDRESS(ES)

National Aeronautics and Space Administration
Lewis Research Center
Cleveland, Ohio 44135-3191

10. SPONSORING/MONITORING AGENCY REPORT NUMBER

NASA CR-198543

11. SUPPLEMENTARY NOTES

Project Manager, Robert R. Tacina, Propulsion Systems Division, NASA Lewis Research Center, organization code 2710, (216) 433-3588.

12a. DISTRIBUTION/AVAILABILITY STATEMENT

Unclassified - Unlimited
Subject Category 07

This publication is available from the NASA Center for AeroSpace Information, (301) 621-0390.

12b. DISTRIBUTION CODE

13. ABSTRACT (*Maximum 200 words*)

In recent years, environmental regulations have become more stringent, requiring lower emissions of mainly nitrogen oxides (NO_x), as well as carbon monoxide (CO) and unburned hydrocarbons (UHC). These regulations have forced the gas turbine industry to examine non-conventional combustion strategies, such as the lean burn approach. The reasoning behind operating under lean conditions is to maintain the temperature of combustion near and below temperatures required for the formation of thermal nitric oxide (NO). To be successful, however, the lean processes require careful preparation of the fuel/air mixture to preclude formation of either locally rich reaction zones, which may give rise to NO formation, or locally lean reaction zones, which may give rise to inefficient fuel processing. As a result, fuel preparation is crucial to the development and success of new aeroengine combustor technologies. A key element of the fuel preparation process is the fuel nozzle. As nozzle technologies have developed, airblast atomization has been adopted for both industrial and aircraft gas turbine applications. However, the majority of the work to date has focused on prefilming nozzles, which despite their complexity and high cost have become an industry standard for conventional combustion strategies. It is likely that the new strategies required to meet future emissions goals will utilize novel fuel injector approaches, such as radial injection. This thesis proposes and demonstrates an experiment to examine, on a mechanistic level (i.e., the physics of the action), the processes associated with the atomization, evaporation, and dispersion of a liquid jet introduced, from a radial, plain-jet airblast injector, into a crossflow of air. This understanding requires the knowledge not only of what factors influence atomization, but also the underlying mechanism associated with liquid breakup and dispersion. The experimental data acquired identify conditions and geometries for improved performance of radial airblast injectors.

14. SUBJECT TERMS	15. NUMBER OF PAGES
Combuster; Fuel injection; Atomization; Dispersion	160
	16. PRICE CODE: A08

17. SECURITY CLASSIFICATION OF REPORT	18. SECURITY CLASSIFICATION OF THIS PAGE	19. SECURITY CLASSIFICATION OF ABSTRACT	20. LIMITATION OF ABSTRACT
Unc[illegible]fied	Unclassified	Unclassified	